

Data-driven Beam Hardening Correction for Cone Beam Computed Tomography

Dissertation

zur Erlangung des akademischen Grades

**Doktoringenieur
(Dr.-Ing.)**

von Shiras Koodampulli Abdurahman, M. Sc.
geboren am 15.05.1986 in Panangad, Indien

genehmigt durch die Fakultät für Elektrotechnik und Informationstechnik der
Otto-von-Guericke Universität Magdeburg.

Gutachter:

Prof. Dr. rer. nat. Georg Rose
Prof. Dr. rer. nat. habil. Oliver Speck

Promotionskolloquium am 01.10.2021

Abstract

Cone beam computed tomography (CBCT) systems equipped with a flat panel detector are widely employed for clinical and industrial imaging. Clinical CBCT systems facilitate increased patient access and broad volume coverage, enabling them to be utilized for interventional imaging. However, beam hardening, scatter, and image lag artifacts degrade the low-contrast resolution of CBCT images. The correction of these artifacts is crucial to enhance the soft tissue imaging capability of clinical CBCT scanners. Beam hardening artifacts are caused by the violation of the assumed linear forward model of projection generation due to polychromatic X-ray attenuation. State-of-the-art correction methods mitigate the non-linear projection error caused by beam hardening utilizing a polynomial expression. In clinical CT, the polynomial coefficients are pre-computed during the scanner's calibration using a homogeneous water phantom. Since the water correction alone is insufficient to correct the artifacts due to beam hardening by high attenuation bone and metal structures, additional post-processing algorithms based on higher-order correction models are necessary.

In this thesis, novel beam hardening correction algorithms are discussed to improve CBCT image quality. The correction parameters are directly estimated from the projection data by enforcing data consistency conditions on a set of cone beam projection pairs. Consistency conditions are the mathematical expressions of the redundancy exhibited by over-determined projection measurements and need to be strictly satisfied by ideal and error-free projections. The optimal polynomial coefficients for beam hardening corrections are computed by minimizing the projection inconsistency induced by polychromatic X-ray attenuation. The algorithms were validated with the simulation studies and real datasets from CBCT scanners. The results show the feasibility of material- and energy-specific beam hardening corrections without tedious and recurrent calibrations and prior knowledge about X-ray and attenuation spectra. The water and bone corrections significantly improved the quality of clinical C-arm CBCT images. A comparative evaluation of cone beam consistency conditions was conducted by analyzing the efficacy of the corrections when the polychromatic projections are corrupted with errors corresponding to various artifacts. The results from the robustness studies will be valuable to select the appropriate conditions for beam hardening correction depending on the system geometry and the presence of projection errors other than those caused by beam hardening. Likewise, the effectiveness of higher-order beam hardening correction models was compared, utilizing cone beam consistency conditions.

Zusammenfassung

Kegelstrahl-Computertomographiesysteme (KSCT), die mit einem Flachdetektor ausgestattet sind, werden häufig für die klinische und industrielle Bildgebung eingesetzt. Klinische KSCT-Systeme erleichtern den Zugang zu Patienten und decken ein großes Volumen ab, sodass sie auch für die interventionelle Bildgebung eingesetzt werden können. Allerdings führen die Strahlaufhärtung, Streuung und Bildverzögerungsartefakte zu einer geringen Kontrastauflösung von KSCT-Bildern. Die Korrektur dieser Artefakte ist entscheidend für die Verbesserung der Weichteilbildgebung in der klinischen KSCT-Bildgebung. Strahlverhärtungsartefakte werden durch die Verletzung des angenommenen linearen Vorwärtsmodells der Projekterzeugung aufgrund polychromatischer Röntgenabschwächung verursacht. Die aktuellen Korrekturmethode reduzieren den nicht-linearen Projektionsfehler, der durch die Strahlaufhärtung verursacht wird, mithilfe einer Polynomfunktion. In der klinischen CT werden die Polynomkoeffizienten während der Kalibrierung des Scanners mit einem homogenen Wasserphantom vorberechnet. Da die Wasserkorrektur allein nicht ausreicht, um die Artefakte zu korrigieren, die durch die Strahlaufhärtung von Knochen- und Metallstrukturen mit hoher Schwächung entstehen, sind zusätzliche Nachbearbeitungsalgorithmen erforderlich, die auf Korrekturmodellen höherer Ordnung basieren.

In dieser Arbeit werden neuartige Strahlaufhärtungskorrekturalgorithmen zur Verbesserung der KSCT-Bildqualität diskutiert. Die Korrekturparameter werden direkt aus den Projektionsdaten geschätzt, indem Datenkonsistenzbedingungen für einen Satz von Kegelstrahlprojektionspaaren erzwungen werden. Konsistenzbedingungen sind die mathematischen Ausdrücke der Redundanz, die überbestimmte Projektionsmessungen aufweisen, und müssen von den idealen und fehlerfreien Projektionen streng erfüllt werden. Die optimalen Parameter für die Strahlaufhärtungskorrekturen werden durch Minimierung der durch die polychromatische Röntgenschwächung induzierten Projektionsinkonsistenz berechnet. Die Algorithmen wurden mit den Simulationsstudien und echten Datensätzen von KSCT-Scannern verifiziert. Die Ergebnisse zeigen, dass eine material- und energiespezifische Strahlaufhärtungskorrektur ohne langwierige und wiederkehrende Kalibrierungen und ohne Vorwissen über Röntgen- und Abschwächungsspektren möglich ist. Die Wasser- und Knochenkorrekturen verbesserten signifikant die Bildqualität von Kopfbildern im klinischen C-Bogen-KSCT. Eine vergleichende Bewertung der Kegelstrahlkonsistenzbedingungen wurde durchgeführt, indem die Wirksamkeit der Korrekturen analysiert wurde, dabei wurden die polychromatischen Projektionen mit zusätzlichen Fehlern beaufschlagt, die verschiedene typische Bildartefakte hervorrufen. Aus den Ergebnissen der Robustheitsstudien lassen sich Bedingungen für die Auswahl einer geeigneten Strahlaufhärtungskorrektur

ableiten, die die Systemgeometrie und das Vorhandensein bestimmter Projektionsfehler einschließen. Ebenso wurde die Effektivität von Strahlauflärungskorrekturmodellen höherer Ordnung unter Verwendung von Kegelstrahlkonsistenzbedingungen verglichen.

Declaration of Honor

“I hereby declare that I produced this thesis without prohibited external assistance and that none other than the listed references and tools have been used. I did not make use of any commercial consultant concerning graduation. A third party did not receive any nonmonetary perquisites neither directly nor indirectly for activities which are connected with the contents of the presented thesis.

All sources of information are clearly marked, including my own publications.

In particular I have not consciously:

- Fabricated data or rejected undesired results
- Misused statistical methods with the aim of drawing other conclusions than those warranted by the available data
- Plagiarized data or publications
- Presented the results of other researchers in a distorted way

I do know that violations of copyright may lead to injunction and damage claims of the author and also to prosecution by the law enforcement authorities. I hereby agree that the thesis may need to be reviewed with an electronic data processing for plagiarism.

This work has not yet been submitted as a doctoral thesis in the same or a similar form in Germany or in any other country. It has not yet been published as a whole.”

Magdeburg, November 1, 2021

Shiras Koodampulli Abdurahman

Funding

"This work was supported by the Federal Ministry of Education and Research under grant numbers 13GW0095A (STIMULATE) and 13GW0229A (KIDs-CT) and European Regional Development Fund under the operation number ZS/2016/04/78123 as part of the initiative Sachsen-Anhalt WISSENSCHAFT Schwerpunkte."

List of Own Publications

Journal Articles

1. Shiras Abdurahman, Robert Frysch, Richard Bismark, Steffen Melnik, Oliver Beuing, and Georg Rose. Beam hardening correction using cone beam consistency conditions. *IEEE Transactions on Medical Imaging*, 37(10):2266–2277, 2018
2. Shiras Abdurahman, Robert Frysch, Tim Pfeiffer, Oliver Beuing, and Georg Rose. Comparative evaluation of cone-Beam consistency conditions for beam hardening correction in flat detector computed tomography. *IEEE Transactions on Radiation and Plasma Medical Sciences*, 2021 (submitted)
3. Richard NK Bismark, Robert Frysch, Shiras Abdurahman, Oliver Beuing, Manuel Blessing, and Georg Rose. Reduction of beam hardening artifacts on real c-arm ct data using polychromatic statistical image reconstruction. *Zeitschrift für Medizinische Physik*, 30(1):40–50, 2020

Conference Articles

1. Shiras Abdurahman, Robert Frysch, Richard Bismark, Michael Friebe, and Georg Rose. Calibration free beam hardening correction using grangeat-based consistency measure. In *2016 IEEE Nuclear Science Symposium and Medical Imaging Conference Proceedings (NSS/MIC)*, pages 1–3. IEEE, 2016
2. Shiras Abdurahman, Robert Frysch, Richard Bismark, Oliver Beuing, and Georg Rose. A complete scheme of empirical beam hardening correction using grangeat consistency condition. In *2018 IEEE Nuclear Science Symposium and Medical Imaging Conference Proceedings (NSS/MIC)*, pages 1–5. IEEE, 2018
3. Shiras Abdurahman, Robert Frysch, and Georg Rose. Reduction of beam hardening induced metal artifacts using consistency conditions. In *15th International Meeting on Fully Three-Dimensional Image Reconstruction in Radiology and Nuclear Medicine*, volume 11072, page 110721S. International Society for Optics and Photonics, 2019
4. Shiras Abdurahman, Robert Frysch, Steffen Melnik, and Georg Rose. Beam hardening correction using pair-wise fan beam consistency conditions. In *15th*

International Meeting on Fully Three-Dimensional Image Reconstruction in Radiology and Nuclear Medicine, volume 11072, page 110721T. International Society for Optics and Photonics, 2019

5. Shiras Abdurahman, Robert Frysch, and Georg Rose. Scatter correction using pair-wise fan beam consistency conditions. In *15th International Meeting on Fully Three-Dimensional Image Reconstruction in Radiology and Nuclear Medicine*, volume 11072, page 110722I. International Society for Optics and Photonics, 2019

Conference Abstracts and Talks

1. Shiras Abdurahman, Robert Frysch, Richard Bismark, Oliver Beuing, Michael Friebe, and Georg Rose. Beam hardening correction for bi-material objects using Grangeat-based consistency measure. IEEE MIC, Atlanta, 2017.
2. Shiras Abdurahman, Robert Frysch, Richard Bismark, Oliver Beuing and Georg Rose. Beam hardening correction using Grangeat-based consistency measure, IGIC, Magdeburg, 2017.
3. Shiras Abdurahman, Robert Frysch, Richard Bismark, Oliver Beuing, Michael Friebe, and Georg Rose. Strahlauhärtungskorrektur mit der Konsistenzbedingung für die Kegelstrahl-Computertomographie, Neurorad, 2017
4. Shiras Abdurahman, Robert Frysch, Tim Pfeiffer, Richard Bismark, Oliver Beuing and Georg Rose. CTRS: A 3D reconstruction software for cone beam and multi-slice CT scanners, IGIC 2019.
5. Zhi Qiao, Alfredo Illanes, Shiras Abdurahman, and Michael Friebe. A novel automatic gauge detection algorithm for the performance test of a ct scanner with catphan 600 phantom, BMT, 2017

The following conference papers and patents were published/submitted prior to doctoral studies.

Conference Articles

1. Shiras Abdurahman, Anna Jerebko, Thomas Mertelmeier, Tobias Lasser, and Nassir Navab. Out-of-plane artifact reduction in tomosynthesis based on regression modeling and outlier detection. In *International Workshop on Digital Mammography*, pages 729–736. Springer, 2012

-
2. Shiras Abdurahman, Frank Dennerlein, Anna Jerebko, Andreas Fieselmann, and Thomas Mertelmeier. Optimizing high resolution reconstruction in digital breast tomosynthesis using filtered back projection. In *International Workshop on Digital Mammography*, pages 520–527. Springer, 2014

Patents

1. Shiras Abdurahman, Anna Jerebko, and Michael Kelm. Method for generating a combined projection image and imaging device, December 5 2017. US Patent 9,836,858
2. Shiras Abdurahman, Anna Jerebko, and Michael Kelm. Method and apparatus for projection image generation from tomographic images, February 14 2017. US Patent 9,569,864

Contents

List of Abbreviations	xi
1 Introduction	1
1.1 Motivation	1
1.2 Contributions	3
1.3 Organization of the Thesis	5
1.4 Mathematical Notation and Units	6
2 Theoretical Background	7
2.1 CT Physics and System Components	7
2.1.1 X-ray Generation	7
2.1.2 X-ray Attenuation	8
2.1.3 X-ray Detection	10
2.2 X-Ray Projection Imaging and CBCT	12
2.3 CBCT Geometry	13
2.3.1 World Coordinate System	13
2.3.2 Source Detector Coordinate System	14
2.3.3 Pixel Coordinate System	16
2.3.4 Volume Geometry	16
2.3.5 Projection Geometry	17
2.4 Integral Transforms	19
2.4.1 Radon Transforms	19
2.4.2 X-ray Transforms	21
2.5 Image Reconstruction in CT	21
2.5.1 2D Parallel Beam Reconstruction	23
2.5.2 2D Fan Beam Reconstruction	25
2.5.3 3D CBCT Reconstruction	29
2.6 Cone Beam Data Consistency Conditions	31
2.6.1 Grangeat Consistency Conditions	34
2.6.2 Smith Consistency Conditions	35
2.6.3 Fan Beam Consistency Conditions	36
2.7 CT Artifacts	37
2.7.1 Beam Hardening	37
2.7.2 Scatter	43
2.7.3 Metal Artifacts	45

3	First-order Beam Hardening Correction using Consistency Conditions	46
3.1	Introduction	46
3.2	Method	50
3.3	Experiments	56
3.3.1	Simulation Studies	56
3.3.2	Robustness of Algorithms	59
3.3.3	Real and Clinical Data	61
3.4	Results and Discussion	62
3.4.1	Simulation	62
3.4.2	Robustness of Algorithms	68
3.4.3	Real and Clinical Data	79
4	Beam Hardening Correction for Multi-material Objects	89
4.1	Introduction	89
4.2	Method	89
4.2.1	CC-based IBHC	90
4.2.2	CC-based EBHC	92
4.2.3	CC-based BHFC	93
4.3	Experiments	94
4.4	Results and Discussion	95
4.4.1	Simulation	95
4.4.2	Clinical Data	101
5	Conclusions and Outlook	106
	Appendices	109
	Proofs	110
.1	Beer-Lambert Law	110
.2	Redundancy of 2D Radon Transform	110
.3	Fourier Slice Theorem in 2D	110
.4	Scaling Property of Ramp Filter	111
.5	Zeroth-order HLCC	112
.6	Grangeat’s Fundamental Relation	112
.7	Grangeat Intermediate Function from FDCT Projections	113
.8	Smith Intermediate Function	115
.9	Scatter Projections	115
	Bibliography	117

List of Abbreviations

- ADC** Analog to Digital Converter.
- BHF** Beam Hardening Factor.
- BHFC** Beam Hardening Factor-based Correction.
- CBCT** Cone Beam Computed Tomography.
- CC** Consistency Conditions.
- CT** Computed Tomography.
- DBT** Digital Breast Tomosynthesis.
- DCC** Data Consistency Conditions.
- DCS** Detector Coordinate System.
- DICOM** Digital Imaging and Communications in Medicine.
- DSA** Digital Subtraction Angiography.
- DSP** Digital Signal Processing.
- EBHC** Empirical Beam Hardening Correction.
- EM** Electro-Magnetic.
- FBCC** Fan Beam Consistency Conditions.
- FBP** Filtered Back Projection.
- FD** Flat Detector.
- FDK** Feldkamp Davis Kress.
- FFDA** Fixed Forced Detection Actor.
- FFT** Fast Fourier Transform.
- FOV** Field of View.

- FPD** Flat Panel Detector.
- GCC** Grangeat Consistency Conditions.
- GPU** Graphics Processing Unit.
- HE** High Energy.
- HLCC** Helgason-Ludwig Consistency Conditions.
- HU** Hounsfield Unit.
- IBHC** Iterative Beam Hardening Correction.
- keV** Kilo Electron Volt.
- kVp** Peak Kilovoltage.
- LE** Low Energy.
- LPS** Left Posterior Superior.
- MAD** Median Absolute Deviation.
- MAR** Metal Artifact Reduction.
- mAs** Milli Ampere Second.
- MBIR** Model-Based Iterative Reconstruction.
- MC** Monte-Carlo.
- MDCT** Multi-Detector CT.
- MSE** Mean Squared Error.
- NIST** National Institute of Standards and Technology.
- NMAR** Normalized Metal Artifact Reduction.
- PCS** Pixel Coordinate System.
- ROI** Region of Interest.
- SCC** Smith Consistency Conditions.
- SDCS** Source Detector Coordinate System.

List of Abbreviations

SGMD Sum of Geman-Mcclure Differences.

SKS Scatter Kernel Superposition.

SNR Signal-to-Noise Ratio.

SSD Sum of Squared Differences.

SVD Singular Value Decomposition.

TV Total Variation.

VOI Volume of Interest.

WCS World Coordinate System.

List of Figures

1.1	MDCT and C-arm CBCT scanners.	2
2.1	X-ray and attenuation spectra.	8
2.2	World coordinate system.	13
2.3	Rotation angle.	14
2.4	Projection geometry.	17
2.5	Line in 2D	19
2.6	2D fan beam projection geometry.	26
2.7	The geometry of pair-wise cone beam consistency conditions.	33
2.8	Cupping artifacts.	38
2.9	Beam hardening curve and polynomial.	39
2.10	The correction values of IBHC and EBHC.	42
2.11	Beam hardening factor.	43
3.1	Intermediate functions.	48
3.2	The correction polynomial and identity function	52
3.3	The workflow of consistency condition-based water correction.	55
3.4	Quadratic and Geman-McClure error functions	56
3.5	X-ray spectra used for the simulation study.	57
3.6	Projection images of the brain, elliptical cylinder, and head phantoms.	60
3.7	Projection-specific offsets.	61
3.8	Beam hardening correction for the brain phantom.	63
3.9	Beam hardening correction for the elliptical cylinder phantom.	64
3.10	Beam hardening correction for the head phantom.	65
3.11	Beam hardening correction polynomials (simulation studies).	65
3.12	The attenuation profiles (simulation studies).	66
3.13	The minimization of inconsistency measure (simulation studies).	67
3.14	TV-based water correction results.	68
3.15	Robustness of algorithms (Poisson noise).	69
3.16	Effect of Poisson noise on fan beam and Smith intermediate functions	70
3.17	Robustness of algorithm (axial truncation).	72
3.18	Effect of axial truncation on fan beam and Smith intermediate functions	73
3.19	Robustness of algorithms (lateral truncation).	74
3.20	Robustness of algorithms (axial + lateral truncations).	75
3.21	Beam hardening correction for the truncated projections.	76
3.22	Robustness of algorithms (shift along the detector column).	77

List of Figures

3.23	Robustness of algorithms (shift along the detector row).	78
3.24	Effect of detector shift (column) on fan beam and Smith intermediate functions	79
3.25	Effect of detector shift (row) on fan beam and Smith intermediate functions	80
3.26	Robustness of algorithms (shift along the detector column and rows).	81
3.27	Beam hardening correction for the shifted detector projections.	82
3.28	Robustness of algorithms (constant offset).	83
3.29	Robustness of algorithm (projection-specific offset)	84
3.30	Robustness of algorithm (scatter).	85
3.31	Beam hardening correction for the scatter-corrupted projections.	86
3.32	Beam hardening correction for micro-CT data.	86
3.33	The optimization of correction polynomials (micro-CT).	87
3.34	The minimization of normalized inconsistency measure (clinical data).	87
3.35	Beam hardening correction for C-arm CBCT head scans.	88
4.1	Bone fraction.	90
4.2	The workflow of the multi-pass algorithm for the first and higher-order corrections.	94
4.3	ROIs to compute the robust coefficient of variation.	95
4.4	Water and bone corrections for the head phantom (low energy)	96
4.5	Water and bone corrections for the head phantom (high energy)	97
4.6	Water and bone corrections for the jaw phantom (low energy).	98
4.7	Water and bone corrections for the jaw phantom (high energy)	99
4.8	The minimization of normalized inconsistency measure during higher-order corrections.	100
4.9	GCC-based water and bone corrections for clinical data.	102
4.10	Attenuation profiles (clinical data).	103
4.11	FBCC-based water and bone corrections for clinical data.	103
4.12	SCC-based water and bone corrections for clinical data.	104
4.13	GCC-based corrections for metal artifact reduction.	104

List of Tables

3.1	NLOPT optimization parameters (water correction).	54
3.2	CBCCT system geometry parameters.	57
3.3	X-ray spectra simulation parameters.	57
3.4	Robust coefficient of variation C_v^r after water corrections.	62
3.5	Median of attenuation values (HU).	63
3.6	Summary of comparative evaluations of consistency conditions.	82
4.1	NLOPT optimization parameters (bone corrections).	93
4.2	Robust coefficient of variation C_v^r after water and bone corrections.	101

1 Introduction

1.1 Motivation

Since their discovery by Wilhelm Conrad Röntgen in 1895 [89], X-rays have been used for non-invasive and non-destructive imaging in medicine, industry, science, and archaeology. In the first half of the 20th century, clinical X-ray imaging was constrained to 2D projection radiography and fluoroscopy, where the soft tissue contrast is limited due to overlapping structures. Sir Godfrey Hounsfield and colleagues of EMI Group Limited developed the first X-ray Computed Tomography (CT) device and pioneered 2D cross-sectional X-ray imaging [47]. Since then, many generations of CT systems have been developed and brought into clinical practice. We have witnessed breakthroughs in CT instrumentation and algorithms, including cone-shaped X-ray beam, slip ring technology, digital multi-row detectors, and Graphics Processing Unit (GPU)-accelerated volumetric reconstruction. The major benefits of these advances are the reduction of scan time and increased patient safety and comfort. Third-generation helical Multi-Detector CT (MDCT) scanners (Fig. 1.1a) are widely employed for diagnostic imaging.

Large area digital Flat Panel Detector (FPD) or Flat Detector (FD) are widely used for acquiring 2D projection images in fluoroscopy, radiography, and mammography. Compared with multi-row detectors of MDCT, the large volume coverage in the longitudinal direction, ultra-high spatial resolution, and isotropic pixels enable FPDs to depict fine anatomical details in the projection images and facilitate the steering of catheters and surgical instruments during interventional procedures. Cone Beam Computed Tomography (CBCT) systems equipped with a digital FPD are the latest iteration of third-generation CT scanners [48]. In this thesis, the general term CBCT is used for any FPD-based CBCT system. In contrast to MDCT, the high resolution CBCT images can be used for assessing coronary plaques and micro-calcifications in cardiovascular and breast imaging. C-arm CBCT scanners (Fig. 1.1b), where the X-ray source and the FPD are mounted on a robotic C-shaped arm, revolutionized interventional and intraoperative imaging by facilitating accurate image-guided procedures and 3D navigation. The increased adoption of C-arm CBCT in interventional and intraoperative settings is mainly due to its portability, increased patient access, and the feasibility of performing 3D volumetric imaging and 2D real-time fluoroscopy. Clinical CBCT systems have found applications in radiation therapy, orthopedic, breast, and extremity imaging. CBCT systems are also utilized for non-destructive testing in the industry and automated inspection for security.



(a) MDCT scanner, Siemens Somatom Definition (b) C-arm CBCT scanner, Siemens Artis Q [7]. AS [8].

Figure 1.1: MDCT and C-arm CBCT scanners. Reprinted with permission from Siemens Healthineers, Erlangen, Germany.

The investigation and development of novel artifact correction methods to improve image quality started soon after the development of CT scanners. The physical phenomena of beam hardening and scattering violate the inherent assumption of the linear model describing the CT image formation. The polychromatic X-ray spectrum and the energy-dependent attenuation properties of the imaged object underestimate the total attenuation values of CT projections. After reconstruction, the projection error is transferred to the volume and appears as beam hardening artifacts [26]. In clinical CT, the main manifestations of beam hardening artifacts are [26]:

1. Cupping artifacts are characterized by the in-homogeneity of voxel values where the CT numbers gradually decrease from the periphery to the interior of the imaged object.
2. Streak artifacts appear as dark bands between high attenuation of structures, predominantly visible between bones and metals.
3. Spill-over artifacts are mainly visible in head scans, preventing well-defined bone-tissue boundaries due to the spill-over of the skull to the brain region.

Beam hardening artifacts reduce the low contrast resolution and thereby dampen the soft tissue imaging capability. In interventional imaging, the mitigation of beam hardening artifacts is essential to detect bleeding after a stroke or injury [82]. Beam hardening artifacts also affect the accuracy of quantitative or radiomics studies based on CT images. In industrial and security CBCT systems, beam hardening correction is crucial for reliable automated inspection and accurate material characterization.

Projection linearization is the most widely adopted method for beam hardening correction, where the non-linear error due to the underestimation of projection values

is corrected with a polynomial expression [44] [55]. The coefficients of the correction polynomial are estimated during the calibration of the CT device using homogeneous phantoms. Due to the abundance of water molecules in the human body, the water and soft tissues exhibit similar attenuation properties. Homogeneous water phantoms are used to calibrate clinical CT scanners, and polynomial-based projection linearization is commonly known as water correction.

The attenuation properties of high density and calcium-rich cortical bones differ from those of water and soft tissues. Hence, water correction alone is insufficient to eliminate the beam hardening artifacts from clinical CT images. Joseph and Spital proposed reducing bone-induced residual artifacts using the forward projections of bone structures [52]. The effective correction parameters are estimated by phantom-based calibrations or using prior knowledge about X-ray and attenuation (water and bone) spectra. Subsequently, many algorithms have been published for the correction of bone-induced beam hardening artifacts [49] [58] [73].

Several calibration-free beam hardening corrections have been proposed to eliminate the tedious and recurrent calibrations and the need for prior knowledge about X-ray and attenuation spectra. The prominent and computationally efficient algorithms involve calculating the correction parameters by minimizing the Total Variation (TV) of the corrected volume [58] [61]. TV-based methods yield sub-optimal corrections when the projections are corrupted with inevitable Poisson noise. Tang et al. initiated the attempt to compute polynomials by enforcing consistency conditions on uncorrected projections [88]. Consistency conditions are the mathematical expressions of the redundancy exhibited by the over-determined CT projection values (Sec. 2.6). Violation of the assumptions of the linear forward model generates inconsistent projections. Therefore, the polynomials can be directly estimated from the projection data by enforcing the necessary conditions which need to be strictly satisfied by the artifact-free projections. However, Helgason-Ludwig Consistency Conditions (HLCC) employed by Tang et al. are constrained by the need for CBCT systems with a perfect circular source trajectory and polychromatic projections without additional artifacts like scatter. Hence, HLCC-based corrections are not optimal for CBCT systems like interventional C-arm CT, where a perfect circular source trajectory is not feasible due to the mechanical constraints on robotic C-arms.

1.2 Contributions

In this thesis, calibration-free and projection data-driven beam hardening correction algorithms are discussed. The main contributions are the algorithms to estimate the parameters of the state-of-the-art correction models by enforcing consistency conditions on a set of projection pairs. By utilizing the pair-wise cone beam consistency conditions, the requirement of a perfect circular source trajectory is eliminated. Besides, our studies have proven the feasibility of the correction when the projections are corrupted with Poisson noise and other geometrical and measurement errors. The

algorithm to estimate the polynomial coefficients for water or mono-material correction using Grangeat Consistency Conditions (GCC) was introduced in the following conference paper:

- Shiras Abdurahman, Robert Frysch, Richard Bismark, Michael Friebe, and Georg Rose. Calibration free beam hardening correction using grangeat-based consistency measure. In *2016 IEEE Nuclear Science Symposium and Medical Imaging Conference Proceedings (NSS/MIC)*, pages 1–3. IEEE, 2016

The proposed method was extended to include bone correction, and the algorithm for the concurrent estimation of water and bone correction polynomials using GCC was published in the following journal article:

- Shiras Abdurahman, Robert Frysch, Richard Bismark, Steffen Melnik, Oliver Beuing, and Georg Rose. Beam hardening correction using cone beam consistency conditions. *IEEE Transactions on Medical Imaging*, 37(10):2266–2277, 2018

The multi-pass formulation of GCC-based algorithms to correct bone and metal-induced higher-order artifacts was published in two conference papers:

- Shiras Abdurahman, Robert Frysch, Richard Bismark, Oliver Beuing, and Georg Rose. A complete scheme of empirical beam hardening correction using grangeat consistency condition. In *2018 IEEE Nuclear Science Symposium and Medical Imaging Conference Proceedings (NSS/MIC)*, pages 1–5. IEEE, 2018
- Shiras Abdurahman, Robert Frysch, and Georg Rose. Reduction of beam hardening induced metal artifacts using consistency conditions. In *15th International Meeting on Fully Three-Dimensional Image Reconstruction in Radiology and Nuclear Medicine*, volume 11072, page 110721S. International Society for Optics and Photonics, 2019

In the following conference paper, we demonstrated that optimizing the polynomial coefficients is feasible by enforcing pair-wise Fan Beam Consistency Conditions (FBCC):

- Shiras Abdurahman, Robert Frysch, Steffen Melnik, and Georg Rose. Beam hardening correction using pair-wise fan beam consistency conditions. In *15th International Meeting on Fully Three-Dimensional Image Reconstruction in Radiology and Nuclear Medicine*, volume 11072, page 110721T. International Society for Optics and Photonics, 2019

The preliminary results of estimating kernel parameters for scatter correction were published in the following conference paper:

- Shiras Abdurahman, Robert Frysch, and Georg Rose. Scatter correction using pair-wise fan beam consistency conditions. In *15th International Meeting on Fully Three-Dimensional Image Reconstruction in Radiology and Nuclear Medicine*, volume 11072, page 110722I. International Society for Optics and Photonics, 2019

Finally, a comparative evaluation of GCC, FBCC, and Smith Consistency Conditions (SCC) guided beam hardening corrections has been submitted as the following journal article:

- Shiras Abdurahman, Robert Frysch, Tim Pfeiffer, Oliver Beuing, and Georg Rose. Comparative evaluation of cone-beam consistency conditions for beam hardening correction. *IEEE Transactions on Radiation and Plasma Medical Sciences*, 2021

All author’s publications are listed in the List of Own Publications.

1.3 Organization of the Thesis

Chapter 2 contains a concise overview of the theoretical background on which the consistency condition-based beam hardening corrections are formulated. The chapter begins with the descriptions of X-ray physics and the major CBCT system components. After introducing the CBCT geometry and integral transforms, the reconstruction of 3D volumes is described, along with the derivation of 2D parallel and fan beam reconstruction formulas. Subsequently, three pair-wise cone beam data consistency conditions are explained. The chapter concludes with an in-depth discussion of beam hardening artifacts and the state-of-the-art correction methods, as well as a short overview of other major artifacts mentioned in this thesis. The proofs of the selected equations are given in Appendices.

Chapter 3 describes the data-driven beam hardening correction for mono-material objects using cone beam consistency conditions. The constrained optimization algorithms are discussed, along with the implementation details to enable the reader to reproduce the presented results. The results from the real and simulated datasets are displayed to demonstrate the efficacy of the correction algorithms. Detailed studies are performed to stress test the algorithms under different artifacts for a comparative evaluation of consistency conditions. The comparison studies lead to the ranking of consistency conditions based on their performance and robustness.

Chapter 4 discusses the reduction of higher-order beam hardening artifacts after water correction. The CC-based algorithms utilizing the three different correction models are discussed. We show that the consistency conditions provide a framework to compare artifact correction models.

The final chapter summarizes the algorithms and results and discusses potential future works to enhance CBCT image quality using consistency conditions.

1.4 Mathematical Notation and Units

The N -dimensional vectors (e.g., $\mathbf{f} \in \mathbb{R}^N$) are denoted by italic and bold letters. The unit vectors are marked with a hat symbol ($\hat{\cdot}$) to distinguish them from regular vectors (e.g., $\hat{\mathbf{u}} \in \mathbb{S}^{N-1}$). In general, we consider the N -dimensional vector as a column vector with N rows (e.g., $\mathbf{f} \in \mathbb{R}^{N \times 1}$). The row vector is distinguished by a superscript T to denote the transpose operation on a column vector (e.g., $\mathbf{f}^T \in \mathbb{R}^{1 \times N}$). The matrices with M rows and N columns are represented by upper case, italic and bold English letters (e.g., $\mathbf{P} \in \mathbb{R}^{M \times N}$). Italic and non-bold letters are used to denote the scalar functions and values. Zero-based indexing is used to represent the elements of vectors and matrices. f_i denotes the $i + 1$ -th element of the vector \mathbf{f} and $p_{i,j}$ represents the element of \mathbf{P} in the $i + 1$ -th row and $j + 1$ -th column. The $i + 1$ -th row and $j + 1$ -th column vectors of matrix \mathbf{P} are denoted by \mathbf{p}_i^T and \mathbf{p}_j . \langle, \rangle denotes the inner product of two vectors or functions and $\| \cdot \|$ represents the Euclidean norm. The unit of length is millimeters, and the angles are measured in radians.

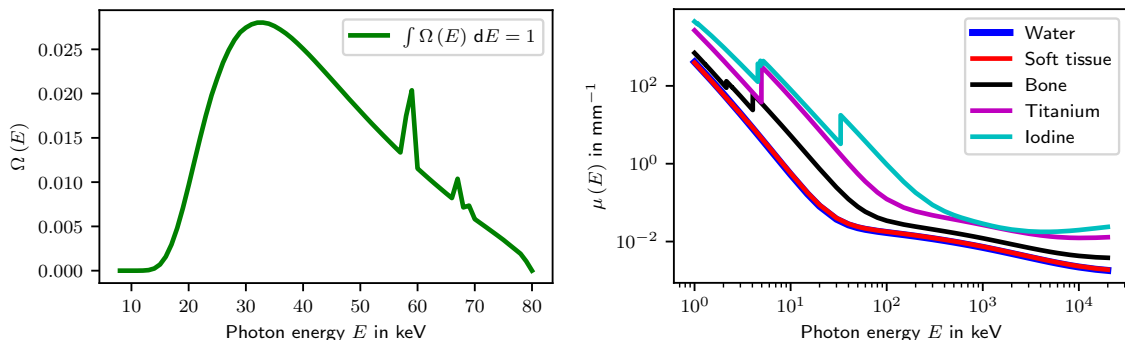
2 Theoretical Background

2.1 CT Physics and System Components

2.1.1 X-ray Generation

X-rays (also known as Röntgen rays) are Electro-Magnetic (EM) radiation serendipitously discovered by Wilhelm Conrad Röntgen in 1895. Compared to visible light, X-rays are higher energy and shorter-wavelength EM waves, which can penetrate through the human body to form projection (radiography) and cross-sectional (Computed Tomography, CT) images. As per the wave-particle duality concept in quantum mechanics, X-rays are also considered as packets of particles called photons with no charge and rest mass. This corpuscular nature of X-rays is utilized to illustrate their interaction with the matter and the resultant process of attenuation. The quantized energy of individual photons is denoted by E and typically measured in Kilo Electron Volt (keV).

X-rays for medical imaging and non-destructive testing are generated with a vacuum tube (X-ray tube) consisting of a cathode filament (negative electrode) and a target anode (positive electrode) encased in a glass or metal housing. Applying DC voltage across the X-ray tube initiates the thermionic emission of electrons after heating the filament with the tube current. The negatively charged electrons will be accelerated towards the anode, and their maximum kinetic energy depends on the maximum voltage applied, known as Peak Kilovoltage (kVp). A cup-shaped electrode of cathode assembly focuses the electrons on a small area of anode known as the focal spot [48]. The high-energy and negatively charged electrons collide with the anode causing mainly two types of interactions. First, the incoming electrons will be deflected by the atomic Coulomb field of the positively charged nucleus of anode atoms [48]. Consequently, the loss of kinetic energy of electrons will be converted into X-ray photons as per the law of conservation of energy. This type of radiation is known as Bremsstrahlung radiation and covers the entire X-ray spectrum. The second type of interaction occurs when the electrons transfer their energy to inner shell electrons to liberate them from the electromagnetic force exerted by the atomic nuclei [48]. The resulting positively charged holes of the excited atoms will be filled by the loosely bound outer shell electrons. The energy loss due to the transition results in the production of characteristic X-rays at distinct energy levels. An example plot of the unit area normalized spectrum (number of photons with respect to its energy) of Bremsstrahlung radiation and the characteristic peaks is displayed in Fig. 2.1a.



(a) Normalized X-ray spectrum: Bremsstrahlung and characteristic peaks. The tabulated spectrum was estimated with Spekcalc software where $kVp = 80$ keV [75].
 (b) Linear attenuation coefficients μ of water, soft-tissues, bone, titanium, and iodine. The tabulated spectra were accessed from the database of National Institute of Standards and Technology (NIST) [9].

Figure 2.1: X-ray and attenuation spectra.

For a specific anode material, the number of emitted X-ray photons is determined by the number of electrons from the cathode and the exposure time. The total X-ray exposure is quantified with the product of X-ray tube current and exposure time and measured in Milli Ampere Second (mAs).

2.1.2 X-ray Attenuation

After emanating from the focal spot, X-ray photons undergo the process of attenuation during their transmission through the imaged object (patient in clinical imaging). For the photons of energy less than 1000 keV, the attenuation mainly comprises the physical phenomena of photoelectric absorption, Compton, and Rayleigh scatterings [80]. In photoelectric absorption, the incoming photon ceases to exist after transferring its energy to tightly bound inner shell electron and ionizing the atom [48]. As a result, high-energy outer shell electrons move to the positively charged holes, and their transition energy will be emitted as characteristic rays [80]. In clinical imaging, the low energy characteristic radiation will be eventually absorbed by the patient's body and does not play any role in image formation [48]. The probability of photoelectric absorption (photoelectric cross-section) is proportional to the fourth power of atomic number [80]. Therefore, the attenuation due to photoelectric absorption is higher in bone and metals than in soft tissues or water.

The other dominant phenomenon of attenuation in clinical imaging is Compton scattering (incoherent scattering). After their interaction with the electrons and ionizing the atoms, the incoming photons lose energy and will be deviated from their propagation path. The extent of deflection is measured as the scattering angle [48]. The higher energy photons primarily undergo forward scattering, where the scattering

angle is less than 90° . The forward scattering acts as a secondary radiation source and degrades the quality of projection radiographs and CT images. The low-energy photons are subjected to back-scattering, where the scattering angle is greater than 90° [48]. The back-scattered photons will be absorbed by the X-ray tube's metal housing and do not contribute to image formation [48].

In Rayleigh scattering, the incoming photons transfer their energy to electrons and force them into oscillations in their orbits resonant with the photon's electrical field [80]. The electrons lose their energy by emitting photons in the forward direction but with a possible small deflection [66]. The emitted photons will have the same energy as those of incoming photons. Since the energy of incoming photons is less than the binding energy of electrons, Rayleigh scattering does not ionize the atom. Hence, the probability of Rayleigh interaction at higher energies is very low [86]. Rayleigh scattering cannot be ignored in mammography and Digital Breast Tomosynthesis (DBT), where the low-energy X-rays are used for better soft tissue contrast [86].

Thus, the process of attenuation refers to the demise or the deflection of photons from their original linear propagation path. Consider the X-ray photons of energy E pass through a homogeneous medium where the length of the medium along the photon transport direction is denoted by l . The instantaneous X-ray intensity (a measure of the number of photons) along the propagation path is denoted by $I(E)$. The attenuation of X-ray intensity is governed by the law of exponential decay where the decrease in intensity is proportional to its current value [1]:

$$\frac{dI(E)}{dl} = -\mu(E) I(E) \quad (2.1)$$

$\mu(E) \geq 0$ denotes the energy-dependent linear attenuation coefficient of the medium (exponential decay constant). The transmitted (non-attenuated) X-ray intensity $I_t(E)$ can be mathematically expressed by solving the above first-order ordinary differential equation, and its closed-form solution is widely known as Beer-Lambert law:

$$I_t(E) = I_0(E) e^{-\mu(E)l} \quad (2.2)$$

where $I_0(E)$ represents the incident X-ray intensity prior to the attenuation by the medium. The derivation of the equation is given in Appendix .1.

For a heterogeneous medium where the spatial (linear) distribution of attenuation coefficients is denoted by $\mu(x, E)$, $x \in [0, l]$, the above equation can be reformulated as:

$$I_t(E) = I_0(E) e^{-\int_0^l \mu(x, E) dx} \quad (2.3)$$

By considering the medium or imaged object is situated in attenuation-free vacuum or air, the limits of integration of the above equation can be modified:

$$I_t(E) = I_0(E) e^{-\int_0^\infty \mu(x, E) dx} \quad (2.4)$$

If an ideal source generates monochromatic X-rays of energy E_m , the total attenuation along the photon propagation direction (extinction or ray sum) is given by:

$$\begin{aligned}
 g_m &= \int_0^{\infty} \mu(x, E_m) dx \\
 &= -\ln \left(\frac{I_t(E_m)}{I_0(E_m)} \right)
 \end{aligned}
 \tag{2.5}$$

We refer to the total attenuation measured using monochromatic X-radiation as monochromatic attenuation or projection value.

Apart from photon energy, the attenuation properties of a material depend on its effective atomic number. The contrast of the clinical X-ray images is mainly determined by the difference in attenuation coefficients of soft tissues, bones, implants (fabricated using titanium or stainless steel), and radio-contrast agents (e.g., iodine). Fig. 2.1b shows the attenuation spectrum of water (density = 1.0 g/cm^3) [6], soft tissue (density = 1.06 g/cm^3) [2], calcium-rich cortical bone (density = 1.85 g/cm^3) [3], titanium (density = 4.54 g/cm^3) [5] and iodine (density = 4.93 g/cm^3) [4]. We can infer from the figure that the degree of attenuation decreases non-linearly with the increase in photon energy. Due to the difference in attenuation, bone-tissue contrast is significant even at higher energies. The attenuation spectra of soft tissues can be approximated with that of water due to the abundance of water molecules in soft tissues.

In practice, X-ray sources of clinical imaging systems are polychromatic with a wide photon energy range. The maximum energy of the source is denoted by E_{max} . As Fig. 2.1b demonstrates, the low-energy photons are strongly attenuated during their propagation through the human body. Due to their low transmittance, low-energy photons are unable to contribute to the final image contrast. The excess ionization due to the increased photoelectric absorption is harmful to the patient and can damage the DNA of cells. To reduce the absorbed dose by the patient, the X-ray spectrum is modulated by applying filters to strongly attenuate the low-energy photons before reaching the patient. The most widely used filter materials are thin sheets of aluminium and copper. E_{min} denotes the minimum energy of X-ray photons after filtration.

2.1.3 X-ray Detection

In radiography and CT, the transmitted radiation is detected with an X-ray detector. Though many analog and digital detectors have been developed over the years, we limit our discussion to energy integrating digital Flat Panel Detector (FPD). The majority of the FPDs comprise X-ray scintillator crystals (e.g., cesium iodide, CsI) and photodiode arrays (e.g., amorphous silicon, a-Si) to perform a two-level conversion process [85]. Scintillator crystal converts the incoming X-ray radiation to visible light,

and the photodiode converts light photons to electric charge. An Analog to Digital Converter (ADC) of detector electronics amplifies the electrical charge and converts it to a digital signal for processing. FPDs are relatively lightweight and can be easily mounted on C-arms for interventional imaging [66].

An energy integrating detector accumulates X-ray intensities during the exposure time. The efficiency of the detector to convert incoming X-ray radiation of various energies to electric signal is characterized by the detector spectral response $\mathcal{D}(E)$, $0 \leq \mathcal{D}(E) \leq 1 \forall E$. For a polychromatic source where the X-ray energy $E \in [E_{min}, E_{max}]$, the measured (detected) intensity of incident X-rays can be estimated as follows:

$$I_0^m = \int_{E_{min}}^{E_{max}} I_0(E) \mathcal{D}(E) dE \quad (2.6)$$

If \mathcal{N}_p is the total number of emitted photons of all energies and $\Omega(E)$ is the polychromatic X-ray spectrum normalized to a unit area (Fig. 2.1a), $I_0(E)$ is given by:

$$I_0(E) = \mathcal{N}_p \Omega(E) \quad (2.7)$$

By substituting Eq. 2.7 in Eq. 2.6,

$$I_0^m = \mathcal{N}_p \int_{E_{min}}^{E_{max}} \Omega(E) \mathcal{D}(E) dE \quad (2.8)$$

The measured X-ray intensity after attenuation is given as:

$$\begin{aligned} I_t^m &= \int_{E_{min}}^{E_{max}} I_t(E) \mathcal{D}(E) dE \\ &= \int_{E_{min}}^{E_{max}} I_0(E) e^{-\int_0^\infty \mu(x,E) dx} \mathcal{D}(E) dE, \quad \text{after substituting Eq. 2.4} \quad (2.9) \\ &= \mathcal{N}_p \int_{E_{min}}^{E_{max}} \Omega(E) \mathcal{D}(E) e^{-\int_0^\infty \mu(x,E) dx} dE \end{aligned}$$

Similar to Eq. 2.5, the measured polychromatic total attenuation or projection

value can be computed as:

$$\begin{aligned}
 g_p &= -\ln \left(\frac{I_t^m}{I_0^m} \right) \\
 &= -\ln \left(\frac{\int_{E_{min}}^{E_{max}} \Omega(E) \mathcal{D}(E) e^{-\int_0^\infty \mu(x,E) dx} dE}{\int_{E_{min}}^{E_{max}} \Omega(E') \mathcal{D}(E') dE'} \right) \\
 &= -\ln \left(\int_{E_{min}}^{E_{max}} \frac{\Omega(E) \mathcal{D}(E)}{\int_{E_{min}}^{E_{max}} \Omega(E') \mathcal{D}(E') dE'} e^{-\int_0^\infty \mu(x,E) dx} dE \right) \\
 &= -\ln \left(\int_{E_{min}}^{E_{max}} \eta(E) e^{-\int_0^\infty \mu(x,E) dx} dE \right)
 \end{aligned} \tag{2.10}$$

where $\eta(E)$ (also known as system weighting function) is the unit area normalized detected spectrum comprising the emitted X-ray spectrum, filtration, and detector response [53] [43]:

$$\eta(E) = \frac{\Omega(E) \mathcal{D}(E)}{\int_{E_{min}}^{E_{max}} \Omega(E') \mathcal{D}(E') dE'} \tag{2.11}$$

2.2 X-Ray Projection Imaging and CBCT

Flat Panel Detector (FPD)-equipped cone beam X-ray systems are used for 2D radiographic imaging. The large area detector, ultra-high spatial resolution, and isotropic pixels enable the visualization of anatomical details necessary for diagnosis and intra-operative interventions. Compared to conventional film radiography, the high frame rate of FPD facilitates the real-time acquisition of fluoroscopic projection images. Digital Subtraction Angiography (DSA) is a fluoroscopy technique to visualize blood vessels and is widely utilized for angiographic interventions.

By rotating the cone beam X-ray source and FPD pair around the patient, 2D cross-sectional images can be reconstructed from 2D projection views, making volumetric reconstruction feasible with a single rotation. The reconstructed volumes of CBCT enable 3D characterization of complex anatomical structures, including 3D visualization of contrast-enhanced vessels (3D rotational DSA) [71]. C-arm CBCT, where the X-ray source and FPD are mounted on a C-shaped arm, facilitates 2D projection radiography, fluoroscopy, DSA, and 3D CBCT in a single unit and is widely employed in interventional suites.

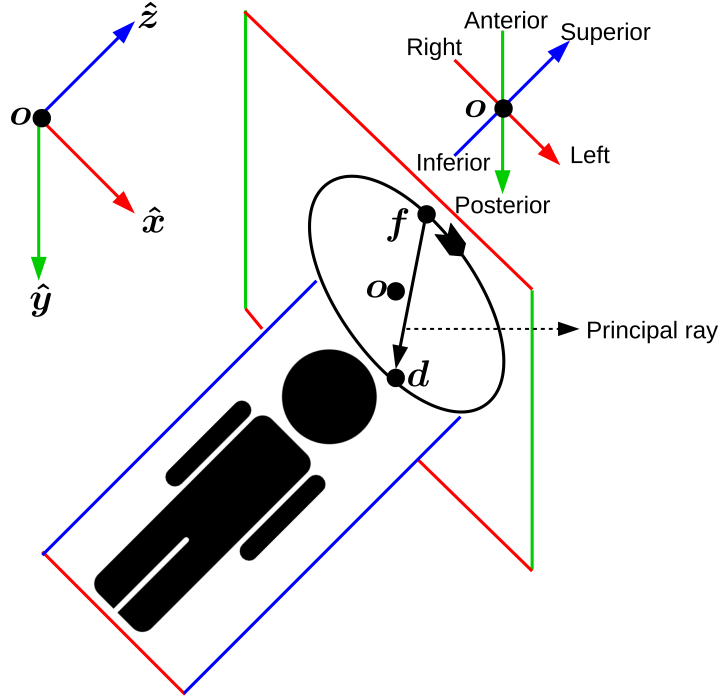


Figure 2.2: Perspective view of CBCT geometry and World Coordinate System (WCS).

2.3 CBCT Geometry

This section introduces CBCT geometry parameters and their notations to describe the 3D reconstruction algorithm and consistency conditions.

2.3.1 World Coordinate System

World Coordinate System (WCS) is used to represent points in 3D world space where the CT system and the imaged object are located, and the CT image is sampled. WCS is a Cartesian coordinate system and is fixed during the scan. We utilize the Left Posterior Superior (LPS) orientation of the DICOM patient coordinate system to define WCS coordinate axes, as shown in Fig. 2.2. The positive \hat{x} , \hat{y} , and \hat{z} axes are oriented from right to left, anterior to posterior, and from inferior to superior of the patient, respectively. The origin of WCS is considered as the isocenter ($\mathbf{o} \in \mathbb{R}^3$) of the CT system. The basis vectors of WCS are the standard basis of 3D Euclidean space:

$$\hat{x} = \begin{bmatrix} 1 \\ 0 \\ 0 \end{bmatrix}, \hat{y} = \begin{bmatrix} 0 \\ 1 \\ 0 \end{bmatrix}, \hat{z} = \begin{bmatrix} 0 \\ 0 \\ 1 \end{bmatrix} \quad (2.12)$$

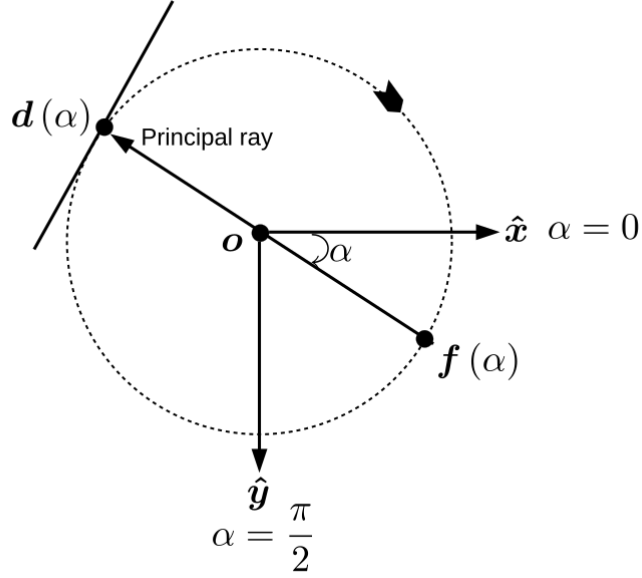


Figure 2.3: Rotation plane of source-detector assembly and the gantry rotation angle.

As shown in Fig. 2.2, $\mathbf{f} \in \mathbb{R}^3$ denotes the 3D position vector of the X-ray source. We assume a punctiform X-ray source, which is termed as the focal spot, a point on the X-ray anode from where X-ray photons are emitted. In practice, this assumption is often not valid and can cause spatially varying resolution properties of the reconstructed image. R_f denotes the distance from the isocenter (center of rotation) to the focal spot (source-isocenter distance). D is the perpendicular distance from the focal spot to the detector plane, and the orthogonal ray is referred to as the principal ray. $\mathbf{d} \in \mathbb{R}^3$ denotes the point where the principal ray intersects the detector plane.

2.3.2 Source Detector Coordinate System

In the axial scans of clinical CBCT systems, the source-detector pair rotates around the patient and acquires a series of 2D projections/views while the patient remains stationary lying on a table. As shown in Fig. 2.2, the \hat{z} axis of WCS is chosen as the rotation axis. For a stable CBCT system, the focal spot trajectory (source orbit) is a full (full scan) or partial (short scan) circle, and R_f is its radius. The circular focal spot trajectory is parameterized by rotation angle $\alpha \in \mathbb{R} : \alpha \in [0, 2\pi)$ and an arbitrary point on the trajectory is denoted by $\mathbf{f}(\alpha)$. α is the angle between the principal ray and the positive \hat{x} axis, as depicted in Fig. 2.3. $\alpha = 0$, when the focal spot is positioned on the positive \hat{x} axis, and the angle increases during the clockwise rotation of the source-detector assembly. The matrix $\mathbf{R}_z(\alpha) \in \mathbb{R}^{3 \times 3}$ describes the

rotation around the \hat{z} axis.

$$\mathbf{R}_z(\alpha) = \begin{bmatrix} \cos \alpha & -\sin \alpha & 0 \\ \sin \alpha & \cos \alpha & 0 \\ 0 & 0 & 1 \end{bmatrix} \quad (2.13)$$

By assuming the \hat{z} -coordinate of the points in the rotation plane is 0, the 3D position vector of the focal spot is given by:

$$\mathbf{f}(\alpha) = \mathbf{R}_z(\alpha) \begin{bmatrix} R_f \\ 0 \\ 0 \end{bmatrix} \quad (2.14)$$

CBCT systems acquire projections at regular intervals under ideal conditions during their rotation, and the angular sampling width is represented by $\Delta\alpha$. The total number of projections acquired during a single scan is denoted by N_α . Each projection/view is indexed by $i \in \mathbb{N} : i \in [0, N_\alpha - 1]$ and the corresponding rotation angle is denoted by $\alpha_i \in \mathbb{R}$. α_0 , and $\alpha_{N_\alpha-1}$ represent the angles that correspond to the initial and final projections and characterize the circular source trajectory. The angle associated with each projection index can be computed with the following equation:

$$\alpha_i = (\alpha_0 + i \Delta\alpha) \bmod 2\pi, \quad i = 0, \dots, N_\alpha - 1 \quad (2.15)$$

Source Detector Coordinate System (SDCS) is the rotated coordinate system of the source-detector assembly. The orthonormal basis vectors of SDCS are parameterized by rotation angle α and denoted by $\hat{\mathbf{u}}(\alpha)$, $\hat{\mathbf{v}}(\alpha)$, and $\hat{\mathbf{w}}(\alpha)$. $\hat{\mathbf{u}}(\alpha)$, and $\hat{\mathbf{v}}(\alpha)$ orient in the direction of detector columns and rows while $\hat{\mathbf{w}}(\alpha)$ is the direction of the orthogonal ray towards the detector plane from the focal spot, the origin of SDCS. If the detector plane is perfectly aligned and not tilted around the $\hat{\mathbf{x}}$ or $\hat{\mathbf{y}}$ axis, it is assumed that, $\hat{\mathbf{u}}(0) \parallel \hat{\mathbf{y}}$, $\hat{\mathbf{v}}(0) \parallel -\hat{\mathbf{z}}$ and $\hat{\mathbf{w}}(0) \parallel -\hat{\mathbf{x}}$. The implicit rotation matrix $\mathbf{R}_0 \in \mathbb{R}^{3 \times 3}$ can be formed by stacking the basis vectors of SDCS at $\alpha = 0$ row by row:

$$\mathbf{R}_0 = \begin{bmatrix} \hat{\mathbf{u}}(0)^T \\ \hat{\mathbf{v}}(0)^T \\ \hat{\mathbf{w}}(0)^T \end{bmatrix} = \begin{bmatrix} \hat{\mathbf{y}}^T \\ -\hat{\mathbf{z}}^T \\ -\hat{\mathbf{x}}^T \end{bmatrix} \quad (2.16)$$

The SDCS basis vectors at arbitrary angle α are the rows of the rotation matrix $\mathbf{R}(\alpha)$, the product of \mathbf{R}_0 and $\mathbf{R}_z(\alpha)$:

$$\mathbf{R}(\alpha) = \begin{bmatrix} \hat{\mathbf{u}}(\alpha)^T \\ \hat{\mathbf{v}}(\alpha)^T \\ \hat{\mathbf{w}}(\alpha)^T \end{bmatrix} = \mathbf{R}_0 \mathbf{R}_z(\alpha) \quad (2.17)$$

Detector Coordinate System (DCS) is a subspace of SDCS with the origin at \mathbf{d} (the orthogonal projection of focal spot onto the detector plane) and basis vectors $\hat{\mathbf{u}}(\alpha)$ and $\hat{\mathbf{v}}(\alpha)$. The position vector of an arbitrary point on the detector plane can be mathematically expressed as $u \hat{\mathbf{u}}(\alpha) + v \hat{\mathbf{v}}(\alpha) + D(\alpha) \hat{\mathbf{w}}(\alpha)$ in SDCS and $u \hat{\mathbf{u}}(\alpha) + v \hat{\mathbf{v}}(\alpha)$ in DCS.

2.3.3 Pixel Coordinate System

From the geometric viewpoint, a Flat Panel Detector (FPD) is considered a rectangular grid (2D matrix) of pixels. The number of columns and rows of the matrix are represented by N_u and N_v . The centroid of each detector element (pixel) is identified with the column index $u_i \in \mathbb{N} : u_i \in [0, N_u - 1]$ and row index $v_i \in \mathbb{N} : v_i \in [0, N_v - 1]$. It is assumed that the detector is equidistant sampled along column and row directions and the sampling intervals are the pixel width Δu and height Δv .

Pixel Coordinate System (PCS) is used to represent any point on the detector with the coordinates $u^{pcs} \in \mathbb{R} : u^{pcs} \in [-0.5, N_u - 0.5]$ and $v^{pcs} \in \mathbb{R} : v^{pcs} \in [-0.5, N_v - 0.5]$. The origin of the PCS is the centroid of the pixel located at the top left corner when $\alpha = \frac{3\pi}{2}$ and viewing direction is from the source to the detector (top view). At each pixel centroid, $u^{pcs} = u_i$ and $v^{pcs} = v_i$. PCS is utilized to access the pixel value of the corresponding point in DCS, and the coordinate transformation from DCS to PCS can be performed with an affine transform (scaling + translation):

$$\begin{bmatrix} u^{pcs} \\ v^{pcs} \end{bmatrix} = \begin{bmatrix} \frac{1}{\Delta u} & 0 \\ 0 & \frac{1}{\Delta v} \end{bmatrix} \begin{bmatrix} u \\ v \end{bmatrix} + \begin{bmatrix} u_0^{pcs} \\ v_0^{pcs} \end{bmatrix} \quad (2.18)$$

$[u_0^{pcs}, v_0^{pcs}]^T$ is the origin of DCS (principal point) in PCS. DCS is used to define any point on the infinite detector plane where the values of coordinates are measured in millimeters. We use DCS in the derivation of analytical reconstruction formulas. The coordinate values of PCS are measured in number of detector pixels, and the fractional value indicates the point between adjacent pixel centroids.

2.3.4 Volume Geometry

In CT imaging, reconstructed volume is the spatial distribution of linear attenuation coefficients $\mu(\mathbf{x})$, where $\mathbf{x} \in \mathbb{R}^3$ denotes an arbitrary 3D point in WCS. $\mu(\mathbf{x})$ is assumed to be a sufficiently regular (differentiable at least twice) and has a compact support of radius R_{FOV} ($\mu(\mathbf{x}) = 0 \forall \|\mathbf{x}\| > R_{FOV}$) [31]. R_{FOV} is the radius of the cylindrical Field of View (FOV). For numerical reconstruction, the volume is discretized on a grid of $N_x \times N_y \times N_z$ voxels in x, y and, z directions as the number of columns, rows, and slices of the volume. $\Delta x, \Delta y$, and Δz represent voxel width, height, and depth. The volume is also specified by the reconstruction center (volume mid-point) \mathbf{x}_{rc} , a 3D point in WCS. The centroid of each voxel is identified by the column x_i , row y_i , and slice z_i indices. The 3D position vector of first voxel ($x_i = y_i = z_i = 0$) in WCS is given by:

$$\mathbf{x}_0 = \mathbf{x}_{rc} - \begin{bmatrix} \frac{(N_x-1)\Delta x}{2} \\ \frac{(N_y-1)\Delta y}{2} \\ \frac{(N_z-1)\Delta z}{2} \end{bmatrix} \quad (2.19)$$

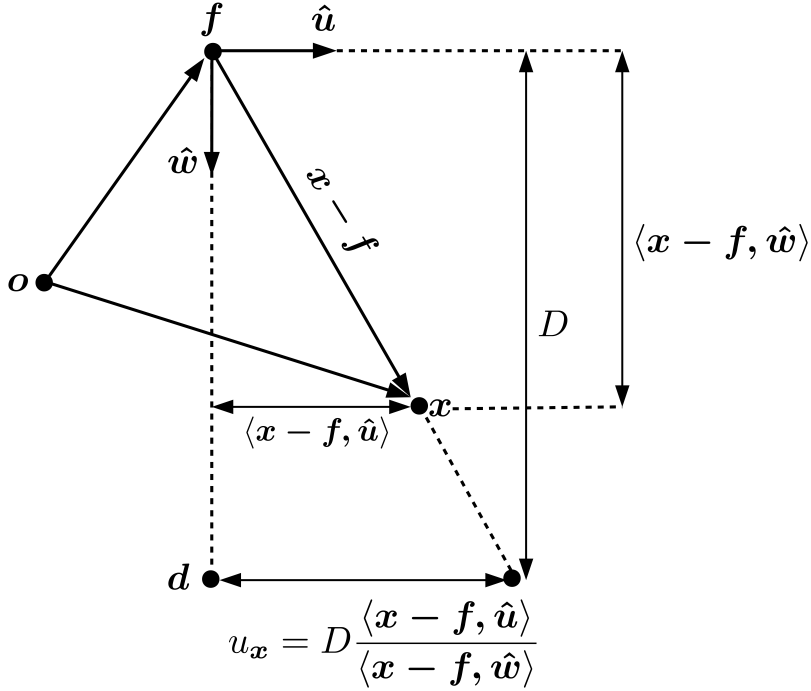


Figure 2.4: Projection geometry of voxel to pixel mapping in the $\hat{u}\hat{w}$ plane.

The coordinates of each voxel centroid in WCS can be computed with the following affine transform:

$$\mathbf{x} = \mathbf{x}_0 + \begin{bmatrix} \Delta x & 0 & 0 \\ 0 & \Delta y & 0 \\ 0 & 0 & \Delta z \end{bmatrix} \begin{bmatrix} x_i \\ y_i \\ z_i \end{bmatrix} \quad (2.20)$$

2.3.5 Projection Geometry

Consider a 3D point \mathbf{x} is projected by an X-ray emanating from the focal spot $\mathbf{f}(\alpha)$ onto the detector plane. The coordinates of the projected point in DCS are given by (Fig. 2.4):

$$\begin{aligned} u_x(\alpha) &= D \frac{\langle \mathbf{x} - \mathbf{f}(\alpha), \hat{u}(\alpha) \rangle}{\langle \mathbf{x} - \mathbf{f}(\alpha), \hat{w}(\alpha) \rangle} \\ v_x(\alpha) &= D \frac{\langle \mathbf{x} - \mathbf{f}(\alpha), \hat{v}(\alpha) \rangle}{\langle \mathbf{x} - \mathbf{f}(\alpha), \hat{w}(\alpha) \rangle} \end{aligned} \quad (2.21)$$

The corresponding point in PCS $[u_x^{pcs}(\alpha), v_x^{pcs}(\alpha)]^T$ can be computed with the Eq. 2.18.

For a mechanically stable CT system with a perfect circular source trajectory (e.g., clinical MDCT, high precision industrial CBCT), the projection geometry at rotation

angle α is determined by the vectors $\mathbf{f}(\alpha)$, $\hat{\mathbf{u}}(\alpha)$, $\hat{\mathbf{v}}(\alpha)$, and $\hat{\mathbf{w}}(\alpha)$. The values of rotation-invariant parameters D , R_f , u_0^{pcs} and v_0^{pcs} are fixed during the scan. By knowing the system geometry parameters and the rotation angle of each projection, the projection geometry of the axial scan can be estimated. The perfect circular trajectory is not practical for C-arm CBCT due to mechanical constraints. Hence, the scalars and the vectors of the geometry parameters are rotationally variant. Apart from $\mathbf{R}_z(\alpha)$, additional rotations around $\hat{\mathbf{x}}$ and $\hat{\mathbf{y}}$ axes are necessary to estimate the final rotation matrix $\mathbf{R}(\alpha)$ if the detector plane is tilted. In this scenario, CBCT systems make use of projection matrices $\mathbf{P}(\alpha) \in \mathbb{R}^{3 \times 4}$ to describe the geometry of cone beam projection. The mapping of a 3D point \mathbf{x} to its corresponding projected location in PCS can be performed as a matrix-vector multiplication [33]:

$$\lambda \begin{bmatrix} u_x^{pcs} \\ v_x^{pcs} \\ 1 \end{bmatrix} = \mathbf{P}(\alpha) \tilde{\mathbf{x}} = \mathbf{P}(\alpha) \begin{bmatrix} x \\ y \\ z \\ 1 \end{bmatrix}, \quad \tilde{\mathbf{x}} \in \mathbb{P}^3 := \mathbb{R}^4 \setminus [0, 0, 0, 0]^T \quad (2.22)$$

$\tilde{\mathbf{x}}$ is the homogeneous representation of \mathbf{x} in 3D projective space (\mathbb{P}^3), where the last element of the homogeneous vector is unity. The pixel coordinates are computed by eliminating the non-zero scaling factor λ as per the following normalization [33]:

$$\begin{aligned} u_x^{pcs} &= \frac{\langle \mathbf{p}_0^T(\alpha), \tilde{\mathbf{x}} \rangle}{\langle \mathbf{p}_2^T(\alpha), \tilde{\mathbf{x}} \rangle} \\ v_x^{pcs} &= \frac{\langle \mathbf{p}_1^T(\alpha), \tilde{\mathbf{x}} \rangle}{\langle \mathbf{p}_2^T(\alpha), \tilde{\mathbf{x}} \rangle} \end{aligned} \quad (2.23)$$

where \mathbf{p}_i^T is the $i+1$ -th row of the projection matrix. The matrices are computed during the geometrical calibration of the scanner using phantoms consisting of marker balls. Utilizing the known point correspondences ($\mathbf{x} \rightarrow [u_x^{pcs}, v_x^{pcs}]^T$) of metal balls, the matrix elements are estimated by solving a system of linear equations with the Singular Value Decomposition (SVD) algorithm [63].

The composition of the projection matrix can be expressed as [41]:

$$\mathbf{P}(\alpha) = \mathbf{K}(\alpha) [\mathbf{R}(\alpha) \quad -\mathbf{R}(\alpha) \mathbf{f}(\alpha)] \quad (2.24)$$

where the intrinsic matrix $\mathbf{K}(\alpha) \in \mathbb{R}^{3 \times 3}$ is given by:

$$\mathbf{K}(\alpha) = \begin{bmatrix} \frac{D(\alpha)}{\Delta u} & 0 & u_0^{pcs}(\alpha) \\ 0 & \frac{D(\alpha)}{\Delta v} & v_0^{pcs}(\alpha) \\ 0 & 0 & 1 \end{bmatrix} \quad (2.25)$$

The individual projection geometry parameters necessary for reconstruction can be extracted from the projection matrix using QR decomposition [41].

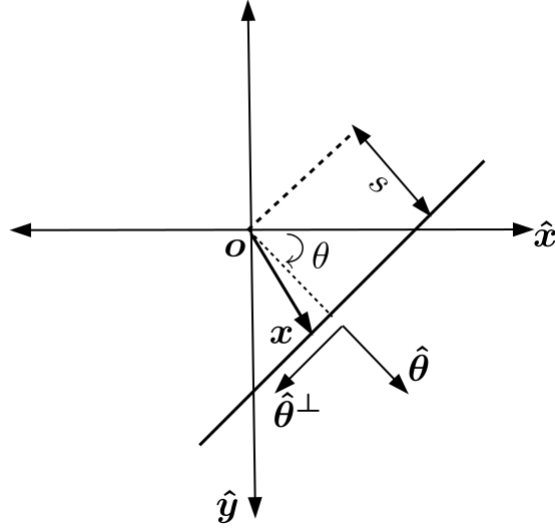


Figure 2.5: Line in 2D.

2.4 Integral Transforms

2.4.1 Radon Transforms

By introducing Radon transform and formulating its inverse, Johann Radon laid the mathematical foundations of analytical CT reconstruction in his paper published in 1917 [79]. In 2D, Radon transform \mathcal{R}_2 of a function μ is defined as the set of line integrals where the lines are denoted by $\mathcal{L}(\theta, s)$ or $\mathcal{L}(\hat{\theta}, s)$.

$$\mathcal{L}(\theta, s) = \mathcal{L}(\hat{\theta}, s) = \left\{ \mathbf{x} \in \mathbb{R}^2 : \langle \mathbf{x}, \hat{\theta} \rangle = s, \hat{\theta} \in \mathbb{S}, s \in \mathbb{R} \right\} \quad (2.26)$$

As shown in Fig. 2.5, θ is the angle between the \hat{x} -axis and the normal vector to the line. $\hat{\theta} = [\cos \theta \ \sin \theta]^T$ denotes the normal vector and s is the orthogonal distance from the origin to the line along $\hat{\theta}$. The line direction is represented by $\hat{\theta}^\perp = [-\sin \theta \ \cos \theta]^T$, unit vector orthogonal to $\hat{\theta}$. The 2D Radon transform of the function $\mu(\mathbf{x})$, $\mathbf{x} \in \mathbb{R}^2$ is formulated as [32] [59]:

$$\begin{aligned} \mathcal{R}_2 \mu(\theta, s) &= \mathcal{R}_2 \mu(\hat{\theta}, s) = \int_{\mathbf{x} \in \mathcal{L}(\hat{\theta}, s)} \mu(\mathbf{x}) \, d\mathbf{x} \\ &= \int_{\mathbf{x} \in \mathbb{R}^2} \mu(\mathbf{x}) \delta(\langle \mathbf{x}, \hat{\theta} \rangle - s) \, d\mathbf{x} \\ &= \int_{l \in \mathbb{R}} \mu(s\hat{\theta} + l\hat{\theta}^\perp) \, dl \end{aligned} \quad (2.27)$$

where δ is the Dirac delta function. The important properties of 2D Radon transform, which are relevant to the reconstruction algorithms mentioned in this thesis, are given below [32]:

1. Linearity: Radon transform inherit this property from the linear integral operator [32].

$$\mathcal{R}_2 \sum_{i=1}^N c_i \mu_i (\hat{\boldsymbol{\theta}}, s) = \sum_{i=1}^N c_i \mathcal{R}_2 \mu_i (\hat{\boldsymbol{\theta}}, s), \quad c_i, \in \mathbb{R} \quad (2.28)$$

2. Periodicity:

$$\mathcal{R}_2 \mu (\theta + 2\pi, s) = \mathcal{R}_2 \mu (\theta, s) \quad (2.29)$$

3. Redundancy/consistency:

$$\mathcal{R}_2 \mu (\theta + \pi, -s) = \mathcal{R}_2 \mu (\theta, s), \quad \text{see Appendix .2 for proof} \quad (2.30)$$

4. Fourier slice theorem: For a fixed angle θ , 2D Radon transform in Fourier domain is defined as:

$$\mathcal{F}_1 \mathcal{R}_2 \mu (\sigma; \hat{\boldsymbol{\theta}}) = \int_{s \in \mathbb{R}} \mathcal{R}_2 \mu (s; \hat{\boldsymbol{\theta}}) e^{-i2\pi s \sigma} ds \quad (2.31)$$

where $\mathcal{R}_2 \mu (s; \hat{\boldsymbol{\theta}}) \in \mathbb{L}^1(\mathbb{R}) : \int_{s \in \mathbb{R}} |\mathcal{R}_2 \mu (s; \hat{\boldsymbol{\theta}})| ds < \infty$

$\sigma \in \mathbb{R}$ is the one dimensional Fourier transform variable representing the spatial frequency in cycles per mm. With the corresponding frequency variable $\boldsymbol{\nu} \in \mathbb{R}^2$, 2D Fourier transform of the function $\mu(\mathbf{x})$ is defined as follows:

$$\mathcal{F}_2 \mu (\boldsymbol{\nu}) = \int_{\mathbf{x} \in \mathbb{R}^2} \mu(\mathbf{x}) e^{-i2\pi \langle \mathbf{x}, \boldsymbol{\nu} \rangle} d\mathbf{x} \quad (2.32)$$

where $\mu(\mathbf{x}) \in \mathbb{L}^1(\mathbb{R}^2) : \int_{\mathbf{x} \in \mathbb{R}^2} |\mu(\mathbf{x})| d\mathbf{x} < \infty$

According to Fourier slice theorem in 2D, 1D Fourier transform of Radon transform of the function $\mu(\mathbf{x})$ along the line $\mathcal{L}(\hat{\boldsymbol{\theta}}, s)$ is the 1D "slice" of the function's 2D Fourier transform along the direction $\hat{\boldsymbol{\theta}}$ [56]:

$$\begin{aligned} \mathcal{F}_1 \mathcal{R}_2 \mu (\sigma; \hat{\boldsymbol{\theta}}) &= \mathcal{F}_2 \mu (\boldsymbol{\nu}) \Big|_{\boldsymbol{\nu}=\sigma \hat{\boldsymbol{\theta}}} \\ &= \mathcal{F}_2 \mu (\sigma \hat{\boldsymbol{\theta}}), \quad \text{see Appendix .3 for proof} \end{aligned} \quad (2.33)$$

3D Radon transform \mathcal{R}_3 of function $\mu(\mathbf{x})$, $\mathbf{x} \in \mathbb{R}^3$ is defined as a set of plane integrals. 2D plane in \mathbb{R}^3 is parameterized by the normal vector $\hat{\Theta}$ and the orthogonal distance t from the origin:

$$\Pi(\hat{\Theta}, t) = \left\{ \mathbf{x} \in \mathbb{R}^3 : \langle \mathbf{x}, \hat{\Theta} \rangle = t, \hat{\Theta} \in \mathbb{S}^2, t \in \mathbb{R} \right\} \quad (2.34)$$

3D Radon transform of the function $\mu(\mathbf{x})$, $\mathbf{x} \in \mathbb{R}^3$ is defined as [32] [95]:

$$\begin{aligned} \mathcal{R}_3\mu(\hat{\Theta}, t) &= \int_{\mathbf{x} \in \Pi(\hat{\Theta}, t)} \mu(\mathbf{x}) \, d\mathbf{x} \\ &= \int_{\mathbf{x} \in \mathbb{R}^3} \mu(\mathbf{x}) \delta(\langle \mathbf{x}, \hat{\Theta} \rangle - t) \, d\mathbf{x} \end{aligned} \quad (2.35)$$

Likewise, the generalized Radon transform \mathcal{R}_N in \mathbb{R}^N can be defined as the integral over $N - 1$ -dimensional hyperplanes [95].

2.4.2 X-ray Transforms

N -dimensional X-ray transform of a function $\mu(\mathbf{x})$, $\mathbf{x} \in \mathbb{R}^N$ is defined as the set of integrals along the lines diverging from a focal point \mathbf{f} . If the direction of the line is denoted by $\hat{\beta} \in \mathbb{S}^{N-1}$, X-ray transform can be expressed as:

$$\mathcal{X}_N(\mathbf{f}, \hat{\beta}) = \int_{l \in \mathbb{R}} \mu(\mathbf{f} + l\hat{\beta}) \, dl \quad (2.36)$$

Counter to the definition of Radon transform as the integral over hyperplanes, X-ray transform of a function is defined as a set of line integrals even for higher dimensions. In 2D, Radon and X-ray transforms are defined as line integrals and can be equated with a change of variables known as rebinning. X-ray transforms are also known as fan (2D), and cone beam transforms (3D).

2.5 Image Reconstruction in CT

Image reconstruction in CT is an inverse problem where the 3D spatial distribution of linear attenuation coefficients $\mu(\mathbf{x})$, $\mathbf{x} \in \mathbb{R}^3$ is estimated from its line integrals. CT reconstruction algorithms can be classified into four major categories [93]:

1. Analytical or transform-based reconstruction
2. Iterative reconstruction
3. Deep learning-based reconstruction

4. Hybrid reconstruction

Analytical reconstruction algorithms are the numerical methods for the exact or approximate inversion of Radon or X-ray transforms. In iterative reconstruction algorithms, the reconstructed image is optimized after a series of projection and back projection operations. The optimal image is computed by minimizing the difference between the measured projections and the forward projections of the current estimated image. Model-Based Iterative Reconstruction (MBIR) algorithms facilitate the incorporation of the models of X-ray generation, interaction with matter, detection, and acquisition geometry. Deep learning-based reconstruction is an ongoing research area where image reconstruction is performed using trained neural networks [91]. Analytical, iterative, and deep learning-based algorithms can be combined to formulate a hybrid reconstruction algorithm to exploit each of their advantages.

In this thesis, image reconstruction is performed using an analytical reconstruction algorithm known as Filtered Back Projection (FBP). It is the state-of-the-art reconstruction algorithm of major medical and industrial CT scanners. The prevalence of its adoption is mainly due to the computational efficiency and the linearity of the FBP operator. The emergence of the Fast Fourier Transform (FFT) algorithm and hardware like Digital Signal Processing (DSP) and Graphics Processing Unit (GPU)s enable FBP to perform ultra-fast volumetric reconstruction without requiring a large amount of memory. This is hugely beneficial when fast CT image acquisition is critical for patient safety. This section describes the FBP algorithm for 3D CBCT scanners that employ full or partial circular X-ray source trajectories (axial scans). Feldkamp, Davis, and Kress proposed the original reconstruction formula and is widely known as the FDK algorithm [36]. Since the algorithm is a heuristic extension of 2D fan beam FBP reconstruction, its description is preceded by the derivation of 2D parallel and fan beam reconstruction formulas.

The following assumptions are held for the description and the derivation of the algorithms:

1. The image to be reconstructed is assumed as continuous in their respective domains for the derivation of reconstruction formulas. Likewise, the projections (line integrals) are also continuous and are acquired with an infinite number of detector elements where the X-ray beam width is infinitesimally small.
2. The X-ray source is assumed to be punctiform by ignoring the fixed focal spot size.
3. The projections cover the entire FOV without any truncation.
4. The source-detector pair rotates around the object in a perfect full or partial circle.
5. The X-ray source is monochromatic, and the energy dependence of attenuation coefficient is omitted for brevity, $\mu(\mathbf{x}, E_m) = \mu(\mathbf{x}), \forall E_m$.

6. X-ray photons travel along straight lines without object or detector scatterings.
7. The imaged object is stationary during the scan.

The violation of these assumptions during the projection acquisition leads to various artifacts in the CT reconstructed images, and the artifacts need to be corrected before or after the FBP algorithm.

2.5.1 2D Parallel Beam Reconstruction

In 2D parallel beam projection geometry, X-ray photons are assumed to travel as parallel rays. It is analogous to the first-generation CT scanner's data collection, where the source-detector pair is translated to cover the FOV at each projection angle before rotation. Consider an arbitrary ray hits the detector element (bin) located s distance from the origin of WCS along the ray normal $\hat{\boldsymbol{\theta}}$. The total monochromatic attenuation values (Eq. 2.5) recorded by the detector elements can be considered the 2D Radon transform of the spatial distribution of linear attenuation coefficient $\mu(\mathbf{x})$, $\mathbf{x} \in \mathbb{R}^2$.

$$\begin{aligned}
 g_m(s, \hat{\boldsymbol{\theta}}) &= -\ln \left(\frac{I_t(s, \hat{\boldsymbol{\theta}})}{I_0(s, \hat{\boldsymbol{\theta}})} \right) \\
 &= \int_{l \in \mathbb{R}} \mu(s\hat{\boldsymbol{\theta}} + l\hat{\boldsymbol{\theta}}^\perp) dl \\
 &= \mathcal{R}_2\mu(s, \hat{\boldsymbol{\theta}})
 \end{aligned} \tag{2.37}$$

The mathematical equation for 2D parallel beam reconstruction is derived using the Fourier slice theorem (Eq. 2.33) [56] [48]. 2D inverse Fourier transform of $\mu(\mathbf{x})$ is given by:

$$\mu(\mathbf{x}) = \int_{\boldsymbol{\nu} \in \mathbb{R}^2} \mathcal{F}_2\mu(\boldsymbol{\nu}) e^{i2\pi\langle \mathbf{x}, \boldsymbol{\nu} \rangle} d\boldsymbol{\nu} \tag{2.38}$$

Using the Cartesian to polar coordinate transformation $\boldsymbol{\nu} = \sigma\hat{\boldsymbol{\theta}}$ where the Jacobian determinant $\det \mathbf{J} = |\sigma|$:

$$\mu(\mathbf{x}) = \frac{1}{2} \int_{\hat{\boldsymbol{\theta}} \in \mathbb{S}} \int_{\sigma \in \mathbb{R}} |\sigma| \mathcal{F}_2\mu(\sigma\hat{\boldsymbol{\theta}}) e^{i2\pi\langle \mathbf{x}, \sigma\hat{\boldsymbol{\theta}} \rangle} d\sigma d\hat{\boldsymbol{\theta}} \tag{2.39}$$

By applying the Fourier slice theorem (Eq. 2.33), we can replace the 2D Fourier transform of μ by the 1D Fourier transform of its 2D Radon transform:

$$\mu(\mathbf{x}) = \frac{1}{2} \int_{\hat{\boldsymbol{\theta}} \in \mathbb{S}} \int_{\sigma \in \mathbb{R}} |\sigma| \mathcal{F}_1\mathcal{R}_2\mu(\sigma; \hat{\boldsymbol{\theta}}) e^{i2\pi\sigma\langle \mathbf{x}, \hat{\boldsymbol{\theta}} \rangle} d\sigma d\hat{\boldsymbol{\theta}}, \tag{2.40}$$

where $\int_{\sigma \in \mathbb{R}} |\sigma| \mathcal{F}_1 \mathcal{R}_2(\sigma; \theta) e^{i2\pi\sigma \langle \mathbf{x}, \hat{\boldsymbol{\theta}} \rangle} d\sigma$ can be interpreted as the inverse Fourier transform after filtering in the frequency domain. The filter kernel in the continuous spatial domain is the 1D inverse Fourier transform of ramp function:

$$h_r(s) = \int_{\sigma \in \mathbb{R}} |\sigma| e^{i2\pi\sigma s} d\sigma \quad (2.41)$$

The following scaling property of ramp function is utilized for the derivation of reconstruction algorithms and the definition of consistency conditions:

$$h_r(cs) = \frac{1}{c^2} h_r(s), \quad \forall c \neq 0 \text{ see Appendix .4 for proof} \quad (2.42)$$

Since multiplication in the frequency domain is equivalent to the convolution operation $*$ in the spatial domain, Eq. 2.40 can be modified as:

$$\begin{aligned} \mu(\mathbf{x}) &= \frac{1}{2} \int_{\hat{\boldsymbol{\theta}} \in \mathbb{S}} h_r(s) * \mathcal{R}_2 \mu(s, \hat{\boldsymbol{\theta}}) \Big|_{s=\langle \mathbf{x}, \hat{\boldsymbol{\theta}} \rangle} d\hat{\boldsymbol{\theta}} \\ &= \frac{1}{2} \int_0^{2\pi} h_r(s) * \mathcal{R}_2 \mu(s, \theta) \Big|_{s=\langle \mathbf{x}, \hat{\boldsymbol{\theta}} \rangle} d\theta \\ &= \frac{1}{2} \int_0^{2\pi} \int_{s \in \mathbb{R}} h_r(\langle \mathbf{x}, \hat{\boldsymbol{\theta}} \rangle - s) \mathcal{R}_2 \mu(s, \theta) ds d\theta \end{aligned} \quad (2.43)$$

By exploiting the redundancy of 2D Radon transform (Eq. 2.30), the image can be reconstructed from the projections acquired over half scan where $\theta \in [0, \pi)$:

$$\mu(\mathbf{x}) = \int_0^\pi \int_{s \in \mathbb{R}} h_r(\langle \mathbf{x}, \hat{\boldsymbol{\theta}} \rangle - s) \mathcal{R}_2 \mu(s, \theta) ds d\theta \quad (2.44)$$

The individual steps of the 2D parallel beam reconstruction algorithm are summarized below:

1. Filtering: At first, the projections are filtered with a 1D ramp filter.

$$g_m^f(s; \hat{\boldsymbol{\theta}}) = h_r(s) * g_m(s; \hat{\boldsymbol{\theta}}) \quad (2.45)$$

Using the FFT algorithm, filtering operation can be efficiently implemented in the frequency domain by reducing the computational complexity from $\mathcal{O}(n^2)$ to $\mathcal{O}(n \log n)$.

2. Back projection: Filtered projections are back projected to object/image space where each point along the ray is assigned with the projection value recorded at the corresponding detector bin. Finally, all the back projected values are integrated to compute the reconstructed value at 3D point \mathbf{x} .

$$\mu(\mathbf{x}) = \int_{\theta}^{\pi} g_m^f(\langle \mathbf{x}, \hat{\boldsymbol{\theta}} \rangle, \theta) \, d\theta \quad (2.46)$$

Hence, the above-mentioned algorithm is aptly known as Filtered Back Projection (FBP). \mathcal{R}_2^{-1} denotes the FBP operator for 2D parallel beam reconstruction and is considered as the numerical method for the inversion of 2D Radon transform. The reconstruction of 2D image from the parallel projections using the FBP algorithm can be symbolically represented as $\mu(\mathbf{x}) = \mathcal{R}_2^{-1}g_m(\mathbf{x})$.

2.5.2 2D Fan Beam Reconstruction

In third-generation CT scanners, the projection data is acquired with a wide fan beam where the X-ray photons originating from the focal spot travel in different directions simultaneously to cover the FOV. As a result, the translation of source-detector pair employed in first (parallel beam) and second (narrow fan beam) generation CT scanners is eliminated to accelerate the projection acquisition. We assume that the X-ray photons are detected with a line detector. By limiting 3D cone beam geometry in the 2D rotation plane, we can use the same notations and the conventions as explained in the Sec. 2.3 to illustrate the geometry of 2D fan beam reconstruction as displayed in Fig. 2.6. $\mathbf{f}(\alpha) \in \mathbb{R}^2$ denotes the source position parameterized by the rotation angle α . The direction of the X-ray emanating from the source is denoted by $\hat{\boldsymbol{\beta}} \in \mathbb{S}$. Each ray in the 2D plane can also be identified with the fan angle β , the angle between the ray and the orthogonal vector from the source to the line detector (principal ray). The orthogonal ray meets the detector at point $\mathbf{d}(\alpha)$, the origin of the 1D Detector Coordinate System (DCS). Each ray intersects the detector at u , the signed distance from $\mathbf{d}(\alpha)$. D and R_f are the source-detector and source-isocenter distances. Similar to Eq. 2.37, the forward model of 2D fan beam reconstruction can be expressed as:

$$\begin{aligned} g_m(u, \alpha) &= g_m(\hat{\boldsymbol{\beta}}, \mathbf{f}(\alpha)) \\ &= -\ln \left(\frac{I_t(\hat{\boldsymbol{\beta}}, \mathbf{f}(\alpha))}{I_0(\hat{\boldsymbol{\beta}}, \mathbf{f}(\alpha))} \right) \\ &= \int_{l \in \mathbb{R}} \mu(\mathbf{f}(\alpha) + l\hat{\boldsymbol{\beta}}) \, dl \\ &= \mathcal{X}_2\mu(\hat{\boldsymbol{\beta}}, \mathbf{f}(\alpha)) \end{aligned} \quad (2.47)$$

$$\begin{aligned}
 s &= R_f \sin \beta \\
 &= R_f \frac{u}{\sqrt{u^2 + D^2}}
 \end{aligned} \tag{2.51}$$

The Jacobian determinant associated with the coordinate transformation is:

$$\det \mathbf{J} = \frac{R_f D^2}{(u^2 + D^2)^{\frac{3}{2}}} \tag{2.52}$$

The normal vector $\hat{\boldsymbol{\theta}}$ to any source-detector line can be obtained after 90-degree anti-clockwise rotation (Fig. 2.5):

$$\hat{\boldsymbol{\theta}} = \frac{D \hat{\mathbf{u}}(\alpha) - u \hat{\mathbf{w}}(\alpha)}{\sqrt{u^2 + D^2}} \tag{2.53}$$

2D fan beam reconstruction formula can be derived from its counterpart in 2D parallel beam geometry by substituting the rebinning equations [56]. The term $h_r(\langle \mathbf{x}, \hat{\boldsymbol{\theta}} \rangle - s)$ of Eq. 2.43 can be modified as:

$$\begin{aligned}
 h_r(\langle \mathbf{x}, \hat{\boldsymbol{\theta}} \rangle - s) &= h_r(\langle \mathbf{x}, \hat{\boldsymbol{\theta}} \rangle - \langle \mathbf{f}(\alpha), \hat{\boldsymbol{\theta}} \rangle) \text{ where } s = \langle \mathbf{f}(\alpha), \hat{\boldsymbol{\theta}} \rangle \text{ as per Fig. 2.6} \\
 &= h_r(\langle \mathbf{x} - \mathbf{f}(\alpha), \hat{\boldsymbol{\theta}} \rangle) \\
 &= h_r\left(\langle \|\mathbf{x} - \mathbf{f}(\alpha)\| \frac{\mathbf{x} - \mathbf{f}(\alpha)}{\|\mathbf{x} - \mathbf{f}(\alpha)\|}, \hat{\boldsymbol{\theta}} \rangle\right) \\
 &= h_r(\langle \|\mathbf{x} - \mathbf{f}(\alpha)\| \hat{\boldsymbol{\beta}}_{\mathbf{x}}, \hat{\boldsymbol{\theta}} \rangle) \text{ by substituting Eq. 2.48} \\
 &= \frac{1}{\|\mathbf{x} - \mathbf{f}(\alpha)\|^2} h_r(\langle \hat{\boldsymbol{\beta}}_{\mathbf{x}}, \hat{\boldsymbol{\theta}} \rangle) \text{ as per Eq. 2.42} \\
 &= \frac{1}{\|\mathbf{x} - \mathbf{f}(\alpha)\|^2} h_r\left(\frac{D(u_{\mathbf{x}} - u)}{\sqrt{u_{\mathbf{x}}^2 + D^2} \sqrt{u^2 + D^2}}\right) \\
 &= \frac{(u_{\mathbf{x}}^2 + D^2)(u^2 + D^2)}{\|\mathbf{x} - \mathbf{f}(\alpha)\|^2 D^2} h_r(u_{\mathbf{x}} - u)
 \end{aligned} \tag{2.54}$$

As per Fig. 2.6,

$$\cos \beta_{\mathbf{x}} = \frac{D}{\sqrt{u_{\mathbf{x}}^2 + D^2}} = \frac{\langle \mathbf{x} - \mathbf{f}(\alpha), \hat{\mathbf{w}}(\alpha) \rangle}{\|\mathbf{x} - \mathbf{f}(\alpha)\|} \tag{2.55}$$

By utilizing the above relation,

$$\begin{aligned}
 h_r(\langle \mathbf{x}, \hat{\boldsymbol{\theta}} \rangle - s) &= \frac{D^2 (u^2 + D^2)}{\langle \mathbf{x} - \mathbf{f}(\alpha), \hat{\mathbf{w}}(\alpha) \rangle^2 D^2} h_r(u_{\mathbf{x}} - u) \\
 &= \frac{(u^2 + D^2)}{\langle \mathbf{x} - \mathbf{f}(\alpha), \hat{\mathbf{w}}(\alpha) \rangle^2} h_r(u_{\mathbf{x}} - u)
 \end{aligned} \tag{2.56}$$

By substituting Eq. 2.56 along with the change of variables (Eq. 2.50, Eq. 2.51 and Eq. 2.52), Eq. 2.43 can be transformed to 2D fan beam reconstruction formula:

$$\begin{aligned}\mu(\mathbf{x}) &= \frac{1}{2} \int_0^{2\pi} \int_{u \in \mathbb{R}} \frac{(u^2 + D^2)}{\langle \mathbf{x} - \mathbf{f}(\alpha), \hat{\mathbf{w}}(\alpha) \rangle^2} h_r(u_{\mathbf{x}} - u) \mathcal{X}_2\mu(u, \alpha) \frac{R_f D^2}{(u^2 + D^2)^{\frac{3}{2}}} du d\alpha \\ &= \frac{1}{2} \int_0^{2\pi} \int_{u \in \mathbb{R}} \frac{DR_f}{\langle \mathbf{x} - \mathbf{f}(\alpha), \hat{\mathbf{w}}(\alpha) \rangle^2} h_r(u_{\mathbf{x}} - u) \frac{D}{\sqrt{u^2 + D^2}} \mathcal{X}_2\mu(u, \alpha) du d\alpha\end{aligned}\quad (2.57)$$

Short Scan Reconstruction

If the focal spot trajectory is a full circle (full scan), the lines passing through the imaged object intersect the source trajectory at two different points, and thereby each line integral is measured twice. Similar to Eq. 2.30, redundancy in 2D fan beam geometry is given by:

$$\mathcal{X}_2\mu(\beta, \alpha) = \mathcal{X}_2\mu(-\beta, \alpha + \pi - 2\beta) \quad (2.58)$$

where

$$\beta = \tan^{-1} \left(\frac{u}{D} \right) \quad (2.59)$$

By utilizing the redundancy property of 2D Radon transform, Eq. 2.44 showed that the half-circle source trajectory is sufficient for exact 2D parallel beam reconstruction. As per Tuy's sufficiency condition in 2D, any ray passing through the imaged object should be measured at least once [98]. The projections of half-circle trajectory are not adequate for the accurate 2D fan beam reconstruction due to the unmeasured line integrals. All the line integrals are measured at least once if the rotation angular range is $\pi + \beta_{det}$ where β_{det} is the total detector fan angle. Such CT projection data acquisition is named as short scan and is widely used in interventional CBCT imaging to reduce dose and acquisition time.

In short scans, the majority of the integrals are once, and some are measured twice. To avoid redundancy artifacts, the contribution of line integral measured twice should be equal to that of measured once during back projection. Hence, the line integrals need to be weighted before back projection. As per Eq. 2.58, the important property of redundancy weighting function is given by:

$$w_r(\beta, \alpha) + w_r(-\beta, \alpha + \pi - 2\beta) = 1 \quad (2.60)$$

The trivial function based on binary weights of 1 and 0.5 introduces artifacts in the reconstructed image after high pass ramp filtering. Therefore, Parker introduced

a smooth weighting function for the short scan [74] [45]:

$$w_r(\beta, \alpha) = \begin{cases} \sin^2\left(\frac{\pi(\alpha-\alpha_0)}{4\left(\frac{\beta_{det}}{2}-\beta\right)}\right), & \text{for } 0 \leq (\alpha - \alpha_0) \leq \beta_{det} - 2\beta \\ 1, & \text{for } \beta_{det} - 2\beta \leq (\alpha - \alpha_0) \leq \pi - 2\beta \\ \sin^2\left(\frac{\pi(\pi+\beta_{det}-(\alpha-\alpha_0))}{4\left(\frac{\beta_{det}}{2}+\beta\right)}\right), & \text{for } \pi - 2\beta \leq (\alpha - \alpha_0) \leq \pi + \beta_{det} \end{cases} \quad (2.61)$$

where α_0 is the initial rotation angle. For a full scan where all the line integrals are measured twice, the weighting function is a constant scaling factor.

$$w_r(\beta, \alpha) = 0.5 \quad (2.62)$$

By modifying Eq. 2.57, the generalized full and short scan reconstruction formula for 2D fan beam geometry can be formulated:

$$\mu(\mathbf{x}) = \int_{\alpha_0}^{\alpha_{N_\alpha-1}} \int_{u \in \mathbb{R}} \frac{DR_f}{\langle \mathbf{x} - \mathbf{f}(\alpha), \hat{\mathbf{w}}(\alpha) \rangle^2} h_r(u_{\mathbf{x}} - u) w_r(u, \alpha) \frac{D}{\sqrt{u^2 + D^2}} \mathcal{X}_2 \mu(u, \alpha) du d\alpha \quad (2.63)$$

where $\alpha_{N_\alpha-1}$ is the rotation angle of the final projection.

2.5.3 3D CBCT Reconstruction

In CBCT axial scans, 3D volume $\mu(\mathbf{x})$, $\mathbf{x} \in \mathbb{R}^3$ is reconstructed from cone beam projections where the focal spot trajectory is a full or partial circle. The acquired projections are the line integrals (3D X-ray transform, \mathcal{X}_3) measured on a 2D detector plane. Since each cone beam projection contains the line integrals through the whole volume or the desired Region of Interest (ROI), real-time multi-slice reconstruction can be performed without translating the patient or source-detector assembly. As per the CBCT geometry described in Sec. 2.3, the cone beam projection generation is modeled as:

$$\begin{aligned} g_m(u, v, \alpha) &= g_m(\hat{\beta}, \mathbf{f}(\alpha)), \quad \hat{\beta} \in \mathbb{S}^2, \mathbf{f}(\alpha) \in \mathbb{R}^3 \\ &= -\ln\left(\frac{I_t(\hat{\beta}, \mathbf{f}(\alpha))}{I_0(\hat{\beta}, \mathbf{f}(\alpha))}\right) \\ &= \int_{l \in \mathbb{R}} \mu(\mathbf{f}(\alpha) + l\hat{\beta}) dl \\ &= \mathcal{X}_3 \mu(\hat{\beta}, \mathbf{f}(\alpha)) \end{aligned} \quad (2.64)$$

$[u, v]^T$ is the point on the detector where the X-ray of direction $\hat{\beta}$ hits:

$$\begin{aligned} u &= D \frac{\langle \hat{\beta}, \hat{u}(\alpha) \rangle}{\langle \hat{\beta}, \hat{w}(\alpha) \rangle} \\ v &= D \frac{\langle \hat{\beta}, \hat{v}(\alpha) \rangle}{\langle \hat{\beta}, \hat{w}(\alpha) \rangle} \end{aligned} \quad (2.65)$$

2D Radon and X-ray transforms are defined as line integrals, and the FBP algorithm in 2D is the inversion of Radon transform. In 3D, Radon and X-ray transforms are defined as plane and line integrals. Without an explicit formula to relate 3D Radon and X-ray transforms, Feldkamp, Davis, and Kress proposed the FDK reconstruction algorithm for the approximate inversion of 3D X-ray transform [36]. The algorithm is formulated by the heuristic extension of the 2D fan beam reconstruction formula. 3D FDK and 2D fan beam reconstructions are identical in the rotation plane. Therefore, an exact 3D reconstruction of the central slice is feasible with the FDK algorithm. According to Tuy's data sufficiency condition in 3D, an exact reconstruction is only possible if 3D Radon transform is available for all the planes intersecting the imaged object. It can be easily visualized that any plane parallel to the rotation plane does not intersect the CBCT axial scan's source trajectory. As a result, the approximate FDK reconstruction introduces artifacts in the slices distant from the rotation plane, and the artifacts are known as cone beam or Feldkamp artifacts.

The individual steps of FBP reconstruction using the FDK algorithm are [45]:

1. Cosine weighting: Each integral is weighted with the cosine of the angle between the X-ray and the principal ray.

$$g_m^c(u, v, \alpha) = \frac{D}{\sqrt{u^2 + v^2 + D^2}} g_m(u, v, \alpha) \quad (2.66)$$

2. Redundancy weighting: Row-wise redundancy weighting of the cosine weighted projections can be expressed as:

$$g_m^{cr}(u, v, \alpha) = w_r(u, \alpha) g_m^c(u, v, \alpha) \quad (2.67)$$

The redundancy weighting functions $w_r(u, \alpha)$ for full and short scans are given by Eq. 2.62 and Eq. 2.61

3. Filtering: Row-wise ramp filtering of the weighted projections in the spatial or frequency domain.

$$g_m^{crf}(u, v, \alpha) = h_r(u) * g_m^{cr}(u, v, \alpha) \quad (2.68)$$

4. Cone beam back projection: The linear attenuation coefficient at 3D point \mathbf{x} is computed by the cone beam back projection of filtered projection value at

$[u_{\mathbf{x}}, v_{\mathbf{x}}]^T$, the point where the X-ray coming from the source located at $\mathbf{f}(\alpha)$ and passes through \mathbf{x} hits the detector.

$$\mu(\mathbf{x}) = \int_{\alpha_0}^{\alpha_{N_\alpha-1}} \frac{DR_f}{\langle \mathbf{x} - \mathbf{f}(\alpha), \hat{\mathbf{w}}(\alpha) \rangle^2} g_m^{crf}(u_{\mathbf{x}}, v_{\mathbf{x}}, \alpha) d\alpha \quad (2.69)$$

$u_{\mathbf{x}}$ and $v_{\mathbf{x}}$ can be computed using Eq. 2.21.

3D CBCT axial reconstruction using FDK operator \mathcal{X}_3^{-1} is symbolically represented as:

$$\mu(\mathbf{x}) = \mathcal{X}_3^{-1} g_m(\mathbf{x}) \quad (2.70)$$

By contrast, the computation of total attenuation values from the reconstructed volume using cone beam transform \mathcal{X}_3 is known as forward projection.

$$g_m(u, v, \alpha) = \mathcal{X}_3 \mu(u, v, \alpha) \quad (2.71)$$

2.6 Cone Beam Data Consistency Conditions

In CT, the redundancy of over-determined and error-free projection measurements (Radon or X-ray transforms) can be mathematically expressed as a set of equivalence relations, known as Data Consistency Conditions (DCC). As explained in the previous section, the full scan projection dataset is over-determined in 2D parallel and fan beam geometries. Hence, Eq. 2.29 and Eq. 2.58 can be considered as the DCC caused by the redundant measurements. The exploration of symmetry in integral geometry has led to the discovery of several consistency conditions. For 2D and 3D parallel beam projections, Helgason-Ludwig Consistency Conditions (HLCC) are necessary and sufficient to characterize the projection data (2D or 3D Radon transforms) [64]. According to zeroth-order HLCC in 2D, the integral of 2D Radon transform over s gives 2D plane integral (3D Radon transform) independent of the rotation angle θ :

$$\int_{s \in \mathbb{R}} \mathcal{R}_2 \mu(s, \theta) ds = \mathcal{R}_3 \mu(\hat{\Theta}, t), \quad \text{see Appendix .5 for proof} \quad (2.72)$$

HLCC can be reformulated for 2D fan beam projections after rebinning using Eq. 2.50, Eq. 2.51 and Eq. 2.52.

$$\int_{u \in \mathbb{R}} \mathcal{X}_2 \mu\left(u, \alpha + \frac{\pi}{2} - \tan^{-1}\left(\frac{u}{D}\right)\right) \frac{D^2 R_f}{(u^2 + D^2)^{\frac{3}{2}}} du = \mathcal{R}_3 \mu(\hat{\Theta}, t) \quad (2.73)$$

For a 3D CBCT system with a perfect circular trajectory, HLCC is valid for 2D fan beam projection associated with the rotation or source trajectory plane.

In this thesis, we focus on data consistency conditions applicable to cone beam projection pairs. The consistency conditions are derived from the works of Bruce Smith and Pierre Grangeat to develop the exact 3D cone beam reconstruction algorithms based on the inversion of 3D Radon transforms [39] [83]. Accurate 3D reconstruction is possible if 3D Radon transform data is available for all the planes intersecting the imaged object, $\mu(\mathbf{x})$, $\mathbf{x} \in \mathbb{R}^3$. By employing the Fourier slice theorem in 3D, the inversion of 3D Radon transform (3D FBP) can be expressed as [32]:

$$\mu(\mathbf{x}) = \frac{1}{2} \int_{\mathbb{S}^2} \int_{\mathbb{R}} |\sigma| |\sigma| \mathcal{F}_1 \mathcal{R}_3 \mu(\hat{\Theta}, \sigma) e^{i2\pi\sigma\langle\mathbf{x}, \hat{\Theta}\rangle} d\sigma d\hat{\Theta} \quad (2.74)$$

Hence, the image can be reconstructed by 3D back projection of Radon transforms after filtering twice with the ramp filter along the radial direction. The second derivative of 3D Radon transform in the Fourier domain is given by [59]:

$$\mathcal{F}_1 \frac{\partial^2 \mathcal{R}_3 \mu(\hat{\Theta}, t)}{\partial t^2} = -(2\pi\sigma)^2 \mathcal{F}_1 \mathcal{R}_3 \mu(\hat{\Theta}, \sigma) \quad (2.75)$$

By substituting Eq. 2.75 in Eq. 2.74, the inversion of 3D Radon transform can be reformulated as [32]:

$$\mu(\mathbf{x}) = \frac{-1}{8\pi^2} \int_{\hat{\Theta} \in \mathbb{S}^2} \frac{\partial^2}{\partial t^2} \mathcal{R}_3 \mu(\hat{\Theta}, t) \Big|_{\langle\mathbf{x}, \hat{\Theta}\rangle=t} d\hat{\Theta} \quad (2.76)$$

Hence, the exact reconstruction is possible if 3D Radon transform data is available for all the planes intersecting the small spherical neighborhood of point \mathbf{x} . As a result, the requirement for 3D Radon transform for all the planes intersecting the imaged object is eliminated by replacing the global ramp filtering with the local derivative operation.

If the projections are acquired with a flat detector and 3D parallel beam X-rays, any plane integral can be directly computed from the projections itself by integrating the attenuation values along the line formed by the intersection of the plane and the detector (HLCC in 3D). This is not possible for cone beam projections due to the divergence of X-rays where the rays are condensed near the source, and the ray density decreases as the distance from the source increases. This will introduce a distance-dependent weighting factor while computing the integral. Instead of estimating 3D Radon transform directly, Smith and Grangeat's works focus on the computation of intermediate functions from the cone beam projection data. Smith and Grangeat intermediate functions are the ramp and first derivative filtered 3D Radon transforms along the radial directions. The necessary data for 3D reconstruction can be obtained from the intermediate functions by the subsequent ramp filtering and derivative operations. In this thesis, the consistency conditions derived from the

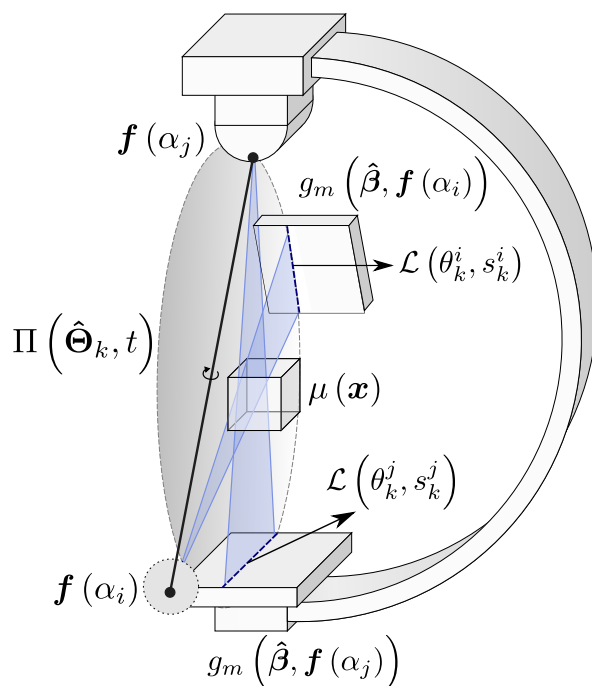


Figure 2.7: The geometry of pair-wise cone beam consistency conditions. The cone beam projections $g_m(\hat{\beta}, f(\alpha_i))$ and $g_m(\hat{\beta}, f(\alpha_j))$ are generated by the X-ray sources situated at $f(\alpha_i)$ and $f(\alpha_j)$. The plane $\Pi(\hat{\Theta}_k, t)$ contains the line $f(\alpha_i) - f(\alpha_j)$ and slices the 3D volume $\mu(\mathbf{x})$. $\mathcal{L}(\theta_k^i, s_k^i)$ and $\mathcal{L}(\theta_k^j, s_k^j)$ represent the lines formed by the intersection of $\Pi(\hat{\Theta}_k, t)$ and the detector planes. Reprinted from Abdurahman et al. [13] with permission from IEEE. ©IEEE 2018.

respective intermediate functions are aptly named Grangeat (GCC) and Smith Consistency Conditions (SCC). We also discuss the pair-wise formulation of Fan Beam Consistency Condition (FBCC), an extension of fan beam consistency condition for cone beam projections.

The pair-wise conditions are free from the limitations of having a perfect circular source trajectory and applicable for 3D CBCT systems with irregular or wobbling source trajectories found in interventional or mobile C-arm CT. As in all the formulations of DCC, we assume that cone beam projections are not truncated. Unlike HLCC for parallel beam projections, all the pair-wise consistency conditions mentioned in this thesis are necessary but not sufficient to fully characterize cone beam projection data.

Fig. 2.7 displays the geometry of pair-wise consistency conditions. $g_m(\beta, f(\alpha_i))$ and $g_m(\beta, f(\alpha_j))$ are cone beam projections where the X-ray sources are located at $f(\alpha_i)$ and $f(\alpha_j)$. α_i and α_j are the rotation angles corresponding to the projection indices i and j where $i, j \in \{0, 1, \dots, N_\alpha - 1\}$ (Eq. 2.15). The line connecting two

source positions is given by $\mathbf{f}(\alpha_i) - \mathbf{f}(\alpha_j)$ and is termed as the baseline. We can find a set of planes $\Pi(\hat{\Theta}_k, t)$ (Eq. 2.34) containing the baseline. The planes slice the volume $\mu(\mathbf{x})$, $\mathbf{x} \in \mathbb{R}^3$ and intersect the detectors. $\mathcal{L}(\theta_k^i, s_k^i)$ and $\mathcal{L}(\theta_k^j, s_k^j)$ denote the intersection lines. θ_k^i and s_k^i are the 2D Radon coordinates in Detector Coordinate System (DCS) spanned by the basis vectors $\hat{\mathbf{u}}(\alpha_i)$ and $\hat{\mathbf{v}}(\alpha_i)$. θ_k^i is the angle between the line normal vector and $\hat{\mathbf{u}}(\alpha_i)$. s_k^i is the orthogonal distance from the origin of DCS to the line (Fig. 2.5). D^i and D^j denote the source-detector distances, considering the irregular source trajectory. $-\hat{\mathbf{w}}(\alpha_i)$ and $-\hat{\mathbf{w}}(\alpha_j)$ are the normal vectors to the detector planes.

2.6.1 Grangeat Consistency Conditions

Consider the 2D X-ray fan beam marked by the transparent blue triangle in Fig. 2.7. $\beta \in \mathbb{R}$ and $r \in \mathbb{R}$ represent the polar angle and the radial distance from the point $\mathbf{f}(\alpha_i)$, the origin of the 2D polar coordinate system. 2D plane integral or 3D Radon transform can be expressed in polar coordinates:

$$\mathcal{R}_3\mu(\hat{\Theta}_k, t) = \int_0^\pi \int_{r \in \mathbb{R}} \mu(r, \beta) r dr d\beta \quad (2.77)$$

The integral of total attenuation values along the line $\mathcal{L}(\theta_k^i, s_k^i)$ gives the 2D plane integral of the function $\mu(r, \beta)$ after weighting with the inverse of radial distance [98] [46].

$$\int_{\hat{\beta} \in \mathbb{S}^2} \delta(\langle \hat{\Theta}_k, \hat{\beta} \rangle) g_m(\hat{\beta}, \mathbf{f}(\alpha_i)) d\hat{\beta} = \int_0^\pi \int_{r \in \mathbb{R}} \frac{1}{r} \mu(r, \beta) r dr d\beta \quad (2.78)$$

If κ is the angle between $\hat{\Theta}_k$ and the normal vector of the plane orthogonal to the detector (slice angle), the angular and tangential (radial) derivative of the planes are related by [98] [46]:

$$\frac{\partial}{\partial \kappa} = r \frac{\partial}{\partial t} \quad (2.79)$$

Using "Grangeat's trick", the radial and first derivative of the 3D Radon transform can be computed by the angular derivative of the weighted plane integral [98] [46].

$$\begin{aligned} \int_0^\pi \int_{r \in \mathbb{R}} \frac{\partial}{\partial \kappa} \frac{1}{r} \mu(r, \beta) r dr d\beta &= \int_0^\pi \int_{r \in \mathbb{R}} \frac{\partial}{\partial t} \mu(r, \beta) r dr d\beta \\ &= \frac{\partial}{\partial t} \mathcal{R}_3\mu(\hat{\Theta}_k, t) \end{aligned} \quad (2.80)$$

Therefore, a relation can be established between 3D Radon transform and artifact-free cone beam projection via an intermediate function G , the first derivative of 3D Radon transform. The relation was proposed by Pierre Grangeat and is known as Grangeat's fundamental relation [39] [31] [37]:

$$\begin{aligned} G^i(\hat{\Theta}_k) &= - \int_{\hat{\beta} \in \mathbb{S}^2} \delta'(\langle \hat{\Theta}_k, \hat{\beta} \rangle) g_m(\hat{\beta}, \mathbf{f}(\alpha_i)) d\hat{\beta} \\ &= \frac{\partial}{\partial t} \mathcal{R}_3 \mu(\hat{\Theta}_k, t) \Big|_{t=\langle \mathbf{f}(\alpha_i), \hat{\Theta}_k \rangle} \end{aligned} \quad (2.81)$$

where δ' is the distributional derivative of Dirac delta function:

$$- \int \delta'(x) f(x) dx = \int \delta(x) f'(x) dx \quad (2.82)$$

The proof of Grangeat's fundamental relation is given in Appendix .6.

As described in [31], the intermediate function can be computed from the cosine weighted projection g_m^c (Eq. 2.66) by calculating the 2D Radon transform and the derivative orthogonal to the line:

$$\begin{aligned} G^i(\hat{\Theta}_k) &= G(\theta_k^i, s_k^i) \\ &= \frac{(s_k^i)^2 + (D^i)^2}{(D^i)^2} \frac{\partial}{\partial s_k^i} \mathcal{R}_2 g_m^c(\theta_k^i, s_k^i) \quad \text{see Appendix .7 for proof} \end{aligned} \quad (2.83)$$

Since both source points lie in the same plane, the same value of the intermediate function can be computed from the projection pair, and the consistency condition associated with the plane is given by $G^i(\hat{\Theta}_k) = G^j(\hat{\Theta}_k)$. By considering K number of sampled planes around the baseline $\mathbf{f}(\alpha_i) - \mathbf{f}(\alpha_j)$, Grangeat Consistency Conditions (GCC) can be mathematically expressed as:

$$G^i(\hat{\Theta}_k) = G^j(\hat{\Theta}_k), \quad \forall k \in \{0, \dots, K-1\} \quad (2.84)$$

2.6.2 Smith Consistency Conditions

The relation between 3D Radon transform and cone beam projection can also be established using Smith intermediate function, the ramp filtered 3D Radon transform [83].

$$\begin{aligned} S^i(\hat{\Theta}_k) &= \int_{\hat{\beta} \in \mathbb{S}^2} h_r(\langle \hat{\Theta}_k, \hat{\beta} \rangle) g_m(\hat{\beta}, \mathbf{f}(\alpha_i)) d\hat{\beta} \\ &= h_r(t) * \mathcal{R}_3 \mu(\hat{\Theta}_k, t) \Big|_{t=\langle \mathbf{f}(\alpha_i), \hat{\Theta}_k \rangle} \quad \text{see Appendix .8 for proof} \end{aligned} \quad (2.85)$$

As like Eq. 2.83, Smith intermediate function can be computed from the flat panel detector projections:

$$\begin{aligned} S^i(\hat{\Theta}_k) &= S(\theta_k^i, s_k^i) \\ &= \frac{(s_k^i)^2 + (D^i)^2}{(D^i)^2} h_r(s_k^i) * \mathcal{R}_2 g_m^c(\theta_k^i, s_k^i) \end{aligned} \quad (2.86)$$

By following the same reasoning employed to define GCC, Smith Consistency Conditions (SCC) are given by:

$$S^i(\hat{\Theta}_k) = S^j(\hat{\Theta}_k), \quad \forall k \in \{0, \dots, K-1\} \quad (2.87)$$

2.6.3 Fan Beam Consistency Conditions

Consider the source-detector assembly travels along a straight line and acquires 2D fan beam projections $g_m(\hat{\beta}, \mathbf{f}(\alpha^d))$, $\hat{\beta} \in \mathbb{S}$. The source position is denoted by $\mathbf{f}(\alpha^d)$ where α^d is the distance parameter along the linear source trajectory. ϕ is the angle between the normal to the source trajectory and the ray $\hat{\beta}$. Clackdoyle developed a necessary and sufficient n th-order condition for 2D fan beam projections (FBCC) acquired over the line trajectory [28]. As per the zeroth-order formulation of FBCC, the weighted sum of projections is invariant irrespective of the source position.

$$F(d) = \int_{-\frac{\pi}{2}}^{\frac{\pi}{2}} \frac{g(\hat{\beta}, \mathbf{f}(\alpha^d))}{\cos \phi} d\phi = F \quad (2.88)$$

We refer to F as the fan beam "intermediate" function for uniformity. The proof of the above equation can be found in [28].

FBCC can also be applied for a pair of cone beam projections as described in [60]. The projection values along the intersected lines $\mathcal{L}(\theta_k^i, s_k^i)$ and $\mathcal{L}(\theta_k^j, s_k^j)$ can be mapped onto a 1D virtual linear detector with the resampling equations given in [60]. The baseline between two source positions lies parallel to the 1D virtual detector. Hence, Eq. 2.88 is valid for a pair of resampled fan beam projections acquired with a linear source trajectory. In addition, many 1D virtual detectors parallel to the baseline and the associated fan beam projection pairs can be found by considering the planes containing baseline and intersecting the detectors as in GCC and SCC. Thus, pair-wise FBCC applicable to cone beam projections can be expressed as:

$$F^i(\hat{\Theta}_k) = F^j(\hat{\Theta}_k), \quad \forall k \in \{0, \dots, K-1\} \quad (2.89)$$

Without resampling, the fan beam intermediate function can be directly estimated from the cone beam projections by computing the line integral over the intersected

line after cosine and distance weighting [20] [59]:

$$\begin{aligned} F^i(\hat{\Theta}_k) &= F(\theta_k^i, s_k^i) \\ &= \frac{-1}{\langle \hat{\mathbf{w}}(\alpha_i), \frac{\mathbf{f}(\alpha_i) - \mathbf{f}(\alpha_j)}{\|\mathbf{f}(\alpha_i) - \mathbf{f}(\alpha_j)\|_2} \rangle} \mathcal{R}_2 g_m^{c,d}(\theta_k^i, s_k^i) \end{aligned} \quad (2.90)$$

$$\begin{aligned} F^j(\hat{\Theta}_k) &= F(\theta_k^j, s_k^j) \\ &= \frac{-1}{\langle \hat{\mathbf{w}}(\alpha_j), \frac{\mathbf{f}(\alpha_j) - \mathbf{f}(\alpha_i)}{\|\mathbf{f}(\alpha_i) - \mathbf{f}(\alpha_j)\|_2} \rangle} \mathcal{R}_2 g_m^{c,d}(\theta_k^j, s_k^j) \end{aligned} \quad (2.91)$$

where the distance weighting of projections is given by:

$$g_m^{c,d}(u, v, \alpha_i) = \frac{g_m^c(u, v, \alpha_i)}{\sqrt{(u - u_{e^{ij}})^2 + (v - v_{e^{ij}})^2}} \quad (2.92)$$

The distance is measured between the detector element location and the meeting point of all the intersected lines on the detector, known as the epipole. $[u_{e^{ij}}, v_{e^{ij}}]^T$ denotes the coordinates of the epipole in DCS and its counterpart in PCS $[u_{e^{ij}}^{pcs}, v_{e^{ij}}^{pcs}]^T$ is the projected pixel location of the source position $\mathbf{f}(\alpha_j)$:

$$\begin{aligned} u_{e^{ij}}^{pcs} &= \frac{\langle \mathbf{p}_0^T(\alpha_i), \tilde{\mathbf{f}}(\alpha_j) \rangle}{\langle \mathbf{p}_2^T(\alpha_i), \tilde{\mathbf{f}}(\alpha_j) \rangle} \\ v_{e^{ij}}^{pcs} &= \frac{\langle \mathbf{p}_1^T(\alpha_i), \tilde{\mathbf{f}}(\alpha_j) \rangle}{\langle \mathbf{p}_3^T(\alpha_i), \tilde{\mathbf{f}}(\alpha_j) \rangle} \end{aligned} \quad (2.93)$$

$\tilde{\mathbf{f}}(\alpha_j)$ is the source position in homogeneous coordinates. $\mathbf{p}_m^T(\alpha_i)$ is the $m+1$ -th row of the projection matrix $\mathbf{P}(\alpha_i)$. Similarly, the location of epipole $[u_{e^{ij}}^{pcs}, v_{e^{ij}}^{pcs}]^T$ is calculated by projecting the source position $\mathbf{f}(\alpha_j)$ onto the detector plane with the projection matrix $\mathbf{P}(\alpha_j)$.

2.7 CT Artifacts

2.7.1 Beam Hardening

In CT reconstruction using FBP algorithms, it is assumed that the projections are acquired with a monochromatic X-ray source. For a homogeneous and mono-material object, the reconstructed image can be considered the uniform distribution of linear attenuation coefficient $\mu(E_m)$. There exists a linear relationship between the

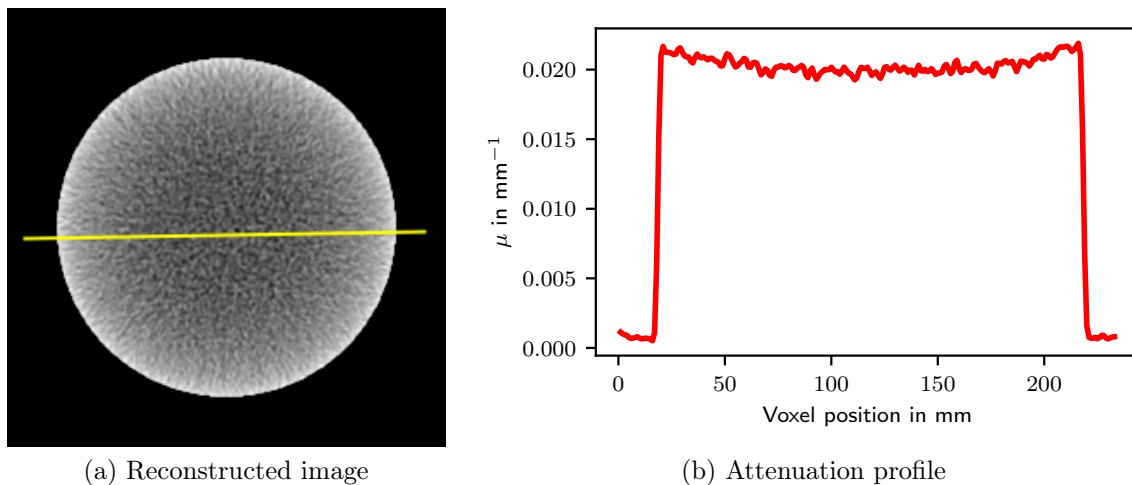


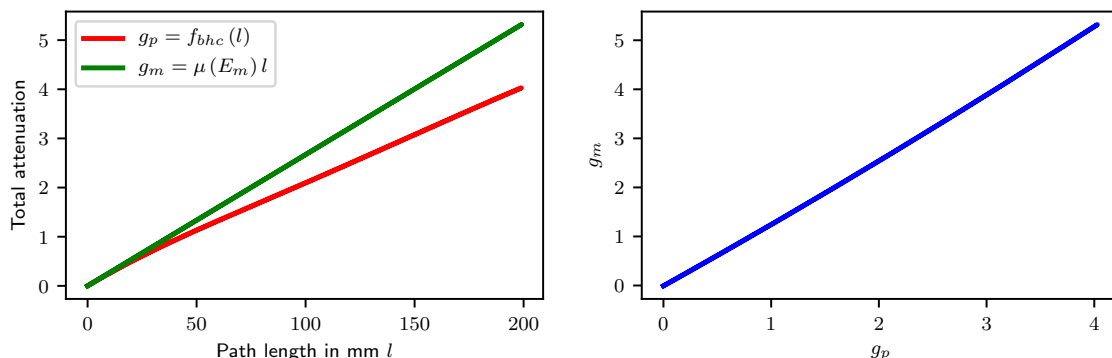
Figure 2.8: Cupping artifacts: (a) image reconstructed from the simulated polychromatic projections of the water phantom; (b) plot of attenuation values of the linear ROI segmented from the reconstructed image (marked by the yellow line).

monochromatic total attenuation g_m and the X-ray path length through the object l (length of the medium in Eq. 2.5) as displayed in Fig. 2.9a.

$$g_m = \mu(E_m)l \quad (2.94)$$

In practice, CT projections data is acquired with a polychromatic X-ray source violating the linear forward model due to the energy-dependent attenuation properties of the materials. During the transmission of polychromatic X-rays, the low-energy photons are preferentially attenuated (Fig. 2.1b). As a result, the mean energy of the X-ray spectrum increases, and it is referred to as the "hardening" of the X-ray beam [26]. The degree of attenuation decreases as the X-ray beam hardens. The relationship between the polychromatic total attenuation g_p and the path length through the volume is not linear (Eq. 2.10), as shown in Fig. 2.9a. The error due to the underestimation of total attenuation values is proportional to the path length. After reconstruction using linear FBP operation, the projection error is propagated to the volume as cupping artifacts (first-order beam hardening artifacts) where the linear attenuation coefficient values gradually decrease from the periphery to the interior of the object, as shown in Fig. 2.8a [55].

In clinical CBCT imaging, beam hardening artifacts hamper accurate clinical diagnosis and interventional procedures. Cupping artifacts degrade the low contrast detectability significantly in soft tissue imaging, where the artifacts are predominant due to low kVp. Selecting an optimal window level will be a tedious task to visualize low contrast structures if the cupping artifacts are present. Beam hardening artifacts also affect reliable quantitative evaluations and analysis based on CT images (e.g., attenuation correction in PET/CT) [53].



(a) The relation between the X-ray path length and the total attenuation, beam hardening curve (red) (b) Beam hardening correction polynomial

Figure 2.9: Beam hardening curve and polynomial.

One of the hardware methods to reduce beam hardening artifacts is to pre-harden the X-ray beam by strongly attenuating low-energy photons with the metal filters. In the past, water bags were also used to surround the patient body to achieve this goal [26]. Apart from their inability to remove the artifacts effectively, the pre-filtration of X-ray beams requires additional hardware. The reduced photon output after filtration degrades Signal-to-Noise Ratio (SNR) and necessitates a high dosage CT imaging. By incorporating the polychromatic forward projection models, the artifacts can be corrected by MBIR algorithms [34] [25]. The polychromatic iterative reconstructions are computationally expensive and require prior knowledge of X-ray and attenuation spectra.

Water Correction

The artifacts can be corrected by transforming the total attenuation values from polychromatic to monochromatic using a polynomial-based non-linear mapping [44]. Polynomial correction compensates the non-linear error due to the underestimation of total attenuation values, and the correction is known as projection linearization. In clinical imaging, the polynomials are pre-computed during the calibration of a CT scanner using water-filled cylindrical phantoms. The coverings of the phantom are made up of water-equivalent material like Plexiglas. Since the attenuation properties of water and the soft tissues are similar, beam hardening artifacts of clinical images can be mitigated using the polynomials computed during calibration. Hence, the projection linearization in clinical CT is referred to as water correction.

During calibration, the polychromatic projections of water phantoms are acquired, and the path lengths through the cylindrical volume are computed. The relationship between the path length and the polychromatic total attenuation value is modeled

with a higher-order polynomial function, as shown in Fig. 2.9a.

$$g_p = f_{bhc}(l) \quad (2.95)$$

The analytical expression of f_{bhc} is termed as beam hardening curve/function [90][68]. We can assume that the beam hardening effect is significantly low at the periphery of the cylinder. The linear attenuation coefficient of water when the path length is infinitesimally small is given by [40]:

$$\mu_{water} = \left. \frac{d}{dl} f_{bhc}(l) \right|_{l=0} \quad (2.96)$$

Considering $\mu_{water} = \mu(E_m)$, the values of virtual monochromatic projections can be calculated using Eq. 2.94. Finally, the mapping between polychromatic and monochromatic attenuation values (Fig. 2.9b) is found by polynomial regression.

The transformation of the total attenuation values from polychromatic g_p to virtual monochromatic g_w using a polynomial expression of degree N_w is considered as water correction. The volume free from the first-order beam hardening artifacts $\mu_w(\mathbf{x})$ can be reconstructed from g_w using the FDK algorithm.

Bone Correction

The attenuation properties of high-density and calcium-rich cortical bone differ from that of soft tissues (Fig. 2.1b). The beam hardening-induced projection error is contributed by the polychromatic X-ray transmission through soft tissues and bones. Therefore, water correction alone does not remove beam hardening artifacts from the clinical CT images. The residual error after water correction retains streak artifacts in the volume, which appear as dark bands between high attenuation bony structures. Due to the spill-over of bright pixels of bone to soft tissue regions, bone-induced artifacts also prevent sharp bone-tissue boundaries.

Joseph and Spital proposed a bi-pass correction algorithm for bone-induced artifacts [52]. First, a prior volume $\mu_w(\mathbf{x})$ is reconstructed from the water corrected projections. Subsequently, the bone structures $\mu_b(\mathbf{x})$ are segmented using a thresholding operation. Joseph and Spital theorized that the projection error after water correction $-\Delta g_w^b$ is proportional to the forward (or path length) projection values of segmented bone volume $\mathcal{X}_3\mu_b$ as per the quadratic model given below:

$$-\Delta g_w^b(u, v, \alpha) = A \mathcal{X}_3\mu_b(u, v, \alpha) + B [\mathcal{X}_3\mu_b(u, v, \alpha)]^2 \quad (2.97)$$

where A and B are free parameters. The streak artifacts are caused by the non-linear term of the projection error. The Joseph-Spital algorithm corrects bone-induced artifacts utilizing the forward projections of segmented bone and soft tissue volumes, mass attenuation spectra of bone and soft tissues, and a calibration-based estimation of scaling factors [88] [52].

Based on the works of Joseph-Spital, Hsieh et al. proposed an Iterative Beam Hardening Correction (IBHC) algorithm to reduce bone-induced artifacts [49]. The residual projection error (Eq. 2.97) is modeled with the water \mathbf{w} and bone correction polynomials \mathbf{b}^t of the same degree N_w . Since I_0 and I_t represent the incident and transmitted intensities, water correction can be expressed as:

$$g_{\mathbf{w}} = \sum_{c=1}^{N_w} w_c \left[\ln \left(\frac{I_0}{I_t} \right) \right]^c \quad (2.98)$$

In a sequential X-ray transmission through a volume containing water and bone, we can consider I_w as the intensity transmitted by the water volume and the incident intensity of the bone volume. The water and bone corrected projections can be expressed using \mathbf{w} and \mathbf{b}^t [49]:

$$g_{\mathbf{w}}^{\mathbf{b}^t} = \sum_{c=1}^{N_w} w_c \left[\ln \left(\frac{I_0}{I_w} \right) \right]^c + \sum_{c=1}^{N_w} b_c^t \left[\ln \left(\frac{I_w}{I_t} \right) \right]^c \quad (2.99)$$

The residual projection error after water correction caused by bone-induced beam hardening is quantified by:

$$\begin{aligned} -\Delta g_{\mathbf{w}}^{\mathbf{b}^t} &= g_{\mathbf{w}} - g_{\mathbf{w}}^{\mathbf{b}^t} \\ &= \sum_{c=1}^{N_w} w_c \left[\ln \left(\frac{I_0}{I_t} \right) \right]^c - \sum_{c=1}^{N_w} w_c \left[\ln \left(\frac{I_0}{I_w} \right) \right]^c - \sum_{c=1}^{N_w} b_c^t \left[\ln \left(\frac{I_w}{I_t} \right) \right]^c \\ &= \sum_{c=1}^{N_w} (w_c - b_c^t) \left[\ln \left(\frac{I_w}{I_t} \right) \right]^c + \epsilon \end{aligned} \quad (2.100)$$

\mathbf{b}^t denotes the vector containing IBHC correction coefficients. By approximating $\ln \left(\frac{I_w}{I_t} \right)$ with $\mathcal{X}_3\mu_b$ and ignoring higher-order terms, the above equation can be equated with Eq. 2.97 when $N_w = 2$. The water + bone corrected projections are computed by subtracting the residual error from the water corrected projections:

$$g_{\mathbf{w}}^{\mathbf{b}^t}(u, v, \alpha) = g_{\mathbf{w}}(u, v, \alpha) + \Delta g_{\mathbf{w}}^{\mathbf{b}^t}(u, v, \alpha) \quad (2.101)$$

$\Delta g_{\mathbf{w}}^{\mathbf{b}^t}$ can also be considered as the additive correction values to compensate for the underestimation errors due to bone beam hardening (Fig. 2.10a). The necessary IBHC coefficients can be estimated theoretically using prior knowledge or empirically by phantom experiments [49].

Kyriakou et al. proposed an Empirical Beam Hardening Correction (EBHC) algorithm where the bone corrected projections are modeled as a bivariate polynomial expression of water corrected and bone forward projections (Fig. 2.10b) [58]:

$$\begin{aligned} g_{\mathbf{w}}^{\mathbf{b}^e} &= g_{\mathbf{w}} + \Delta g_{\mathbf{w}}^{\mathbf{b}^e} \\ &= g_{\mathbf{w}} + b_0^e [\mathcal{X}_3\mu_b] + b_1^e [\mathcal{X}_3\mu_b]^2 + b_2^e [g_{\mathbf{w}}\mathcal{X}_3\mu_b] + \dots \end{aligned} \quad (2.102)$$

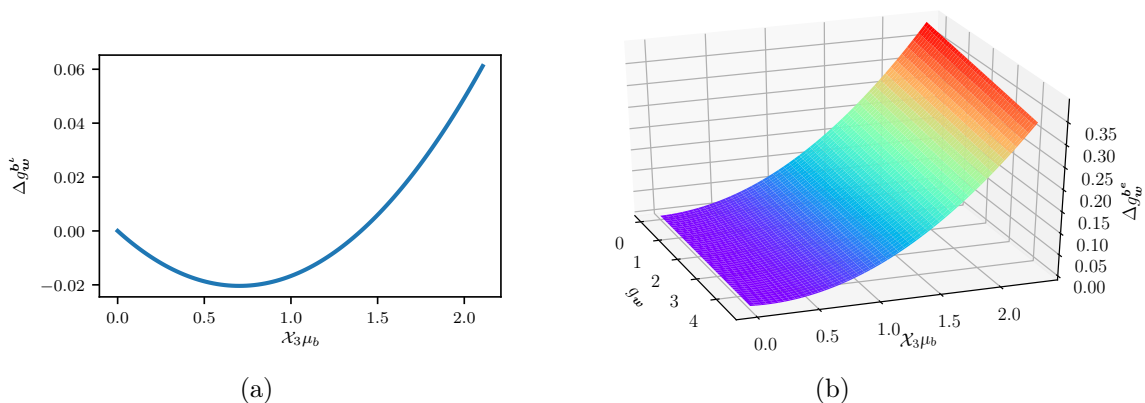


Figure 2.10: The values for bone-induced beam hardening correction in (a) IBHC; (b) EBHC.

The derivation of the above equation is described in [58]. Compared to the second-order IBHC where the uni-variate correction polynomial acts on bone forward projections, the EBHC model contains an additional coefficient to weight the product of water corrected and bone forward projections. Since FBP reconstruction using FDK algorithm is a linear operator (\mathcal{X}_3^{-1}), the bone corrected volume $\mu_w^{b^e}(\mathbf{x})$ parameterized by polynomial coefficients can be expressed as a linear combination of basis volumes $\mu_w(\mathbf{x})$, $\mu_b(\mathbf{x})$, $\mu_{bb}(\mathbf{x})$ and $\mu_{wb}(\mathbf{x})$ [58]:

$$\mu_w^{b^e}(\mathbf{x}) = \mu_w(\mathbf{x}) + b_0^e \mu_b(\mathbf{x}) + b_1^e \mu_{bb}(\mathbf{x}) + b_2^e \mu_{wb}(\mathbf{x}) \quad (2.103)$$

$$\begin{aligned} \mu_w(\mathbf{x}) &= \mathcal{X}_3^{-1}[g_w](\mathbf{x}) \\ \mu_{bb}(\mathbf{x}) &= \mathcal{X}_3^{-1}[\mathcal{X}_3\mu_b]^2(\mathbf{x}) \\ \mu_{wb}(\mathbf{x}) &= \mathcal{X}_3^{-1}[g_w \mathcal{X}_3\mu_b](\mathbf{x}) \end{aligned} \quad (2.104)$$

By minimizing the Total Variation (TV) of bone corrected volume, Kyriakou et al. estimated the optimal correction coefficients as given below [58]:

$$\min_{b^e} \int_{\mathbf{x} \in \mathbb{R}^3} \|\nabla \mu_w^{b^e}(\mathbf{x})\|_1 \, d\mathbf{x} \quad (2.105)$$

Park et al. proposed Beam Hardening Factor (BHF) to quantify the projection error due to beam hardening by high attenuation structures like metals or bones [72] [73]. BHF uses shape information of bones $\mathcal{X}_3 f_b$, the path length through the segmented bone volume. The volume of bone fraction f_b is given by:

$$f_b(\mathbf{x}) = \begin{cases} 1 & \mu_b(\mathbf{x}) > 0 \\ 0 & \mu_b(\mathbf{x}) \leq 0 \end{cases} \quad (2.106)$$

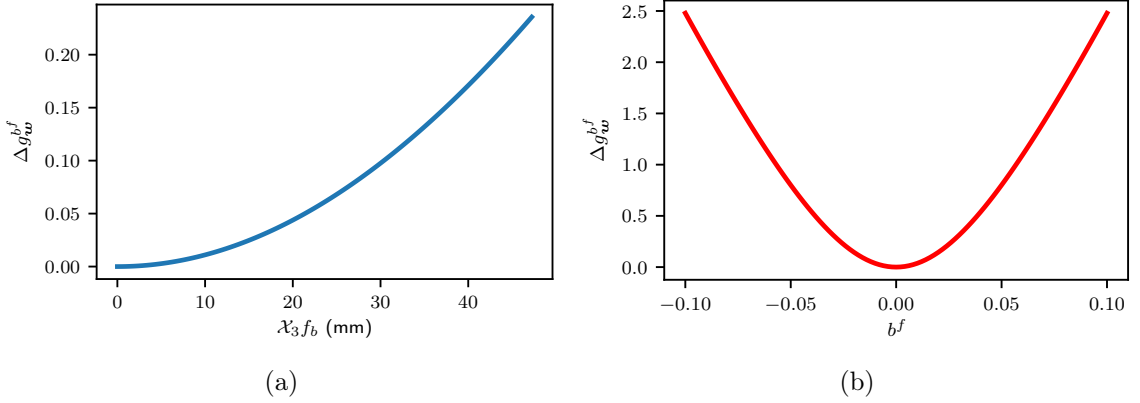


Figure 2.11: Beam hardening factor (Eq. 4.15) when (a) $b^f = 0.02575$; (b) $\mathcal{X}_3 f_b = 47.2446$.

BHF for bone correction can be expressed as (Fig.2.11):

$$\Delta g_{\mathbf{w}}^{b^f}(u, v, \alpha) = \begin{cases} 0 & b^f \mathcal{X}_3 f_b(u, v, \alpha) = 0 \\ \ln\left(\frac{\sinh(b^f \mathcal{X}_3 f_b(u, v, \alpha))}{b^f \mathcal{X}_3 f_b(u, v, \alpha)}\right) & b^f \mathcal{X}_3 f_b(u, v, \alpha) \neq 0 \end{cases} \quad (2.107)$$

The bone corrected projections are computed by adding BHF to the water corrected projections.

$$g_{\mathbf{w}}^{b^f}(u, v, \alpha) = g_{\mathbf{w}}(u, v, \alpha) + \Delta g_{\mathbf{w}}^{b^f}(u, v, \alpha) \quad (2.108)$$

Park et al. estimated the free parameter of BHF by solving the following optimization problem [72].

$$\min_{b^f} \int_{\mathbf{x} \in \mathbb{R}^3} \left[W(\mathbf{x}) \nabla \left(\mu_{\mathbf{w}}(\mathbf{x}) + \mathcal{X}_3^{-1} \Delta g_{\mathbf{w}}^{b^f}(\mathbf{x}) \right) \right]^2 d\mathbf{x} \quad (2.109)$$

The weighting function $W(\mathbf{x})$ was chosen to add more penalties on the high-frequency streak artifacts [72]. We refer to the above correction as Beam Hardening Factor-based Correction (BHFC).

All the correction methods mentioned in this section can also be used for the correction of artifacts caused by the beam hardening in metals or iodine. After water and bone corrections, metal/iodine volume is segmented, and the artifact-free projections/volume can be generated by employing IBHC, EBHC, or BHFC algorithms.

2.7.2 Scatter

Due to Rayleigh or Compton scatterings, X-rays deviate from their original linear propagation path, and the secondary scatter radiation is generated (Sec. 2.1.2). In

the forward model of cone beam reconstruction (Eq. 2.64), the secondary radiation is neglected, and the transmitted X-ray intensity I_t is considered as a measure of the number of photons of non-scattered primary radiation. The presence of secondary scatter radiation of intensity I_s increases the overall detected X-ray intensity to $I_t + I_s$. As a result, the total attenuation values are underestimated after I_0 normalization and log transformation. The total attenuation values of scatter-free g_m and scatter-corrupted g_m^s projections are related by the following equation:

$$g_m^s(u, v, \alpha) = g_m(u, v, \alpha) - \ln(1 + SPR(u, v, \alpha)), \text{ see Appendix .9 for proof} \quad (2.110)$$

where SPR is the scatter to primary ratio image.

$$SPR(u, v, \alpha) = \frac{I_s(u, v, \alpha)}{I_t(u, v, \alpha)} \quad (2.111)$$

The non-linear projection error will be transferred to the volume after reconstruction. As in beam hardening, scatter artifacts appear as cupping and streak artifacts and degrade the low contrast resolution.

The state-of-the-art methods to reduce the scatter artifacts can be classified into two categories [81]:

1. Scatter rejection techniques.
2. Scatter correction techniques.

Scatter rejection techniques are hardware methods that prevent secondary scatter radiations from contributing to the final detected X-ray intensity. Scatter rejection can be achieved with additional hardware like anti-scatter grids and collimators. In clinical Multi-Detector CT (MDCT), one-dimensional scatter grids are employed to minimize the artifacts by absorbing scattered radiation. In clinical CBCT systems where large flat panel detectors are used, 2D anti-scatter grids are not practical due to the decreased SNR and the resultant need for a higher radiation dose. Scatter rejection can also be achieved with techniques like Volume of Interest (VOI) imaging and air-gap [81]. In VOI imaging, the collimators limit the FOV to clinically relevant volume and reduce the scatter in the projection images. VOI imaging requires an additional low dose scan covering the full FOV for the truncation artifact reduction. Like in projection radiography and mammography, most clinical CBCT systems use the air-gap method to eliminate the secondary scatter radiation by keeping the largest feasible distance between the patient and the detector [81].

Software-based scatter correction methods are used in combination with scatter rejection methods like air gap to reduce the residual scatter artifacts. They are also used to replace 2D anti-scatter grids for dose reduction. A posteriori scatter correction methods rely on the computation of scatter contribution to the measured projections [70]. Estimated scatter images can be subtracted from the detected X-ray intensity,

and the artifact corrected volume can be reconstructed. Beam stop arrays can measure scatter images directly but with the disadvantages of excess patient dose and increased acquisition time due to additional scans [81]. The realistic scatter (single and multiple) estimates can be generated by Monte-Carlo (MC) probabilistic simulation of photon transport through the imaged object (scattering medium). In addition to the computationally intensive operations like ray tracing and MC computations, it also requires initial reconstruction and prior knowledge about material compositions and their atomic properties, X-ray spectrum, and detector efficiency [54].

Computationally efficient model-based scatter images can be approximated from the measured projections by Scatter Kernel Superposition (SKS) [70][87][23]. SKS methods are formulated with the assumption that scatter images are the blurred version of the primary images [24]. Hence, the scatter images for all views are computed by the 2D convolution of weighted projections with a scatter kernel. The kernel parameters for a specific imaged object and system geometry need to be pre-computed by MC-based pencil beam experiments [87]. Baer et al. proposed object/patient-specific scatter correction by calibrating the kernel parameters with an initial estimate of scatter images, computed from a coarse MC simulation [23]. Zhao et al. estimated the prior scatter images by subtracting the polychromatic forward projections of initial reconstructed volume from the measured projections and subsequently optimized patient-specific kernel parameters [99].

2.7.3 Metal Artifacts

Due to the prevalence of prosthetics and implants in the aging population, metal streak artifacts are common in CT images. The artifacts are caused by beam hardening, scatter, photon starvation, noise, partial volume, and exponential edge gradient effects [29]. Higher-order beam hardening and scatter correction methods reduce the metal artifacts. However, they cannot effectively remove the artifacts caused by the large metal implants. The state-of-the-art Metal Artifact Reduction (MAR) methods rely on identifying and removing the metal trace from the projections before reconstruction. The missing projection values are restored using the projection completion methods like linear interpolation [38]. Meyer et al. proposed the Normalized Metal Artifact Reduction (NMAR) method to avoid the loss of information around the metals and the introduction of artifacts due to interpolation [67]. In NMAR, the projection data is normalized with the forward projection of the initial reconstructed volume before interpolation. A survey of MAR algorithms can be found in [38].

3 First-order Beam Hardening Correction using Consistency Conditions

3.1 Introduction

As explained in the last chapter (Sec. 2.7.1), beam hardening artifacts due to polychromatic X-ray attenuation by soft tissues can be compensated by projection linearization using correction polynomials. The polynomials are pre-computed during the calibration of the scanner using homogeneous and mono-material phantoms. In clinical CBCT, the water phantoms are used for calibration, assuming the primary constituent material of the human body is water. As shown in Fig. 2.1b and explained in Sec. 2.1, the soft tissues and water exhibit comparable attenuation properties. The mapping of the total attenuation values of the projections from polychromatic g_p to virtual monochromatic g_w using a polynomial expression of degree N_w is referred to as water correction:

$$\begin{aligned} g_w(u, v, \alpha) &= p_w(g_p(u, v, \alpha)) \\ &= \sum_{c=0}^{N_w} w_c [g_p(u, v, \alpha)]^c \\ \mathbf{w} \in \mathbb{R}^{N_w+1} &= [w_0, w_1, w_2, \dots, w_{N_w}]^T \end{aligned} \tag{3.1}$$

We use vector notation of \mathbf{w} to represent all water correction polynomial coefficients. The constant term w_0 is zero due to the lack of attenuation during mono and polychromatic X-ray transmission through the air. Therefore, N_w can also be considered as the number of coefficients of water correction polynomial.

It is very demanding to pre-compute the polynomials for diverse X-ray spectra during calibrations. As a result, the operators of clinical CT scanners are restricted to use pre-selected combinations of kVp, filter material, and thickness. Since effective artifact reduction is only possible for the objects composed of water-equivalent materials, clinical CBCT scanners cannot image the objects of different material compositions. In most scanners, beam hardening correction is a part of the pre-processing steps of the reconstruction pipeline. It is preceded by the algorithms of gain, offset,

overexposure, lag, and scatter corrections [85] [84]. Any modification in the preceding steps will change the projections' total attenuation values, and the calibrations need to be repeated. Similarly, the replacement of the X-ray tube, filters, or detector also requires re-calibrations. When CBCT is used for industrial, scientific, and security applications, the material composition and the geometry of the imaged object and the optimal imaging parameters cannot be determined in advance. Therefore, a calibration-free, energy, geometry, and material-specific and computationally efficient beam hardening correction is a prerequisite to generate artifact-free images for the material characterization and real-time automated inspection. Since our primary focus is artifact reduction in clinical CBCT, we consider water correction as a synonym for beam hardening correction for the mono-material objects with a non-homogeneous density distribution.

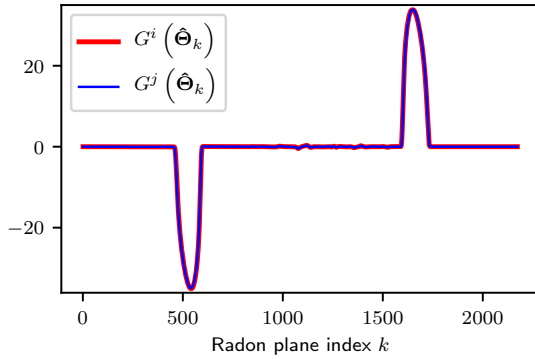
Instead of pre-computing the correction polynomial, Li et al. proposed a calibration-free algorithm to calculate the polynomial for mono-material correction [62]. First, a binary volume is segmented from the prior image, reconstructed from the uncorrected projections. The path length through the volume along each projection ray is computed by the forward projection of binary volume. The geometry and material-specific correction polynomial is estimated by curve fitting, as described in Sec. 2.7.1. Thus, a calibration-free beam hardening correction can be performed with the additional costs of reconstruction and forward projection. Empirical Beam Hardening Correction (EBHC) proposed by Kyriakou et al. (Sec. 2.7.1) can be modified to perform water correction in volume space as a post-processing method [58]. The water corrected volume can be expressed as a linear combination of the following basis volumes:

$$\begin{aligned}
 \mu_w(\mathbf{x}) &= \mathcal{X}_3^{-1}\{g_w\} \\
 &= \sum_{c=1}^{N_w} w_c \mathcal{X}_3^{-1}\{[g_p]^c\} \\
 &= w_1 \mu_1^b(\mathbf{x}) + w_2 \mu_2^b(\mathbf{x}) + \dots + w_{N_w} \mu_{N_w}^b
 \end{aligned} \tag{3.2}$$

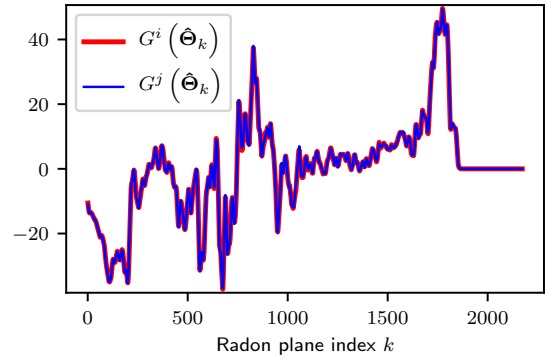
The key idea behind EBHC is to estimate the polynomial coefficients by increasing the flatness of the water corrected image. Hence, the polynomials are calculated by minimizing Total Variation (TV):

$$\min_w \int_{\mathbf{x} \in \mathbb{R}^3} \|\nabla \mu_w(\mathbf{x})\|_1 \, d\mathbf{x} \tag{3.3}$$

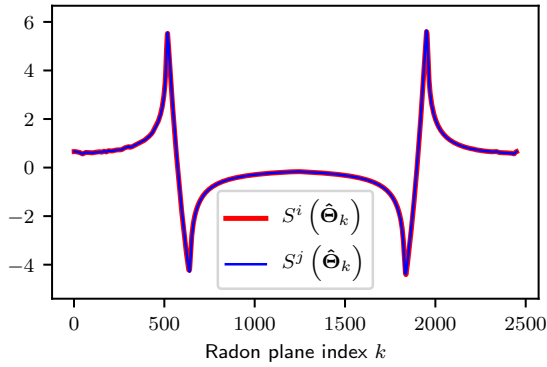
TV-based water correction does not require uncorrected projections g_p since they can be generated by the forward projection of the artifact corrupted volume $\mu_1^b(\mathbf{x})$. The main disadvantage of TV-based water correction is the need for $N_w - 1$ additional reconstructions and forward projections (when uncorrected projections are not available). Therefore, the integration of TV-based correction to the reconstruction



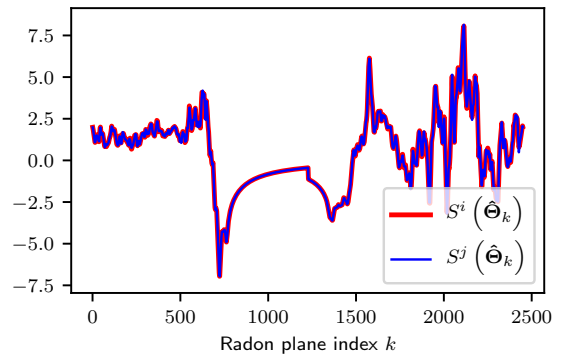
(a) Elliptical cylinder phantom



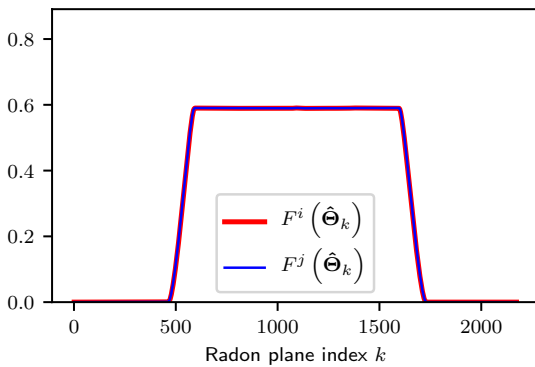
(b) Head phantom



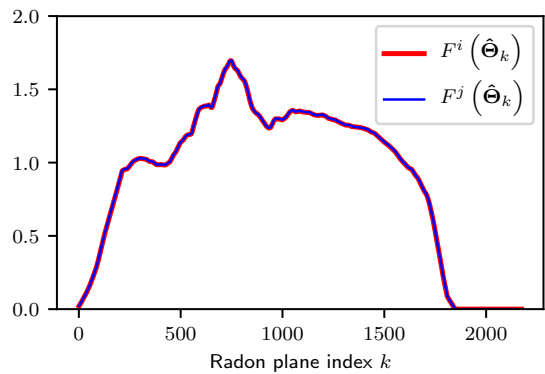
(c) Elliptical cylinder phantom



(d) Head phantom



(e) Elliptical cylinder phantom



(f) Head phantom

Figure 3.1: Grangeat (a, b), Smith (c, d), and fan beam (e, f) intermediate functions computed from the monochromatic projections of the elliptical cylinder and head phantoms.

pipeline demands significant changes in the software architecture due to the necessary additional operations.

All the consistency conditions mentioned in Sec. 2.6 assume that the projections are measured under ideal conditions. The geometrical (e.g., miscalibration, motion) and physical measurement (e.g., beam hardening, scatter) errors introduce inconsistency and invalidate the equivalence relations of consistency conditions. The error-free projections can be estimated from the uncorrected projections using the parameterized models of artifact correction. The key idea behind any artifact reduction algorithms using consistency conditions is to optimize the model parameters by minimizing a cost function quantifying the projection dataset's inconsistency. In this way, consistency conditions have been successfully utilized to reduce the artifacts due to miscalibration [30] [60], motion [37] [96] and scatter [57]. Mou et al. and Tang et al. initiated the attempts to reduce the artifacts due to beam hardening using consistency conditions [69] [88]. They employed zeroth-order HLCC for fan beam CT with a line detector to optimize the polynomials for water correction. For a CBCT system with a flat detector, HLCC can be enforced on the projection values of the 1D line detector formed by the intersection of the source trajectory plane and the 2D flat detector. Using Eq. 2.73 for all rotation angles and detector bins, a system of linear equations was generated. Finally, the polynomial was estimated by solving the equations using the least square method. However, the algorithm cannot be applied to clinical CBCT systems like interventional or mobile C-arm CBCT, where the trajectory of source-detector assembly is not a perfect circle due to mechanical constraints. By relying on a single fan of cone beam projection, the polynomial optimization may not be robust if the projections are corrupted with the additional error due to Poisson noise, scatter, and miscalibration. The number of acquired cone beam projections is very limited in Tomosynthesis and interventional C-arm CBCT using fast scan protocols. As a result, the accuracy and efficiency of the polynomial estimation will be compromised due to the reduced number of equations.

In this chapter, a novel calibration-free beam hardening correction algorithm is discussed to overcome the limitations of the previous methods. All the pair-wise consistency conditions mentioned in Sec. 2.6 involve an inherent assumption that the projections are free from beam hardening artifacts and acquired with a monochromatic X-ray source. Grangeat, Smith, and fan beam intermediate functions computed from the monochromatic projection pairs exhibit a high degree of similarity, as displayed in Fig. 3.1. The polychromatic X-ray spectrum and the energy dependency of attenuation coefficients introduce significant inconsistencies. For the mono-material objects, water correction yields virtual monochromatic projections ($g_w \approx g_m$) and thereby reduces the inconsistency. The optimal correction polynomial can be estimated by enforcing the pair-wise consistency conditions on the uncorrected cone beam projections. Since the equivalence relation of the condition is between the intermediate functions computed from a pair of cone beam projections, the need for a perfect circular trajectory is eliminated. By considering the planes around the baseline connecting two source positions, numerous redundant values can be computed

from a single projection pair. Thus, by utilizing many projection pairs of a cone beam dataset, a robust estimation of the correction polynomial is feasible. Since the polynomials are directly estimated from the projections, no additional reconstructions and forward projections are required, as in TV-based corrections. Hence, the algorithm can be integrated with the reconstruction software without significant changes.

The beam hardening correction using Grangeat Consistency Conditions was introduced in [12] and described in detail in [13]. Würfl et al. demonstrated the feasibility of computationally efficient estimation of the polynomial for first-order correction using GCC [94]. In this chapter, the efficacy and efficiency of polynomial estimations using three pair-wise cone beam consistency conditions are analyzed and compared.

3.2 Method

The inconsistency of water corrected projections parameterized by the polynomial \mathbf{w} can be quantified using a dissimilarity measure like Sum of Squared Differences (SSD). The quantified inconsistency between a pair of water corrected projections corresponding to the projection indices i and j ($i, j \in \{0, 1, \dots, N_\alpha - 1\}, i \neq j$) using GCC (Eq. 2.84) is given below:

$$\mathcal{E}_{GCC}^{ij}(\mathbf{w}) = \sum_{k=0}^{K-1} \left[G^i(\hat{\Theta}_k; \mathbf{w}) - G^j(\hat{\Theta}_k; \mathbf{w}) \right]^2 \quad (3.4)$$

where

$$\begin{aligned} G^i(\hat{\Theta}_k; \mathbf{w}) &= G^i(s_k^i, \theta_k^i; \mathbf{w}) \\ &= \frac{(s_k^i)^2 + (D^i)^2}{(D^i)^2} \frac{\partial}{\partial s_k^i} \mathcal{R}_2 g_{\mathbf{w}}^c(\theta_k^i, s_k^i) \end{aligned} \quad (3.5)$$

Similarly, inconsistency can also be quantified using SCC (Eq. 2.87) and FBCC (Eq. 2.89).

$$\mathcal{E}_{SCC}^{ij}(\mathbf{w}) = \sum_{k=0}^{K-1} \left[S^i(\hat{\Theta}_k; \mathbf{w}) - S^j(\hat{\Theta}_k; \mathbf{w}) \right]^2 \quad (3.6)$$

$$\begin{aligned} S^i(\hat{\Theta}_k; \mathbf{w}) &= S^i(s_k^i, \theta_k^i; \mathbf{w}) \\ &= \frac{(s_k^i)^2 + (D^i)^2}{(D^i)^2} h_r(s_k^i) * \mathcal{R}_2 g_{\mathbf{w}}^c(\theta_k^i, s_k^i) \end{aligned} \quad (3.7)$$

$$\mathcal{E}_{FBCC}^{ij}(\mathbf{w}) = \sum_{k=0}^{K-1} \left[F^i(\hat{\Theta}_k; \mathbf{w}) - F^j(\hat{\Theta}_k; \mathbf{w}) \right]^2 \quad (3.8)$$

$$\begin{aligned}
 F^i \left(\hat{\Theta}_k; \mathbf{w} \right) &= F^i \left(s_k^i, \theta_k^i; \mathbf{w} \right) \\
 &= \frac{-1}{\langle \hat{\mathbf{w}}(\alpha_i), \frac{\mathbf{f}(\alpha_i) - \mathbf{f}(\alpha_j)}{\|\mathbf{f}(\alpha_i) - \mathbf{f}(\alpha_j)\|_2} \rangle} \mathcal{R}_2 g_{\mathbf{w}}^{c,d} \left(\theta_k^i, s_k^i \right)
 \end{aligned} \tag{3.9}$$

We refer $\mathcal{E}^{ij}(\mathbf{w})$ as a generalized inconsistency measure independent of the cone beam consistency conditions. As Fig. 2.9a demonstrates, the error due to polychromatic attenuation is proportional to the path length through the volume (along each X-ray). The forward projections of the binary volume can be considered as the path length projections. If the imaged object exhibits a high degree of rotational asymmetry, the beam hardening-induced inconsistency is correlated to the corresponding path length projection pair's dissimilarity. The path length differential will be very low if $|\langle \mathbf{f}(\alpha_i), \mathbf{f}(\alpha_j) \rangle| \rightarrow 1$. The quantified inconsistency between nearly orthogonal projection pairs ($\langle \mathbf{f}(\alpha_i), \mathbf{f}(\alpha_j) \rangle \rightarrow 0$) is relatively high, and they are selected for the minimization. For clinical C-arm CBCT, the selection of perfect orthogonal projections pairs ($\langle \mathbf{f}(\alpha_i), \mathbf{f}(\alpha_j) \rangle = 0$) may not be possible due to the irregular or wobbling source trajectory caused by the instability of robotic C-arms. Ideally, the projection pairs of a high degree of inconsistency can be estimated by ranking the projection pairs after computing the inconsistency measures. However, the selection of nearly orthogonal projection pairs is very computationally efficient for full and short scans. As the correction is achieved using a unique polynomial expression for all projections, the optimal polynomial coefficients can be estimated from a limited number of pairs. In clinical C-arm CBCT, the first few projections exhibit a drastic difference in attenuation values due to the tube voltage and current adjustment. We selected every 10th orthogonal projection pair of the final half-circle source trajectory to accelerate the optimization. The mean of inconsistency values \mathcal{E}^{ij} computed from the selected projection pairs is the objective function (inconsistency measure) of the optimization. Due to the absence of high frequency emphasizing derivative or ramp filter, FBCC-based inconsistency measure is significantly low (Fig. 3.1). For a valid comparison of the objective function's convergence using different consistency conditions, identical optimization parameters (e.g., stopping criteria) need to be used. Hence, the objective function's value is normalized by the inconsistency measure computed from the uncorrected projections during each iteration.

Identity function $p_{\mathbf{w}_0}(x) = x$, $\mathbf{w}_0 = [0, 1, \dots, 0, 0, 0]^T$ is chosen as the initial parameter for the optimization. If the projections are free from beam hardening artifacts (e.g., monochromatic or water corrected projections), the algorithm cannot minimize the inconsistency measure, and the correction will be performed with the initial parameter. Thus, any degradation of image quality is prevented due to inaccurate polynomial expression.

The computation of intermediate function constitutes linear sub-operations of weighting, integration, differentiation, and ramp filtering. Since SSD is an amplitude-variant

dissimilarity metric, inconsistency measure can be minimized with the trivial solution of zero polynomial ($\mathbf{w} = \mathbf{0}$) or any linear function of slope < 1 . Hence, the optimization of arbitrary degree polynomial is performed by keeping a minimum area under the polynomial curve. The area under the identity function is set as the minimum area and is computed with the robust maximum (99 percentile) of attenuation values of the selected projection pairs g_p^{max} (Fig. 3.2).

$$\int_0^{g_p^{max}} p_{\mathbf{w}_0}(x) dx = \frac{(g_p^{max})^2}{2} \quad (3.10)$$

The constraint ensures the optimization of nonlinear polynomial, and its nonlinearity is proportional to the magnitude of projection error induced by beam hardening. The optimization of N_w degree polynomial can be mathematically expressed as:

$$\begin{aligned} \min_{\mathbf{w}} \quad & \frac{\sum_i \sum_j \mathcal{E}^{ij}(\mathbf{w})}{\sum_i \sum_j \mathcal{E}^{ij}(\mathbf{w}_0)} \quad \text{where } \langle \mathbf{f}(\alpha_i), \mathbf{f}(\alpha_j) \rangle \approx 0 \\ \text{s.t.} \quad & \int_0^{g_p^{max}} p_{\mathbf{w}}(x) dx \geq \frac{(g_p^{max})^2}{2} \end{aligned} \quad (3.11)$$

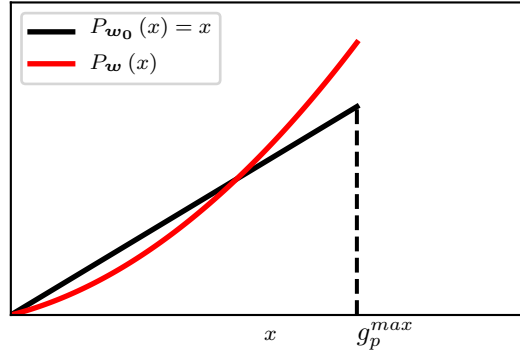


Figure 3.2: The correction polynomial and identity function (initial parameter). During the optimization, the polynomial curves are constrained to keep a minimum area (the area of right-angled triangle).

In clinical CT imaging, CT number or Hounsfield Unit (HU) consistency is essential to maintain after any correction algorithms [48]. The reconstructed images of homogeneous phantoms of unique material composition but with different geometries should have similar HU values under ideal conditions. For the optimization of lower degree polynomials ($N_w = 2, 3$), the inequality constraint can be replaced with an

equality constraint to ensure CT number consistency.

$$\begin{aligned} \int_0^{g_p^{max}} p_{\mathbf{w}}(x) \, dx &= \int_0^{g_p^{max}} p_{\mathbf{w}_0}(x) \, dx \\ &= \frac{(g_p^{max})^2}{2} \end{aligned} \quad (3.12)$$

As per many clinical studies, the second-degree polynomial is sufficient to reduce the cupping artifacts due to the spectral attenuation properties of water and soft tissues [48]. In industrial CT, the artifacts can be corrected with the second-degree polynomial for the objects made up of polymers and thin metals [27]. In the beam hardening correction using second-degree polynomial, the magnitude of artifact reduction is exclusively determined by the leading coefficient or the non-linear term w_2 . By evaluating the above equation using the second-degree polynomial:

$$\begin{aligned} \int_0^{g_p^{max}} [w_2 x^2 + w_1 x] \, dx &= \frac{(g_p^{max})^2}{2} \\ w_2 \frac{(g_p^{max})^3}{3} + w_1 \frac{(g_p^{max})^2}{2} &= \frac{(g_p^{max})^2}{2} \end{aligned} \quad (3.13)$$

By rearranging the terms, the linear coefficient of the polynomial can be expressed as a function of the nonlinear term.

$$w_1 = 1 - \frac{2}{3} w_2 g_p^{max} \quad (3.14)$$

If there is no photon starvation, the mapping between the path length through the volume and the polychromatic total attenuation is one-to-one, as shown in Fig. 2.9a. Besides, the non-linear error due to the underestimation of attenuation values increases proportionally with the path length. Hence, we can safely assume that the second-degree beam hardening correction polynomial is convex and monotonically increasing in the interval $[0, g_p^{max}]$. Consequently, $w_2 \geq 0$ and the abscissa of parabola's vertex is ≤ 0 .

$$\begin{aligned} \frac{-w_1}{2w_2} &\leq 0 \\ \frac{\frac{2}{3} w_2 g_p^{max} - 1}{2w_2} &\leq 0 \\ \frac{g_p^{max}}{3} - \frac{1}{2w_2} &\leq 0 \\ w_2 &\leq \frac{3}{2g_p^{max}} \end{aligned} \quad (3.15)$$

Table 3.1: NLOPT optimization parameters (water correction). The default values were used for all the parameters which are not listed here.

Parameter	value
Algorithm	COBYLA
Number of optimization variables	1
Lower bound	0
Upper bound	$\frac{3}{2g_p^{max}}$
Absolute tolerance on the function value	1e-6
Absolute tolerance on the optimization parameter	1e-6

By incorporating the inequalities, a computationally efficient constrained optimization of the second-degree polynomial can be formulated:

$$\begin{aligned} \min_{w_2} \frac{\sum_i \sum_j \mathcal{E}^{ij}(w_2)}{\sum_i \sum_j \mathcal{E}^{ij}(w_2 = 0)} \text{ where } \langle \mathbf{f}(\alpha_i), \mathbf{f}(\alpha_j) \rangle \rightarrow 0 \\ \text{s.t. } 0 \leq w_2 \leq \frac{3}{2g_p^{max}} \end{aligned} \quad (3.16)$$

The lower and upper bound constraints accelerate the minimization by limiting the search space. Most implementations of the optimization algorithms allow bound constraints on the optimization variable compared to the nonlinear equality or inequality constraints. In all experiments, the optimization is performed with the derivative-free COBYLA algorithm of NLOPT software [51] [76]. The important optimization parameters are listed in Table. 3.1. After optimizing \mathbf{w} from the selected projection pairs, all water corrected projections can be computed using Eq. 3.1. The complete workflow of the reconstruction of water corrected volume is shown in Fig. 3.3.

When mono-material metal objects are imaged in industrial CT, the projections' non-linear error is significantly high due to strong beam hardening. Hence, higher degree polynomials are needed ($N_w \geq 4$) for effective artifact reduction. The equality constraint (Eq. 3.12) may be difficult to maintain during the optimization of higher degree polynomials. Therefore, it may be necessary to perform the optimization using Eq. 3.11. If $w_2 \cong \frac{3}{2g_p^{max}}$ after the minimization using Eq. 4.10, we can infer that the second-degree polynomial may not be sufficient for adequate correction.

Instead of quadratic error function-based distance metrics (e.g., SSD, MSE), the inconsistency measure can also be computed using robust dissimilarity measures. Preuhs et al. utilized the Sum of Geman-Mcclure Differences (SGMD) to quantify the inconsistency for GCC-based estimation of symmetry planes [77]:

$$\mathcal{E}_{GCC}^{ij} = \sum_{k=0}^{K-1} \frac{\left[G^i(\hat{\Theta}_k; \mathbf{w}) - G^j(\hat{\Theta}_k; \mathbf{w}) \right]^2}{1 + \frac{1}{\sigma} \left[G^i(\hat{\Theta}_k; \mathbf{w}) - G^j(\hat{\Theta}_k; \mathbf{w}) \right]^2} \quad (3.17)$$

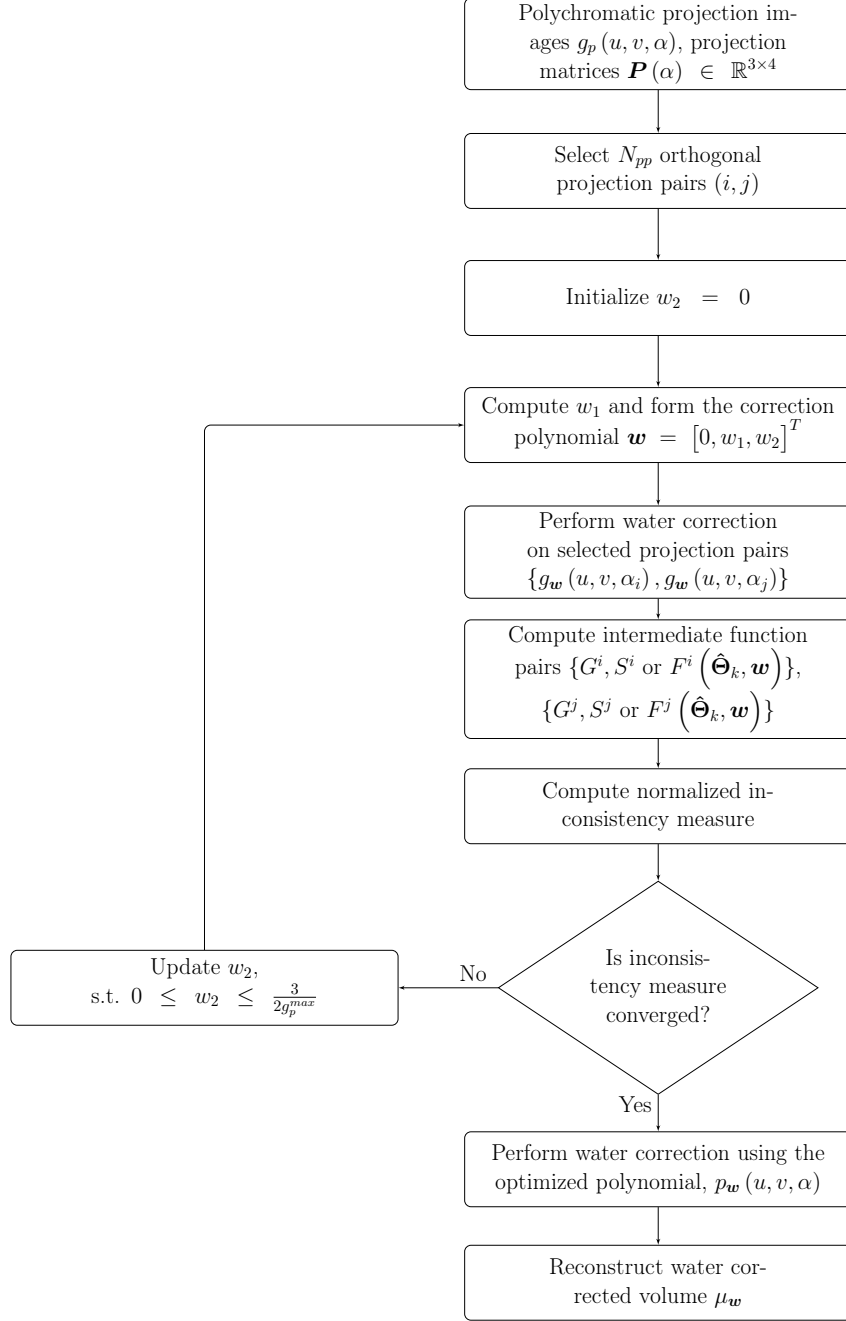


Figure 3.3: The workflow of consistency condition-based first-order (water) correction using second-degree polynomials.

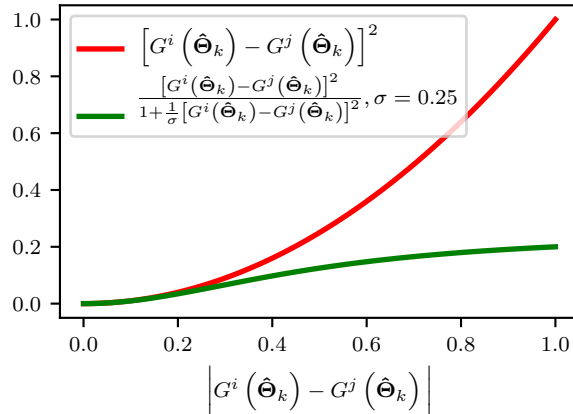


Figure 3.4: Quadratic and Geman-Mcclure error functions.

The value of $\sigma = 0.25$ was empirically determined. As shown in Fig. 3.4, the Geman-Mcclure error function penalizes the large differences preventing over-correction in GCC-based artifact reductions if the volume contains small metal structures or the projections are truncated.

3.3 Experiments

3.3.1 Simulation Studies

To study the efficacy of the proposed beam hardening correction algorithms, polychromatic raw I_t and flat field I_0 images were simulated using GATE Fixed Forced Detection Actor (FFDA) [50]. Ideal energy integrating flat detector with the spectral response $\mathcal{D}(E) = 1, \forall E$ was used for simulation. Before log transformation to compute the total attenuation values g_p , raw and flat field images were corrupted with Poisson noise where the number of photons per detector element was set to 50000. The projections were simulated according to a full scan circular source trajectory. The important geometry parameters are listed in Table. 3.2. Two distinct X-ray spectra correspond to low (LE) and high energies (HE) were utilized for simulations to validate the effectiveness of energy-specific beam hardening corrections. The spectra were generated with Spekcalc program as per the simulation parameters listed in Table. 3.3 [75]. Fig. 3.5 depicts low and high energy spectra after unit area normalization.

The polychromatic projections were generated from the mono-material and homogeneous brain [21] and elliptical cylinder phantoms consisting of water (density = 1 g/cm^3). The density and the linear attenuation coefficient of cortical bones are significantly higher than soft tissues or water. To assess the mono-material correction's efficacy for the objects composed of more than one material, the polychromatic projections were also generated from the head phantom containing water and bone

Table 3.2: CBCT system geometry parameters.

Parameter	value
Source to isocenter distance	1000 mm
Source to detector distance	1536 mm
Number of detector columns	512
Number of detector rows	512
Pixel width	0.8 mm
Pixel height	0.8 mm
Detector size	409.6x409.6 mm ²
Number of projections	360
Rotation angular range	0-359 degree

Table 3.3: X-ray spectra simulation parameters.

Parameter	Low energy (LE)	High energy (HE)
Peak energy (kVp)	80 keV	120 keV
Minimum energy	8 keV	12 keV
Energy bin width	1.0 keV	1.0 keV
Anode material	Tungsten	Tungsten
Anode angle	12 degree	12 degree
Filter material	Aluminium	Aluminium
Filter thickness	2 mm	4 mm

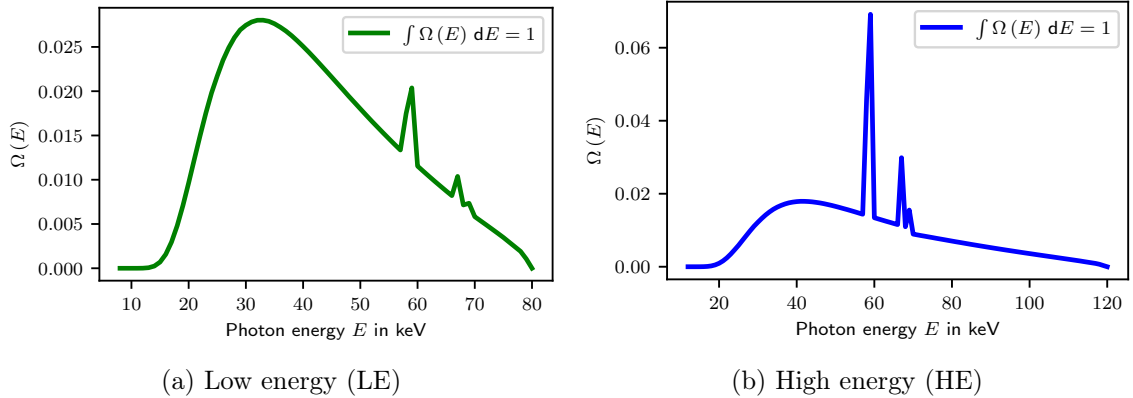


Figure 3.5: X-ray spectra used for the simulation study.

(density = 1.85 g/cm³) [21]. The images were reconstructed using the FDK algorithm of reconstruction software developed as a part of the Ph.D. project. Before voxel-driven cone-beam back-projection, the projections were filtered using a Hann windowed ramp filter, where the cut-off frequency was set to 50% of Nyquist frequency. The images were reconstructed without additional artifact reductions. 3D spatial distribution of linear attenuation coefficients in mm⁻¹ is converted to Hounsfield Unit with the linear attenuation coefficients of water 0.0248 mm⁻¹ and 0.0209 mm⁻¹ for low and high energy spectra. The images were reconstructed from the uncorrected projections (NC) and after CC-based beam hardening corrections (GCC, SCC, and FBCC). The images were also reconstructed after calibration-based water correction (WC) for comparison. The polynomials were calibrated using a cylindrical water phantom of diameter 20 cm.

To compare calibration-free algorithms, the uncorrected reconstructed images were post-processed with the Total Variation (TV)-based water correction as explained in the introduction section (Eq. 3.3 and Eq. 3.2). The polynomials were optimized after minimizing the TV of water corrected volume subjected to bound constraints:

$$\begin{aligned} \min_{w_2} \int_{\mathbf{x} \in \mathbb{R}^3} \|\nabla \mu_w(\mathbf{x})\|_1 \, d\mathbf{x} \\ \text{s.t. } 0 \leq w_2 \leq \frac{3}{2g_p^{max}} \end{aligned} \quad (3.18)$$

Quantitative accuracy

Apart from evaluating mere artifact reductions, supplementary experiments were conducted to assess the quantitative accuracy after corrections. CT number or HU accuracy in clinical imaging has two essential characteristics:

1. CT number uniformity: Reconstructed images of homogeneous and mono-material phantoms should have similar CT numbers (in HU) after beam hardening corrections. The ideal reconstructed image with a unique voxel value is not feasible due to the addition of Poisson noise and the reconstruction errors (e.g., aliasing and interpolation errors). The uniformity of CT numbers was visualized with the plots of attenuation profiles. In addition, the in-homogeneity of voxel values of cone beam artifact-free central slice ($z = 0$) was quantified with a robust coefficient of variation C_v^r , the ratio of Median Absolute Deviation (MAD) and median [22]:

$$C_v^r = \frac{\text{MAD}\{\mu(\mathbf{x})\}}{\text{median}\{\mu(\mathbf{x})\}} \times 100 \text{ where } \mu(\mathbf{x}) > 0.0, z = 0 \quad (3.19)$$

While computing the coefficient of variation, the background voxels were avoided using a threshold segmentation. Due to the presence of bone voxels and bone-induced beam hardening artifacts, C_v^r was not computed from the head phantom images.

2. CT number consistency: After reconstruction with beam hardening corrections, the phantoms of unique material composition but different geometries should have identical CT numbers under ideal conditions. The median of voxel values (in HU) of the central slice was computed to assess CT number consistency.

3.3.2 Robustness of Algorithms

As explained in Sec. 2.6, none of the cone beam consistency conditions mentioned in this thesis fully characterize the projection data since the conditions are necessary but not sufficient. Beam hardening correction algorithms are formulated assuming that the projections are free from other geometrical and physical measurement errors. However, the polychromatic projections are often perturbed by the error due to various physical phenomena like Poisson noise and scatter. The errors can also be contributed by the inaccurate or sub-optimal pre-processing algorithms and the constraints on system geometry (e.g., truncation due to small detector size or FOV). Therefore, the correction algorithm's effectiveness was studied after simulating the projections with various errors. The estimated polynomials from the Poisson noise (corresponding to 50000 photons per detector pixel) corrupted polychromatic projections were considered ground truth \mathbf{w}_{gt} . The polynomials were optimized after corrupting the polychromatic projections with the different magnitudes of errors, and the relative L2 error norms were computed for the comparative evaluation of consistency conditions.

$$\frac{\|\mathbf{w} - \mathbf{w}_{gt}\|_2}{\|\mathbf{w}_{gt}\|_2} \quad (3.20)$$

Poisson noise

To evaluate the algorithms' robustness towards noise, the polychromatic raw I_t and flat field I_0 images were corrupted with an increasing degree of Poisson noise by decreasing the photons per detector pixel, from 50000 to 3000.

Truncation

Lateral and axial truncated projection images were generated by cropping the columns (left and right) and the rows (top and bottom) of all projection images (Fig. 3.6). The maximum number of cropped pixels was 200 reducing the size of each projection image to 112x112. The projection matrices were modified to reflect the changes in projection geometry by shifting the principal points.

Detector shift

To simulate the geometrical errors due to detector shift, the projection images were translated along $\hat{\mathbf{u}}$ (column) and $\hat{\mathbf{v}}$ (row) directions of the Detector Coordinate System (DCS). The projection matrices were not modified to generate miscalibration artifacts

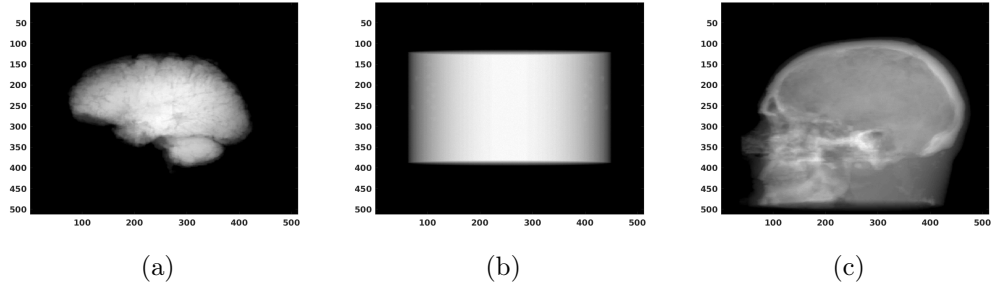


Figure 3.6: Projection image of (a) brain phantom; (b) elliptical cylinder phantom; (c) head phantom.

in the reconstructed images. The detector shift was measured in pixels and the maximum shift applied was 20 pixels.

Scatter

To study the effect of scatter radiation on beam hardening corrections, the scatter images I_s were generated along with the primary intensity (polychromatic) I_t and flat field I_0 images using GATE FFDA. The amount of scatter radiation in the projection images is quantified by the maximum of Scatter Primary Ratios (SPR) SPR_{max} (Eq. 2.111). The scatter contaminated projections g_{ps} were generated from the scatter-free polychromatic projections g_p as per the following equation:

$$g_{ps}(u, v, \alpha) = g_p(u, v, \alpha) - \ln(1 + m SPR(u, v, \alpha)), \quad m \in [0, 1.0] \quad (3.21)$$

By varying the additional factor m , the projections of different SPR_{max} were generated.

Projection Offset

The inaccurate or sub-optimal pre-processing of the projections (e.g., detector calibrations, I_0 , and lag corrections) can affect the accuracy of total attenuation values and the efficacy of beam hardening corrections. Since it is difficult to simulate all the processes that contribute to the error, simplified experiments were conducted to assess the robustness of corrections after adding offset images to the polychromatic projections. First, the projections were corrupted by adding a constant offset value (a fraction of maximum attenuation, g_p^{max}):

$$g_p^e(u, v, \alpha) = g_p(u, v, \alpha) + m g_p^{max}, \quad m \in [0, 0.3] \quad (3.22)$$

The robustness studies were also performed by corrupting the projections with the projection-specific offset values:

$$g_p^e(u, v, \alpha) = g_p(u, v, \alpha) + OS(\alpha) \quad (3.23)$$

By computing the maximum attenuation value of each projection and subsequent sinusoidal curve fitting, the distribution of offsets (frequency and phase of the sine wave) was estimated as shown in Fig. 3.7a. Finally, the projection-specific offsets were computed by setting the minimum offset value to zero and the peak-to-peak amplitude difference to mg_p^{max} , $m \in [0, 0.3]$ (Fig. 3.7b). Thus, by varying m from 0 to 0.3, the projection error was magnified in constant and projection-specific offset experiments.

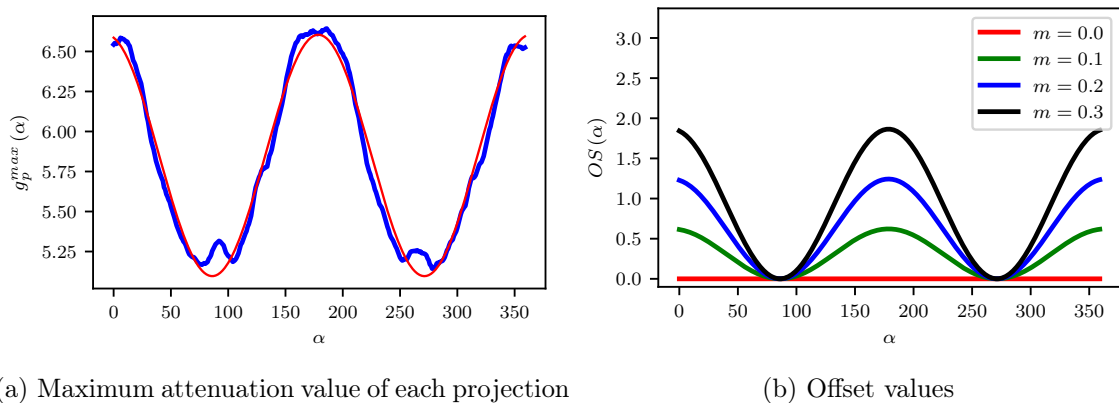


Figure 3.7: Projection-specific offsets.

3.3.3 Real and Clinical Data

The proposed algorithms were validated using the projection data from the industrial and clinical CBCT scanners. The micro-CT projection data of the lower jaw specimen was acquired from the Carl Zeiss Metrotom industrial CT scanner. The projection data acquired at 100 keV comprises 1440 high-resolution images, where each image contains 1456×1840 isotropic pixels of size 0.127 mm. The projections were acquired as per the scanner’s circular source trajectory (full scan). The projections were down-sampled by factor 2, and every second projection was selected to accelerate the reconstruction and limit the memory footprint. The volumes were reconstructed on a grid of $512 \times 512 \times 512$ isotropic voxels of size 0.25 mm.

The head scan projections (108 keV) were acquired from the interventional C-arm CBCT scanner (Artis-Q, Siemens Healthineers, Forchheim, Germany). Each projection dataset contains 496 images of dimension 1240×960 and 0.308 mm pixel resolution. The images after CC-based corrections were compared with the scanner’s calibration-based water corrected images. All the projection images were processed with the scanner’s proprietary scatter correction algorithm before beam hardening correction.

The images were reconstructed using the FDK algorithm. The projections were filtered with a Hann apodized ramp filter where the cut-off frequency was set to 70%

of Nyquist frequency. Since the clinical datasets contain a high degree of noise, the projections were smoothed by 5×5 Gaussian filtering to highlight the soft-tissue contrast improvement.

3.4 Results and Discussion

3.4.1 Simulation

Fig. 3.8, Fig. 3.9, and Fig. 3.10 depict the reduction of cupping artifacts after GCC, FBCC, and SCC-based beam hardening corrections for the brain, elliptical cylinder and head phantoms. Low (LE) and high (HE) energy images are displayed with the same window level and center. It is evident from the figures that the cupping artifacts are significantly high in low-energy images due to a high degree of projection error. By optimizing the energy-specific polynomials, the corrections ensure the reduction of artifacts regardless of the strength of beam hardening. As Fig. 3.11 demonstrates, the optimized polynomials are roughly similar in the interval $[0, g_p^{max}]$ irrespective of the consistency conditions. The low energy correction polynomials exhibit a high degree of nonlinearity compared to their high-energy counterparts. The attenuation profiles (Fig. 3.12) corresponding to linear ROIs segmented from the images (yellow line in NC images) show the effectiveness of correction algorithms to "flatten" the curves by decreasing the in-homogeneity of voxel values. Fig. 3.13 shows the polynomials can be optimized in a limited number of iterations. Besides, all three consistency conditions show similar convergences of inconsistency measures. The computation of fan beam intermediate functions is very efficient due to the lack of additional operations after 2D Radon transform. Smith intermediate functions are computationally expensive and involve a higher memory footprint due to ramp filtering.

Table 3.4: Robust coefficient of variation C_v^r after water corrections.

Image	NC	WC	FBCC	GCC	SCC
Brain phantom (LE)	2.4445	1.7040	1.6224	1.6094	1.5870
Brain phantom (HE)	1.7636	1.7582	1.5951	1.5872	1.5675
Elliptical cylinder (LE)	2.6047	1.7477	1.5770	1.5704	1.5450
Elliptical cylinder (HE)	1.8461	1.7969	1.5317	1.5523	1.5269

The coefficients of variation C_v^r computed from the volumes are listed in Table. 3.4. C_v^r is significantly high for LE images due to the increased in-homogeneity of attenuation values caused by strong beam hardening. The dispersion of voxel values is reduced considerably after corrections. Moreover, C_v^r s computed from LE and HE corrected images are similar due to the energy-specific beam hardening corrections by optimizing apposite polynomials.

Table. 3.5 lists the median attenuation values of water pixels located at the central slice. HU variability is very low after corrections, and thereby, HU consistency

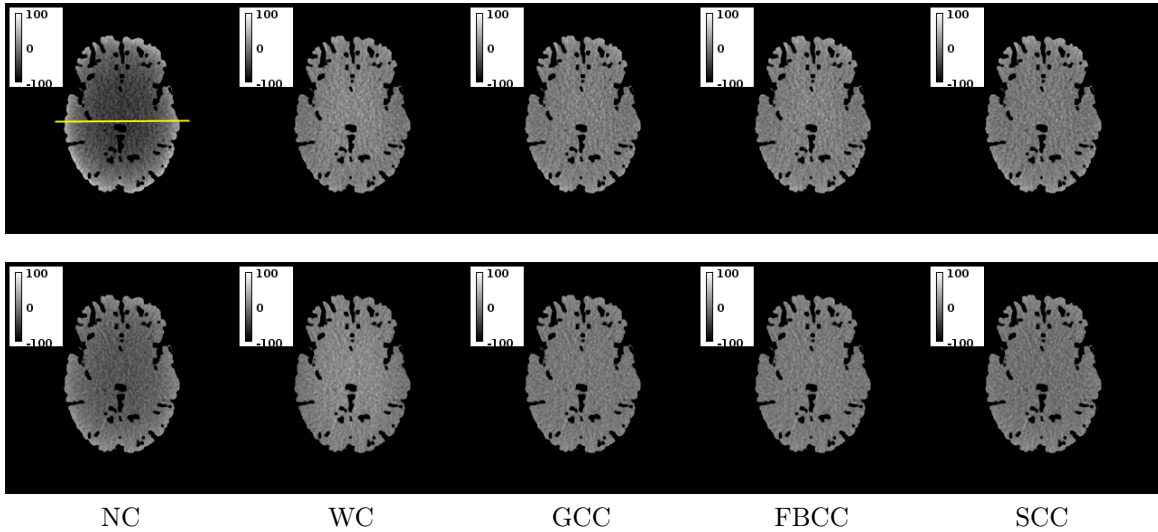


Figure 3.8: Beam hardening correction for the homogeneous brain phantom: NC, reconstructed image without beam hardening correction; WC, after calibration-based water correction; GCC, after GCC-based water correction; FBCC, after FBCC-based water correction; SCC, after SCC-based water correction. Top and bottom row images were reconstructed from the low (LE) and high (HE) energy projections, respectively.

Table 3.5: Median of attenuation values (HU).

Image	NC	WC	GCC	FBCC	SCC
Brain phantom (LE)	-34.7327	-0.2118	-1.5768	-2.7183	-5.4898
Brain phantom (HE)	-21.9835	0.8415	-5.7041	-6.3314	-9.8584
Elliptical cylinder (LE)	-29.4474	3.3436	-12.7171	-12.9393	-13.9193
Elliptical cylinder (HE)	-18.5617	3.9258	-10.6966	-10.1720	-10.8358

is maintained for the volumes of different geometries and sizes. Calibration-based corrections yield volumes of high HU consistency compared to CC-based corrections since the brain and elliptical cylinder phantom projections are corrected with an identical polynomial. We can also find that C_v^r values computed from WC images (Tab. 3.4) are roughly similar.

Fig. 3.14 displays the images after TV-based water correction. For low energy spectra, brain, and elliptical cylinder phantom images indicate under- and over-compensations compared to CC-based corrections. The optimal correction polynomial could not be estimated from the projections of the head phantom. At higher energies where the low-frequency cupping artifacts are not predominant, the minimization of TV-based cost function was only possible for large volume cylinder phantom. Beam hardening corrections were performed with the identity function for low

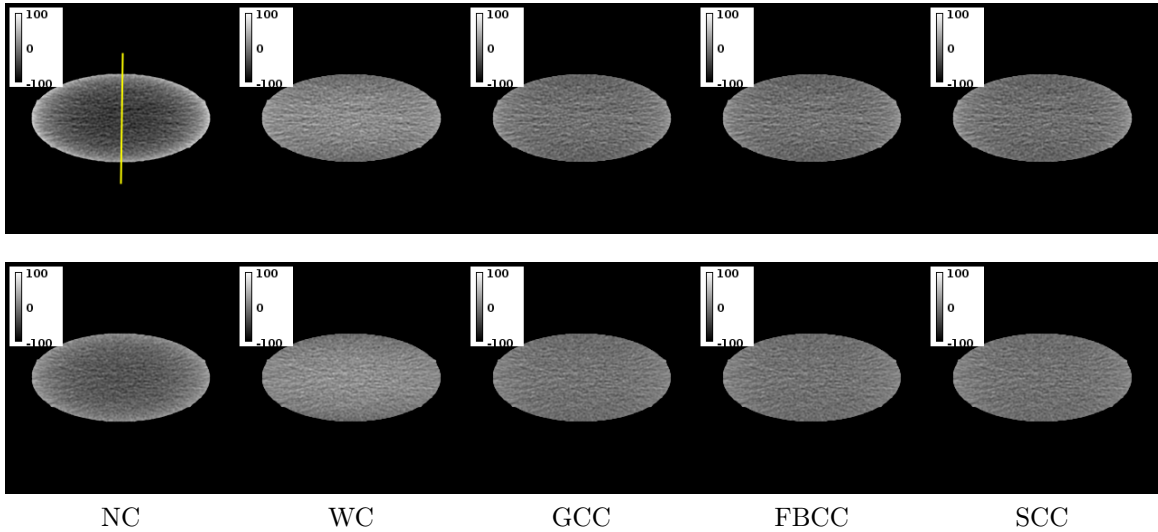


Figure 3.9: Beam hardening correction for the homogeneous elliptical cylinder phantom: NC, reconstructed image without beam hardening correction; WC, after calibration-based water correction; GCC, after GCC-based water correction; FBCC, after FBCC-based water correction; SCC, after SCC-based water correction. Top and bottom row images were reconstructed from the low (LE) and high (HE) energy projections, respectively.

and high energy head phantoms and high energy brain phantom (Fig. 3.14d and Fig. 3.14h). Our studies show the feasibility of TV-based corrections depends on the object’s geometry and the strength of beam hardening artifacts in the uncorrected images. In addition, the computation of gradient images is sensitive to Poisson noise.

CC-based correction algorithms could not minimize the projection inconsistency of objects exhibiting symmetry with respect to the isocenter and around the axis of rotation (e.g., homogeneous and mono-material cylinder). The intermediate functions computed from the projections of rotationally symmetric objects are highly similar. Hence, the inconsistency measure quantified by calculating the dissimilarity of intermediate functions is very low and cannot be minimized with the polynomial corrections. Kim et al. also reported the inability to optimize the scatter kernel for symmetric objects using HLCC [57]. In practice, most of the imaged volumes are of complex geometry, and their rotational asymmetry can be exploited for reliable corrections. The 2-fold rotational symmetry of the elliptical cylinder was circumvented by selecting orthogonal projection pairs, and thereby the correction polynomials could be optimized. If the CBCT systems employ M-Line algorithm for reconstruction where the source-detector pair rotates both in axial and orbital directions (circle + arc trajectory), the correction is feasible for rotational symmetric objects like cylinders [45].

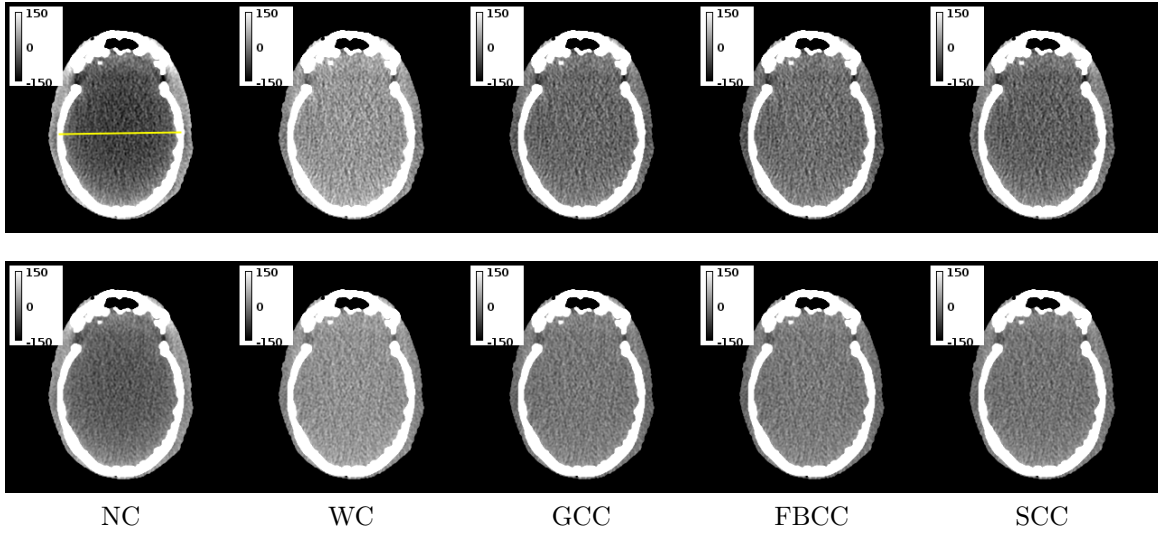


Figure 3.10: Beam hardening correction for the heterogeneous head phantom: NC, reconstructed image without beam hardening correction; WC, after calibration-based water correction; GCC, after GCC-based water correction; FBCC, after FBCC-based water correction; SCC, after SCC-based water correction. Top and bottom row images were reconstructed from the low (LE) and high (HE) energy projections, respectively.

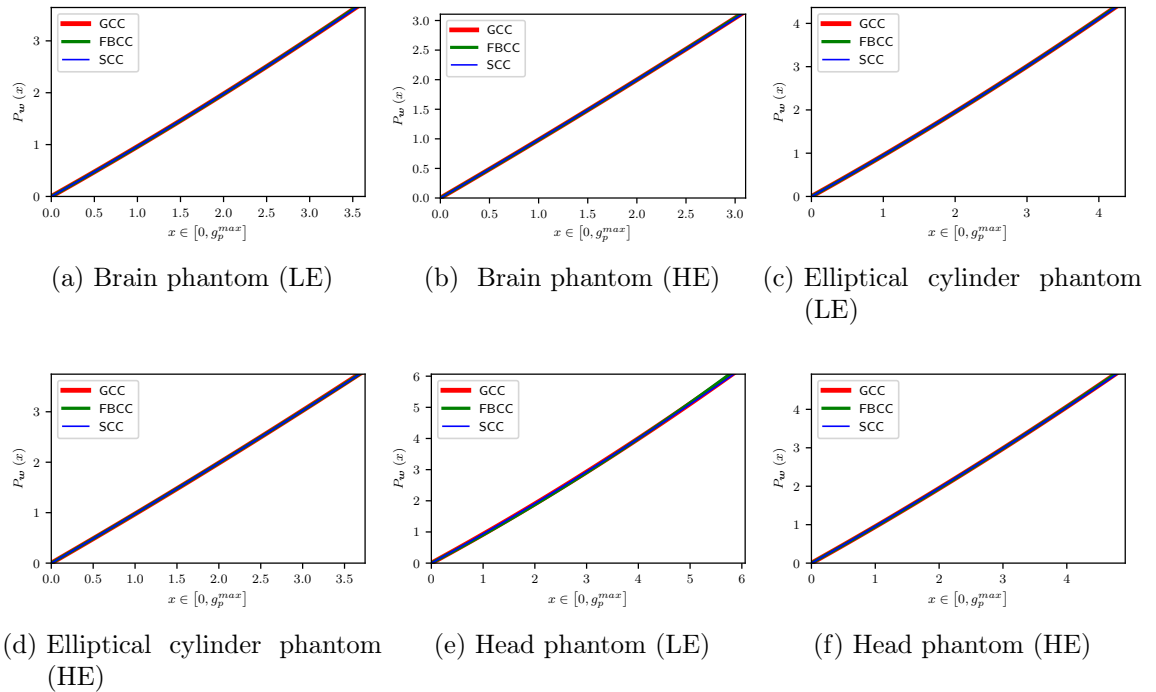


Figure 3.11: Beam hardening correction polynomials (simulation studies).

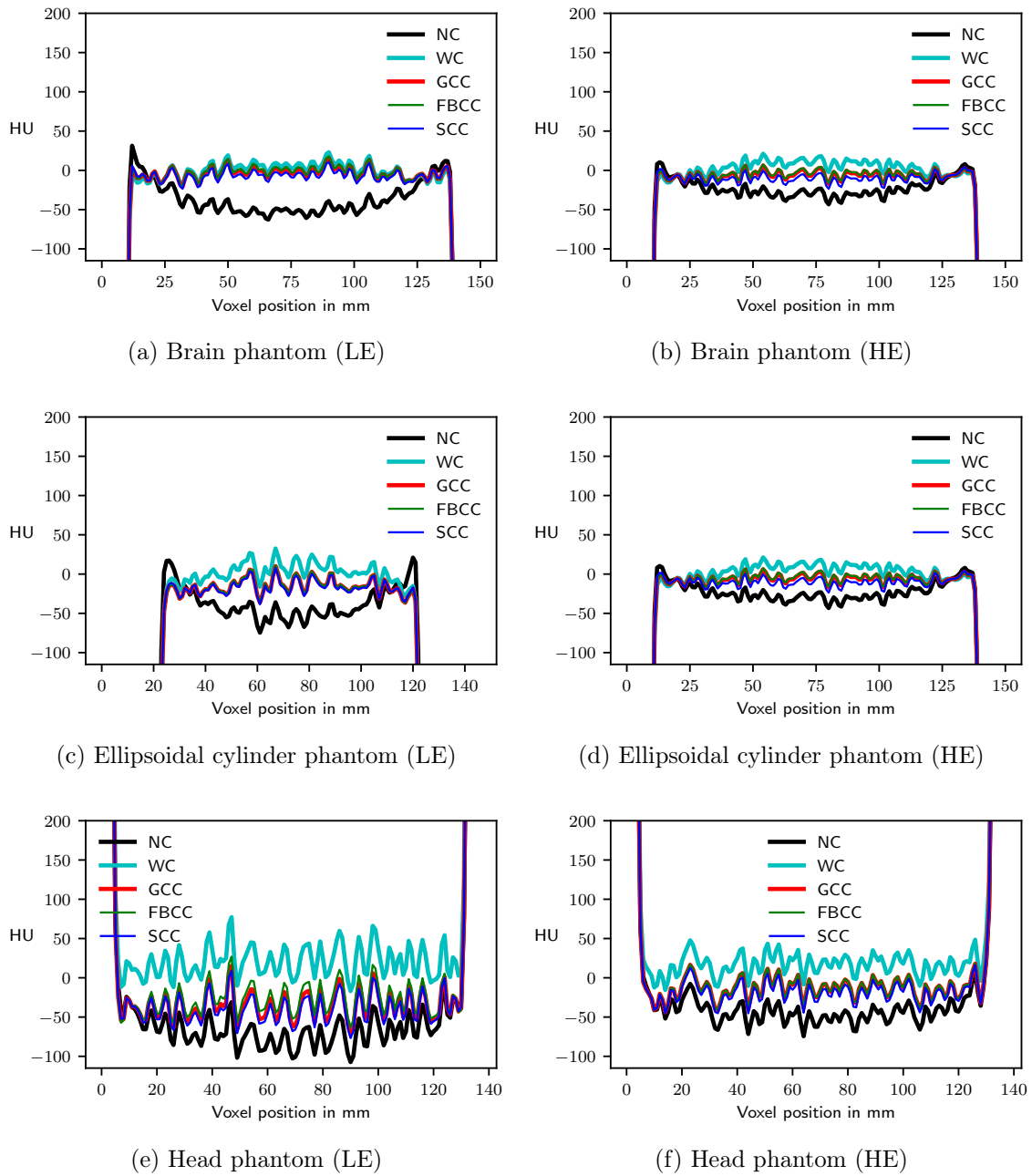


Figure 3.12: The attenuation profiles of linear ROI segmented from the reconstructed images.

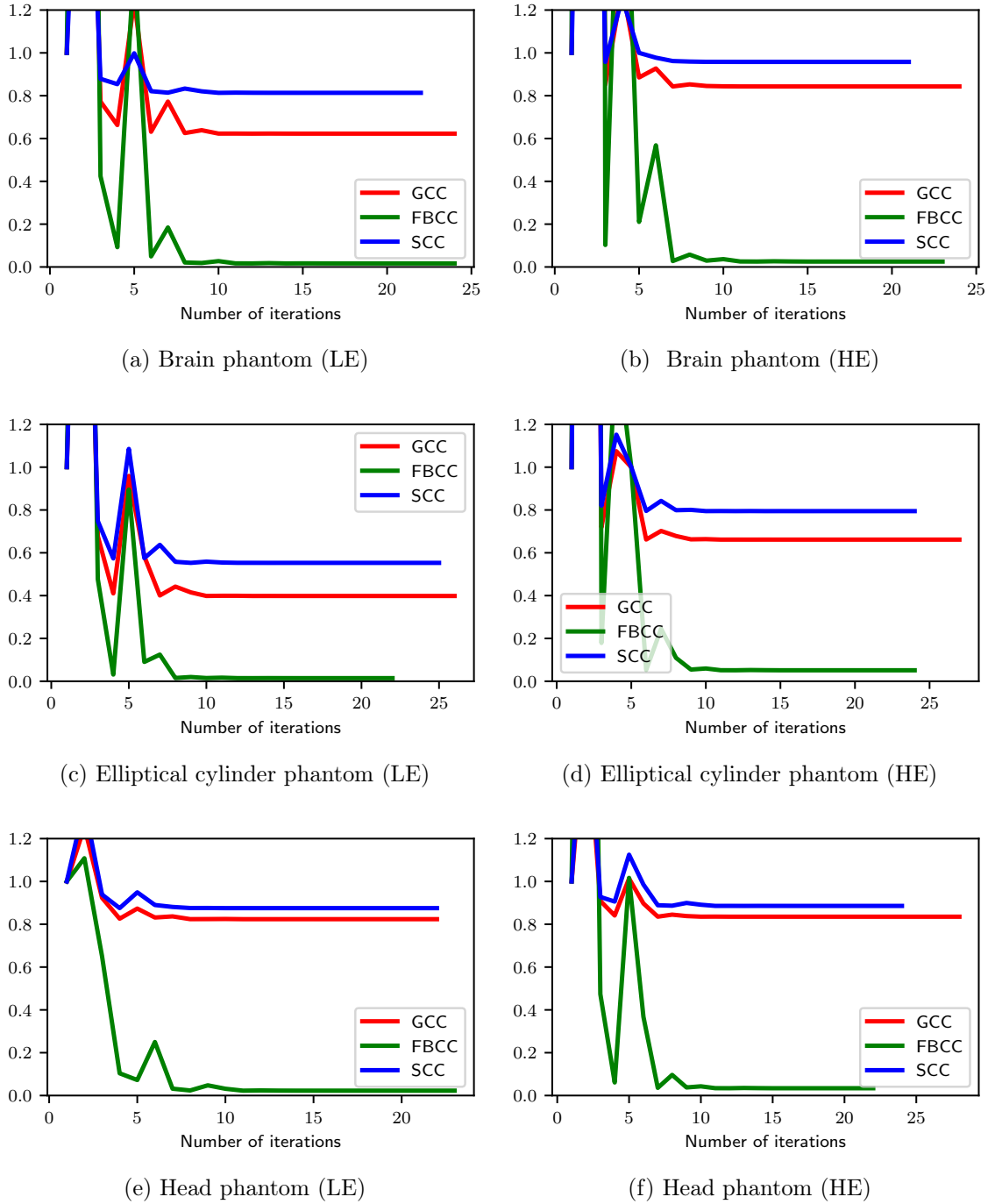


Figure 3.13: The minimization of inconsistency measure (simulation studies).

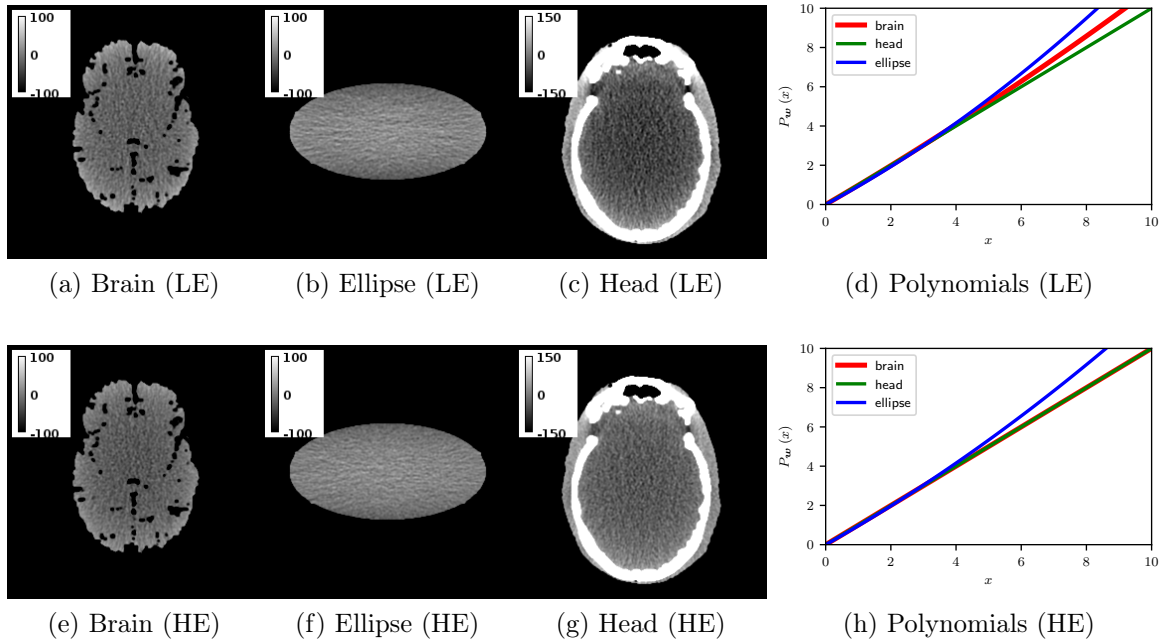


Figure 3.14: TV-based water correction results.

3.4.2 Robustness of Algorithms

Poisson noise

Fig. 3.15 shows the relative polynomial error (Eq. 3.20) for an increasing number of photons per detector pixel. Due to the smoothness of the fan beam intermediate function, FBCC-based polynomial optimization is very robust to noise. SCC and GCC-based algorithms are sensitive to a high degree of Poisson noise due to the presence of high frequency-enhancing ramp and derivative filters. As Fig. 3.16 displays, the fan beam intermediate functions computed from high (50000 photons per pixel) and low (3000 photons per pixel) dose projections exhibit a high degree of similarity compared to Smith intermediate functions. Hence, the same polynomial can be optimized from both projections by the FBCC-based method. The robustness of the GCC-based algorithm can be enhanced by using the outlier resistant SGMD dissimilarity measure (Eq. 3.17). Due to the limited detector gain and high attenuation bones, a large number of photons are necessary for clinical datasets to avoid photon starvation. Hence, all CC-based beam hardening corrections are robust towards Poisson noise for most anthropomorphic phantoms and clinical datasets. It is also to be noted that the derivative and ramp filtering operations of Grangeat and Smith intermediate functions can be modified to enhance the robustness of GCC and SCC-based algorithms (e.g., by employing Savitzky–Golay derivative and Hann apodized ramp filters). In ultra low dose CT imaging and breast CT, FBCC is the preferred consistency condition for beam hardening correction.

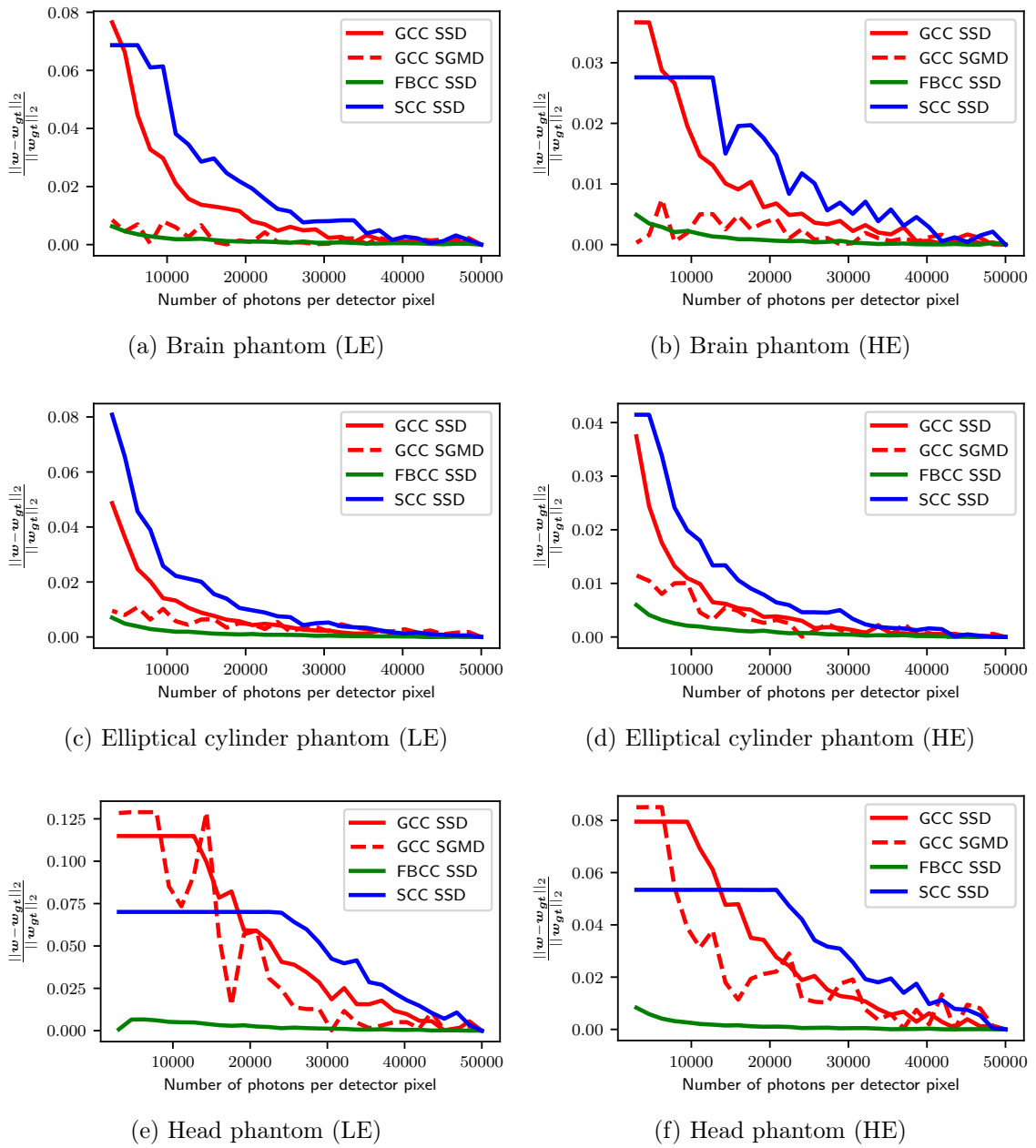
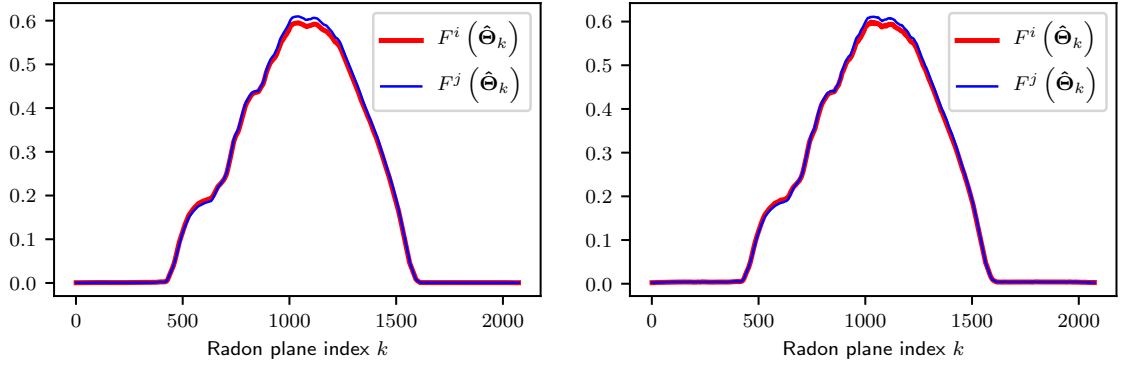
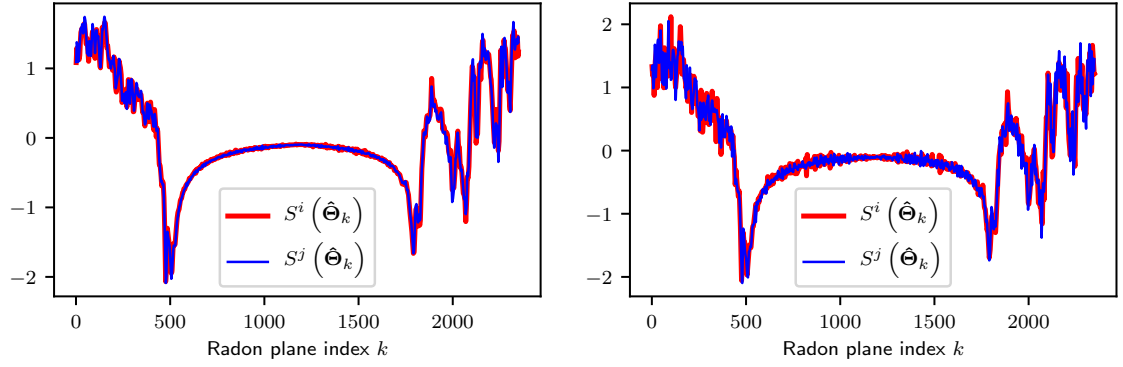


Figure 3.15: Robustness of algorithms (Poisson noise).



(a) Fan beam intermediate functions computed from the high dose projections. (b) Fan beam intermediate functions computed from the low dose projections.



(c) Smith intermediate functions computed from the high dose projections. (d) Smith intermediate functions computed from the low dose projections.

Figure 3.16: Fan beam and Smith intermediate functions computed from the ground truth (high dose) and low dose projections of the brain phantom (LE).

Truncation

Fig. 3.17 shows the robustness of polynomial optimizations under axial truncations. The number of sampled Radon planes around the baseline K (the number of intermediate function vector's elements, Eq. 3.4) decreases after cropping the projection images top and bottom. Since the computation of fan beam intermediate functions (Eq. 4.8) does not consider the adjacent planes, the FBCC-based algorithm is robust towards axial truncation. As Fig. 3.18 shows, intermediate function values computed from the truncated projections can be considered as the segmented values of ground truth intermediate functions. The tolerance towards Poisson noise and the slow varying nature of intermediate function can also make the FBCC-based algorithm robust when the intermediate functions are undersampled. As a result, FBCC-based polynomial optimization is suitable for beam hardening correction in the small cone angle

CBCT systems (e.g., axial scans of MDCT) and VOI imaging. Ramp filtering is a global operation and acts on all the radon planes intersecting the detector (Eq. 4.7). Due to the missing planes, intermediate function values are drastically different after axial truncation (Fig. 3.18), making the SCC-based algorithm very susceptible. The local derivative filter of the Grangeat intermediate function is implemented with the central difference method by considering two adjacent planes making the GCC-based algorithm more robust.

Fig. 3.19 displays the algorithm's robustness under lateral truncations where the projection images are cropped from left and right. All three consistency conditions are sensitive to lateral truncation in equal measures. By penalizing the large errors caused by truncation at the detector edges, the GCC-based algorithm's robustness can be improved by employing the SGMD dissimilarity measure (Eq. 3.17) to quantify the inconsistency. After a certain degree of truncation, the relative polynomial error remains constant, indicating the optimization algorithm's inability to minimize the objective function. Consequently, beam hardening corrections are performed with the initial parameter (identity function).

Fig. 3.20 displays the relative polynomial error when both axial and lateral truncations are applied simultaneously. The resultant plots can be considered as the superposition of axial and lateral truncation polynomial errors. Fig. 3.21 demonstrates the feasibility of artifact reduction when a small degree of truncation is present. Though the algorithms reduced the cupping artifacts after beam hardening corrections, the truncation-induced cupping persists, especially at the top.

Detector shift

Fig. 3.22 and Fig. 3.23 display the robustness of algorithms when the projections are shifted along detector columns \hat{u} and rows \hat{v} to simulate the miscalibration error. The figures show that FBCC-based corrections are very robust to detector shifts compared to other consistency conditions. Shifting along \hat{u} -direction yield shifted intermediate functions and the robustness of the FBCC-based method can be attributed to the slowly varying nature of the fan beam intermediate function (Fig. 3.24). When the projections are shifted along rows (\hat{v}), the FBCC-based method is very robust since the computation of intermediate function does not need the adjacent planes, as evident from the unchanged intermediate functions before and after the detector shift (Fig. 3.25). Fig. 3.26 confirms the robustness of the FBCC-based algorithm when the projections are shifted along both directions simultaneously. Fig. 3.27 displays the images reconstructed from the shifted projections before and after beam hardening corrections. The figures show the feasibility of corrections when the projections contain a small degree of miscalibration errors. The figures and attenuation profiles confirm the superiority of the FBCC-based algorithm to optimize the polynomials from the shifted projections. The artifacts due to inaccurate projection geometry are visible in the images where the bone regions are enlarged compared to the artifact-free images of Fig. 3.10.

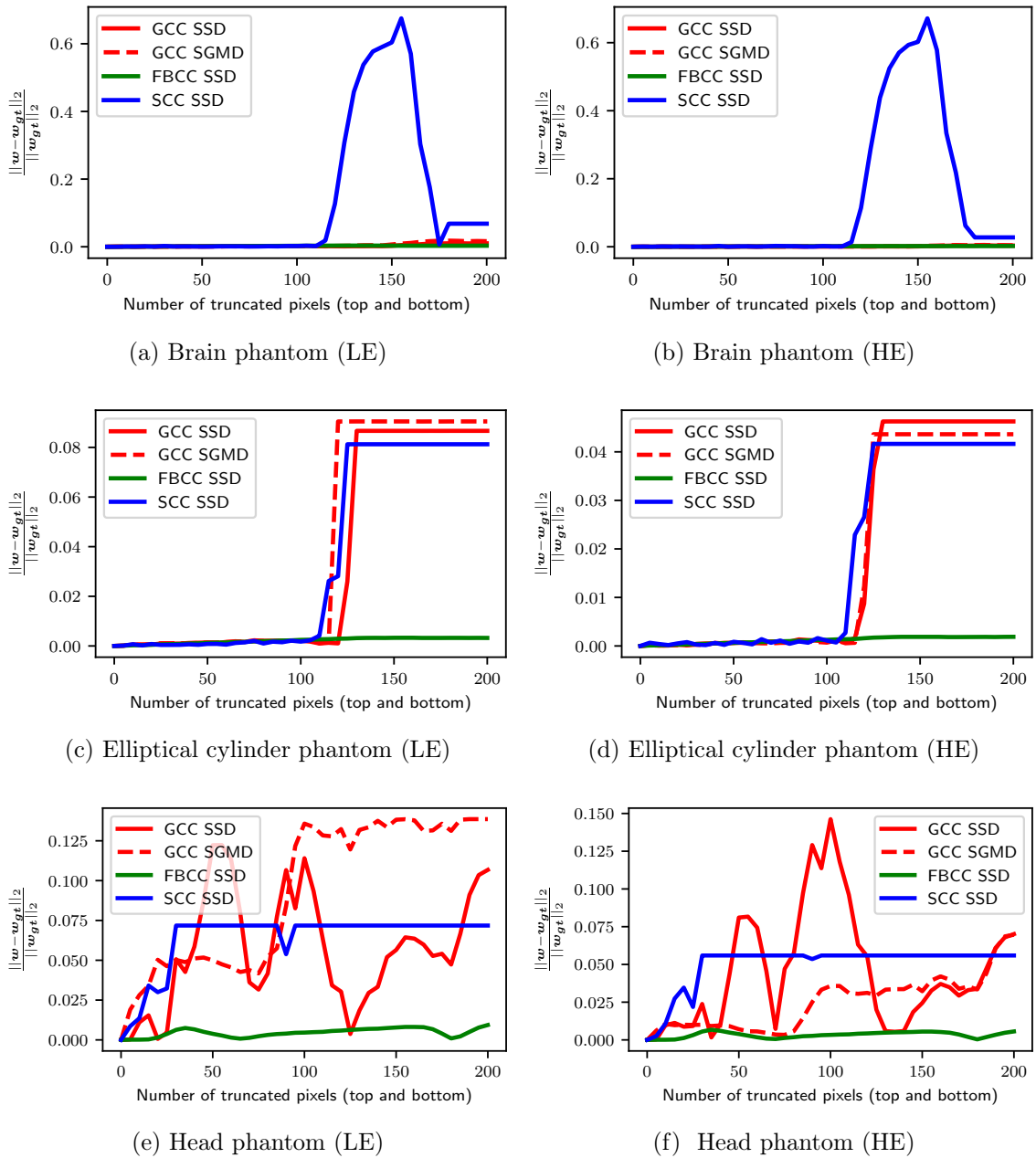
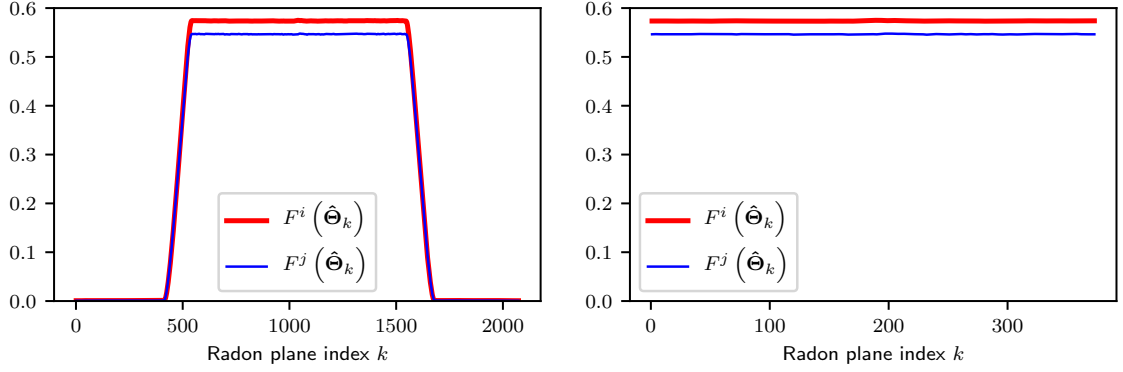
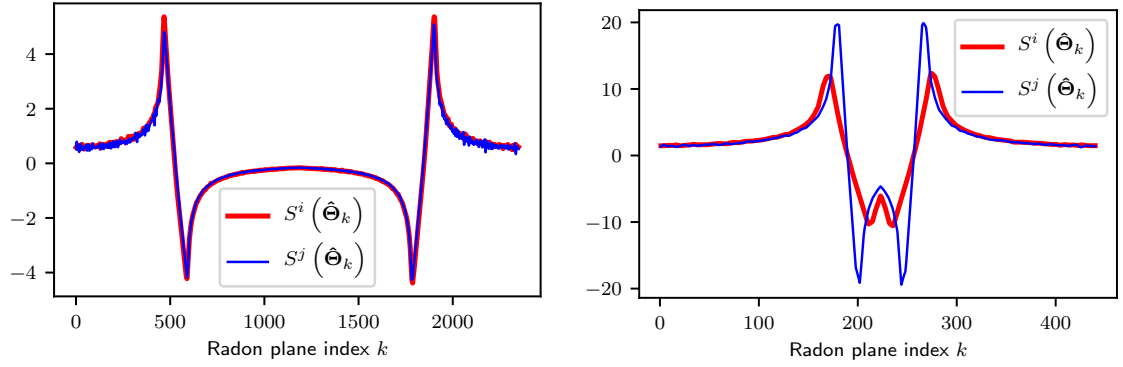


Figure 3.17: Robustness of algorithm (axial truncation).



(a) Fan beam intermediate functions computed from the ground-truth projections. (b) Fan beam intermediate functions computed from the axial truncated projections.



(c) Smith intermediate functions computed from the ground-truth projections. (d) Smith intermediate functions computed from the axial truncated projections.

Figure 3.18: Fan beam and Smith intermediate functions computed from the ground truth and truncated projections of the elliptical cylinder phantom (LE).

Projection offsets

CC-based methods are very robust, and the relative polynomial errors are very low when the projections are corrupted with a constant offset, as shown in Fig. 3.28. Fig. 3.29 demonstrates that the algorithms are sensitive to projections-specific offsets. The derivative and ramp filters enhance the robustness of GCC and SCC-based algorithms. FBCC-based correction is very sensitive to projection-specific offsets due to the lack of offset-canceling additional operations. We can also observe that the FBCC-based correction is less robust compared to others when constant offsets corrupt the projections. The robustness of SCC-based algorithms can be compromised by the addition of offsets to the background and the resultant truncation errors. Hence, GCC-based beam hardening correction is the clear choice for beam hardening correction if the projections are corrupted with the low-frequency offsets due to

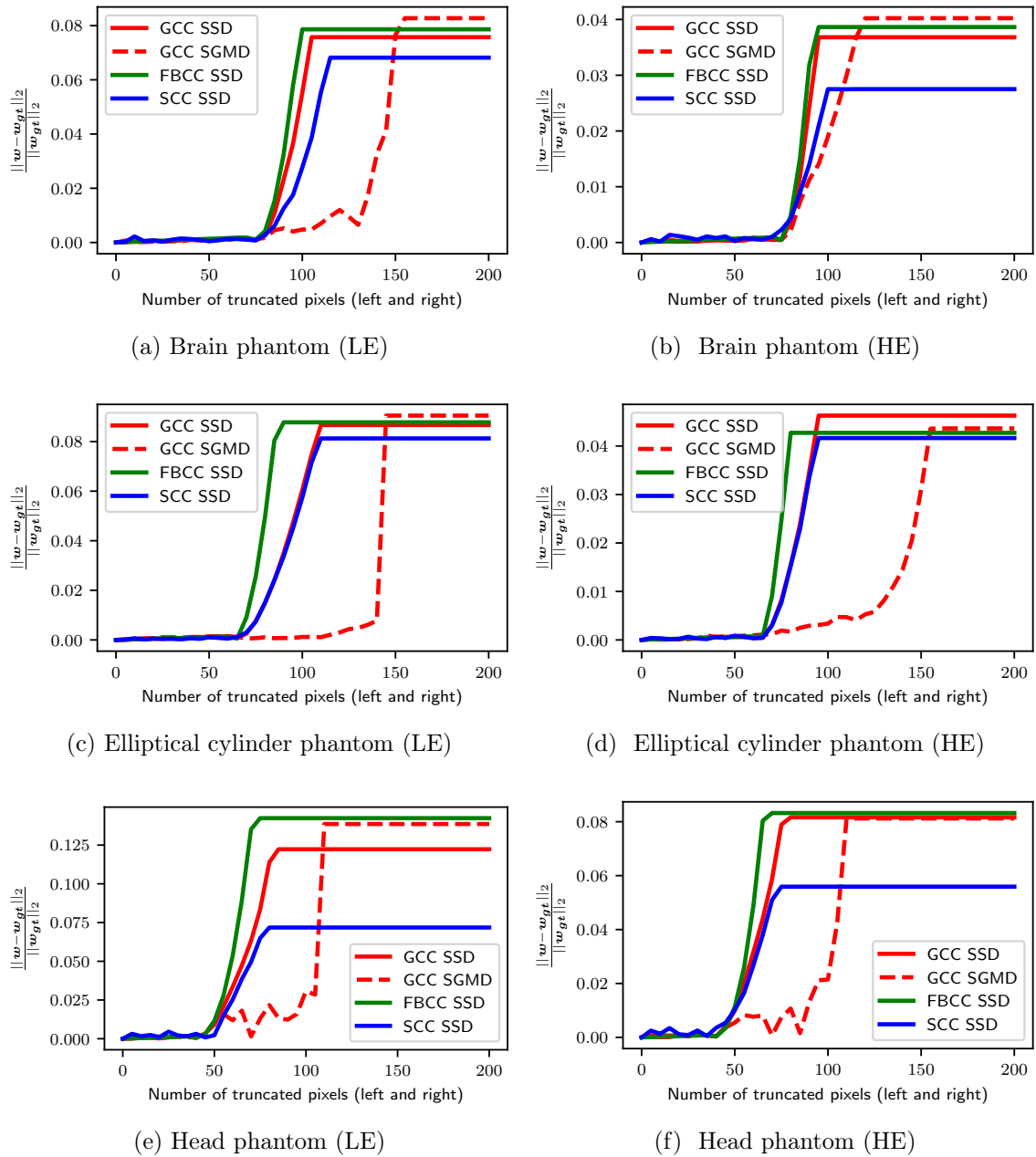


Figure 3.19: Robustness of algorithms (lateral truncation).

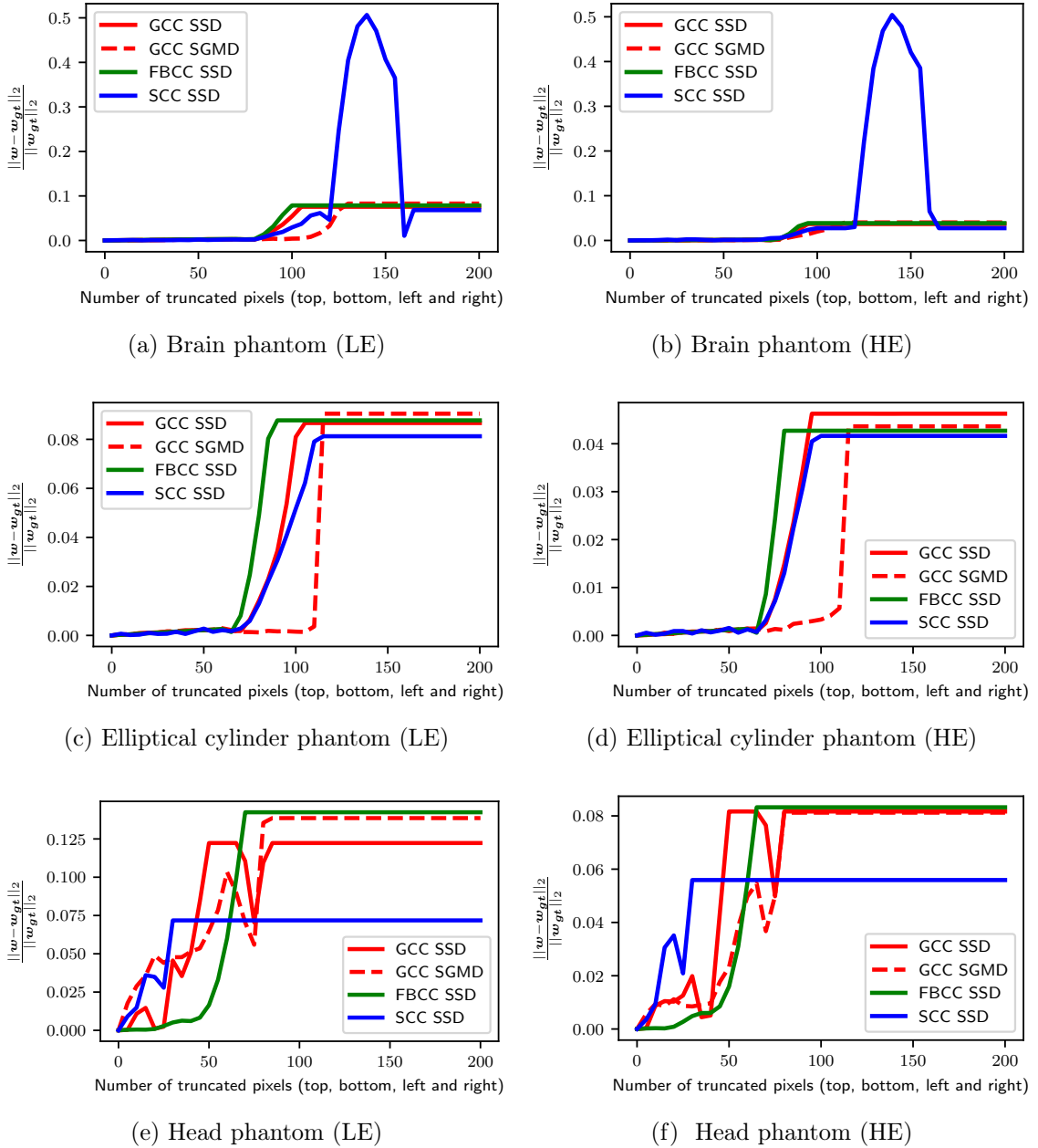


Figure 3.20: Robustness of algorithms under axial and lateral truncations.

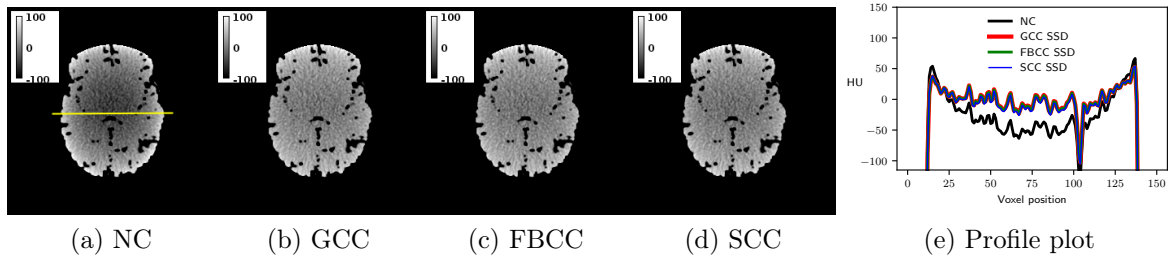


Figure 3.21: Beam hardening correction for the truncated projections where 85 pixels were cropped from all four sides of the projections: NC, reconstructed image without beam hardening correction; GCC, after GCC-based water correction; FBCC, after FBCC-based water correction; SCC, after SCC-based water correction.

sub-optimal projection pre-processing.

Scatter

Fig. 3.30 displays the plots of relative polynomial error for an increasing degree of scatter radiation in the projections. The experiments with the brain and head phantoms indicate the relative robustness of the FBCC-based algorithm towards scattering. However, the sensitivity of GCC and SCC demonstrate their effectiveness of reducing the cupping artifacts due to beam hardening and scatter. Since both phenomena underestimate the projection's attenuation values, the polynomial expressions reduce the artifacts by additive corrections irrespective of their origin. This over-correction is achieved by increasing the non-linearity of the second-degree polynomial. Fig. 3.31 shows the overcompensation by GCC and SCC-based algorithms yield stronger cupping reduction compared to the robust FBCC correction. There is no further image processing in most reconstruction pipelines to mitigate the cupping artifacts after projection linearization, and it often follows the software-based scatter correction algorithm [97] [84]. Hence, a strong correction by the GCC-based algorithm ensures the mitigation of residual scatter artifacts.

Compared to the brain and head phantoms, the increase of non-linearity of the polynomials for the correction of elliptical cylinder phantom images is modest for GCC and SCC-based algorithms. Besides, the decrease of w_2 results in inadequate cupping reduction after FBCC-based correction. *SPR* images of the homogeneous elliptical cylinder are analogous to projection-specific offsets making FBCC-based algorithms sensitive to scatter radiation if the imaged objects are homogeneous and symmetric.

The results of the comparative evaluations of consistency conditions are summarized in Table. 3.6. The robustness of the GCC-based algorithm can be improved by employing the SGMD dissimilarity measure if the projections are corrupted by noise,

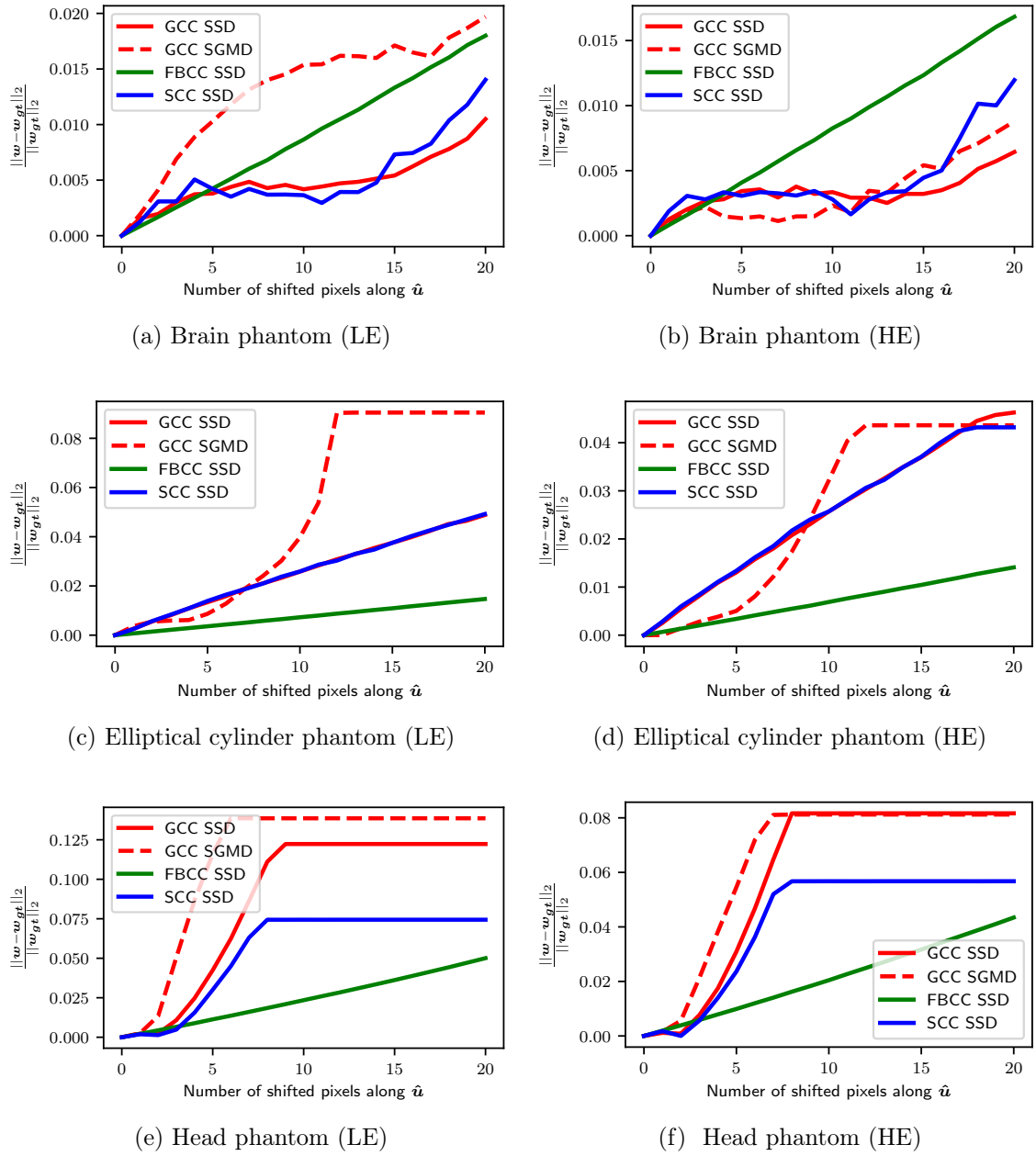


Figure 3.22: Robustness of algorithms under shifted detector along the \hat{u} (column) direction.

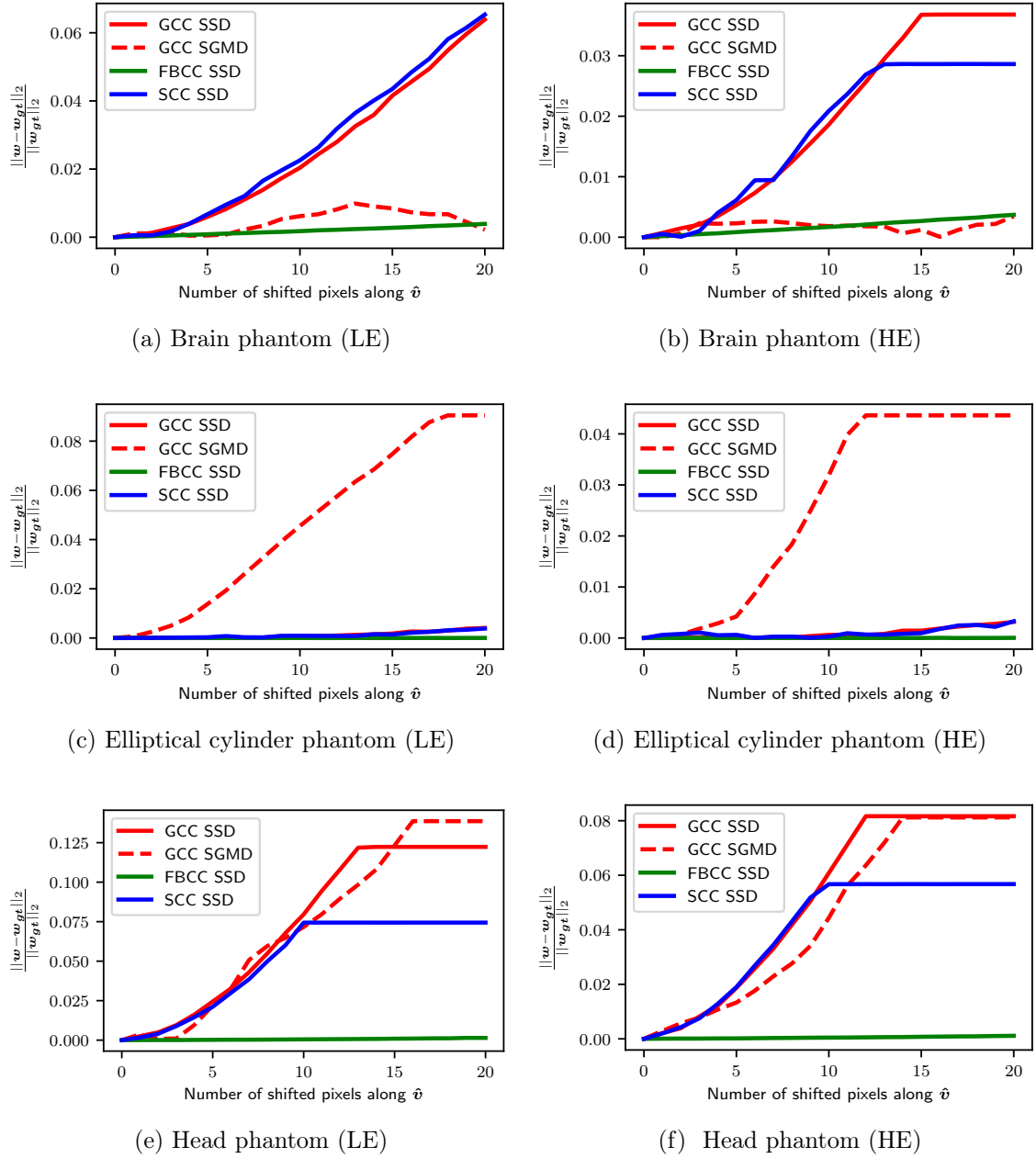
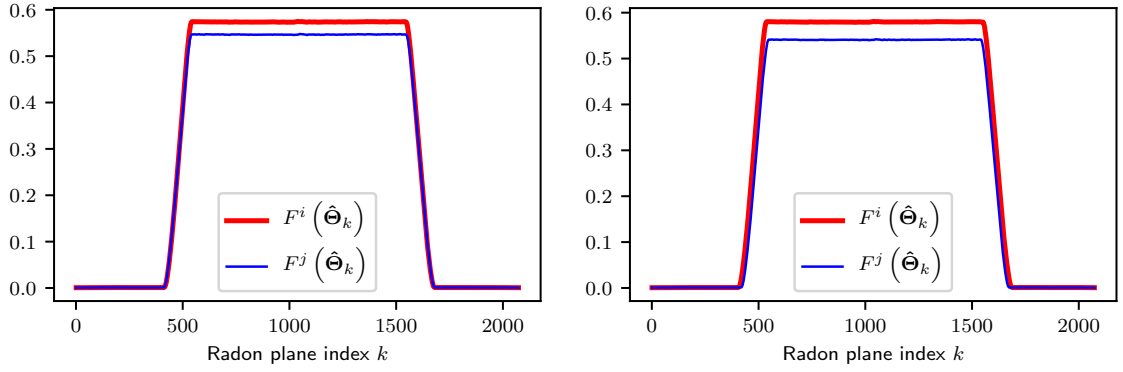
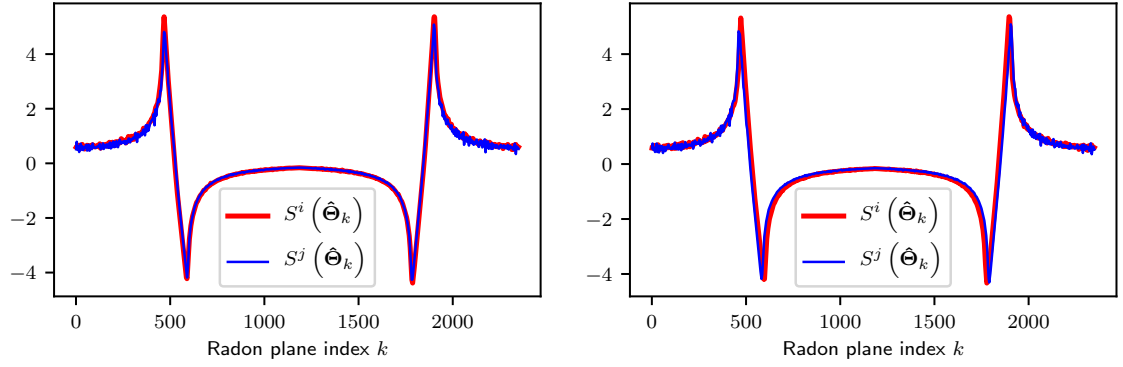


Figure 3.23: Robustness of algorithms under shifted detector along the $\hat{\theta}$ (row) direction.



(a) Fan beam intermediate functions computed from the ground-truth projections. (b) Fan beam intermediate functions computed from the shifted ($\hat{\mathbf{u}}$) projections.



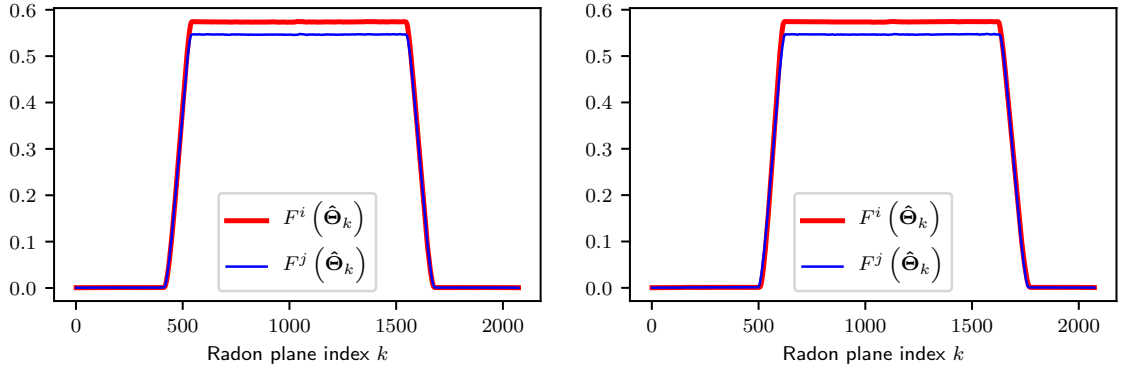
(c) Smith intermediate functions computed from the ground-truth projections. (d) Smith intermediate functions computed from the shifted ($\hat{\mathbf{u}}$) projections.

Figure 3.24: Fan beam and Smith intermediate functions computed from the ground truth and and shifted (along column) projections of elliptical cylinder phantom (LE).

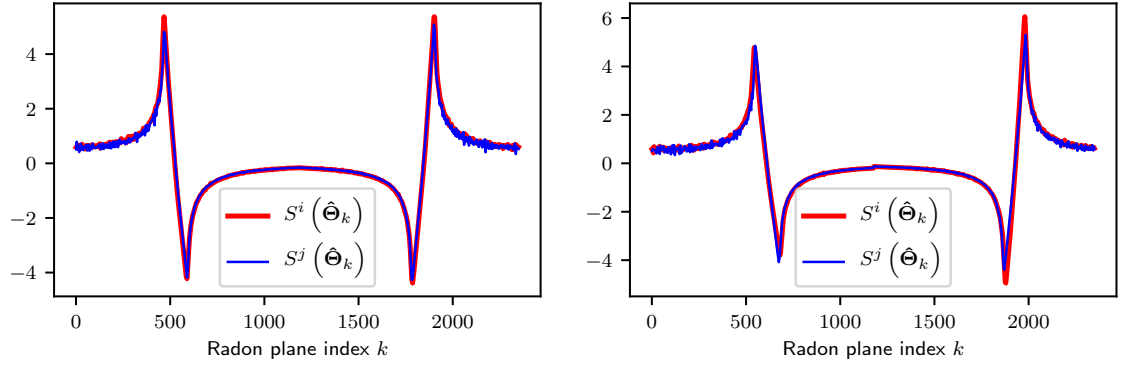
truncation and offsets. Besides, the free parameter of SGMD error metric σ (Eq. 3.17) can be heuristically determined to enhance the robustness towards a specific projection error. Similarly, SGMD can also be employed to improve the robustness of FBCC and SCC-based algorithms. We decided to refrain from calibrating the free parameter for a calibration-free beam hardening correction algorithm since the optimal parameter can vary according to the system geometry and the projection errors.

3.4.3 Real and Clinical Data

Fig. 3.32 displays the beam hardening corrections for the jaw specimen, where the projection data was acquired from a high precision micro-CT scanner. After minimiz-



(a) Fan beam intermediate functions computed from the ground truth projections. (b) Fan beam intermediate functions computed from the shifted (v) projections.



(c) Fan beam intermediate functions computed from the ground truth projections. (d) Fan beam intermediate functions computed from the shifted (v) projections.

Figure 3.25: Fan beam and smith intermediate functions computed from the ground truth and shifted (along row) projections of the elliptical cylinder phantom (LE).

ing the inconsistency measure (Fig. 3.33a), similar second-degree polynomials were estimated by the correction algorithms (Fig. 3.33b). The streak artifacts between teeth and bones are greatly reduced after CC-based corrections. We can observe the introduction of a small degree of bright streak artifacts due to over-corrections. However, the reduction of dark streak artifacts homogenizes the voxel values and significantly outweighs any introduction of artifacts.

Fig. 3.35 depicts beam hardening corrections for different clinical datasets. The cupping artifacts are significantly reduced after GCC-based corrections. The figures demonstrate the feasibility of GCC-based corrections when the projection data is corrupted with geometrical errors due to patient motion or miscalibration. We also observe that the over-correction by GCC-based algorithm reduces the cupping artifacts

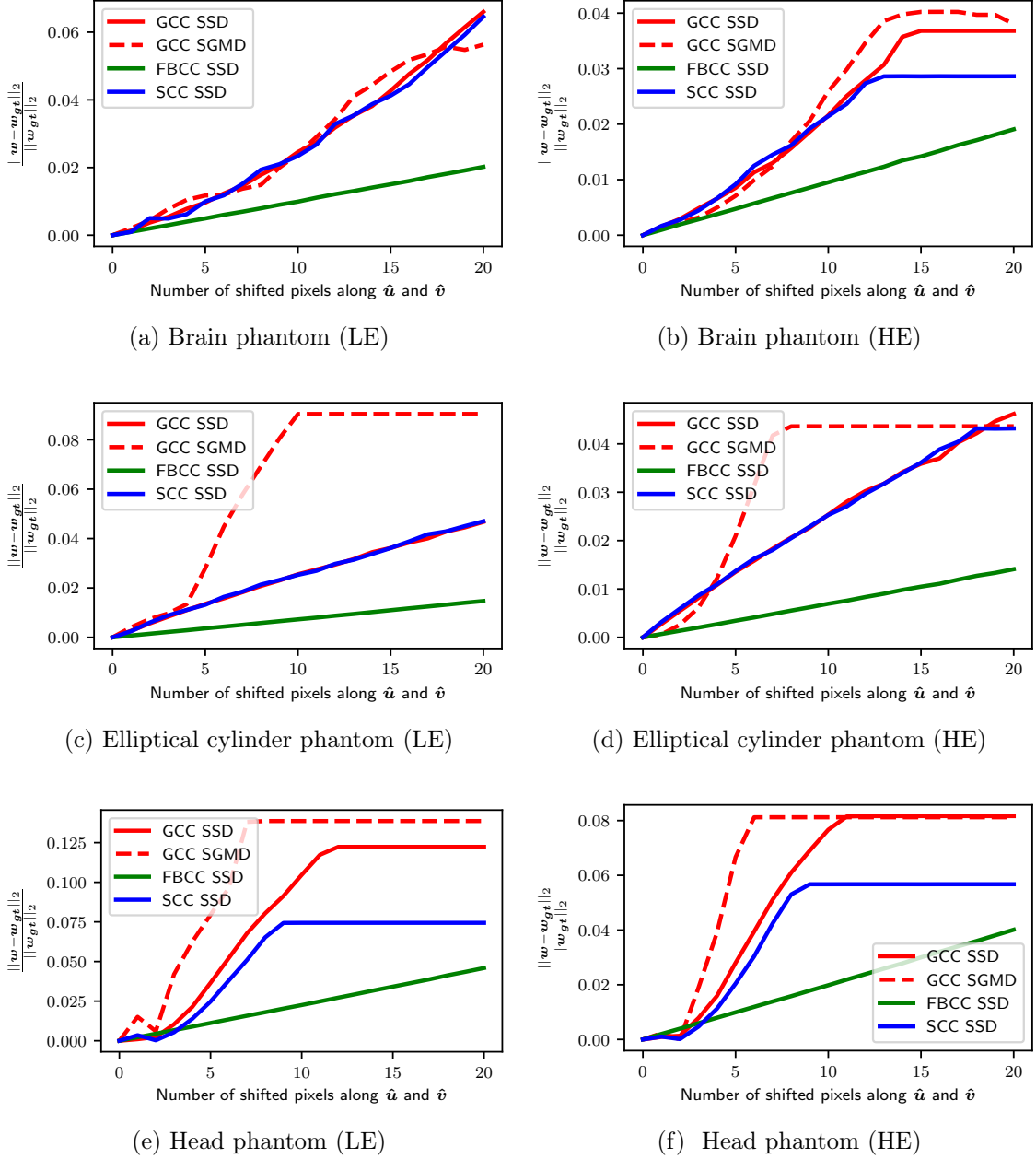


Figure 3.26: Robustness of algorithms under detector shift along the \hat{u} (column) and \hat{v} (row) directions.

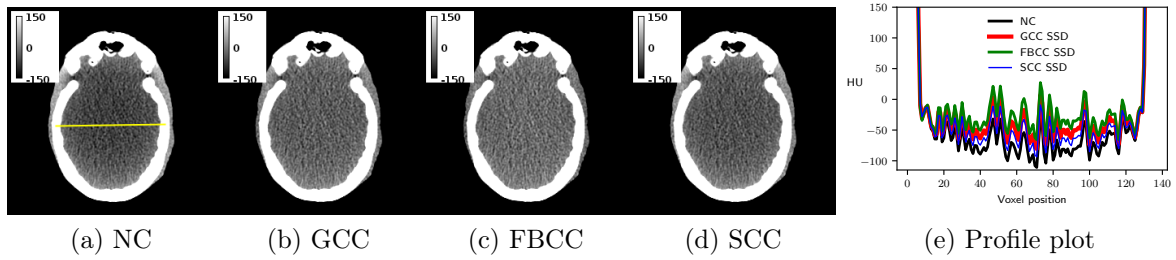


Figure 3.27: Beam hardening correction for the shifted projections (5 pixels along rows and columns): NC, reconstructed image without beam hardening correction; GCC, after GCC-based water correction; FBCC, after FBCC-based water correction; SCC, after SCC-based water correction.

Table 3.6: Summary of comparative evaluations of consistency conditions.

Criteria	GCC	SCC	FBCC
Computational efficiency	✓✓	✓	✓✓✓
Number of iterations for polynomial optimization	✓✓✓	✓✓✓	✓✓✓
Robustness (Poisson noise)	✓✓	✓	✓✓✓
Robustness (axial truncation)	✓✓	✓	✓✓✓
Robustness (lateral truncation)	✓	✓	✓
Robustness (axial + lateral truncation)	✓	✓	✓
Robustness (constant offset)	✓✓✓	✓✓	✓
Robustness (projection specific offset)	✓✓✓	✓✓	✓
Robustness (scatter)	✓	✓	✓✓
Robustness (detector shift)	✓✓	✓	✓✓✓

significantly compared to the scanner built-in water correction. Since the optimization algorithms could not minimize FBCC and SCC-based inconsistency measures (Fig. 3.34), the projection linearizations were performed with the identity function, and the corrected images are equivalent to NC images. It is difficult to find the exact reason for the poor performance of both corrections due to the lack of knowledge of many proprietary pre-processing algorithms prior to water correction. Based on the robustness studies, the inability to minimize FBCC and SCC-based inconsistency measures could be attributed to the presence of projection-specific offsets and truncation artifacts. We can find that the decrease of inconsistency measure is significantly low for clinical data compared to the projections from the industrial CT scanner. This is mainly due to the geometrical errors and detector imperfections (ring artifacts), and the artifacts caused by them are visible in the clinical images.

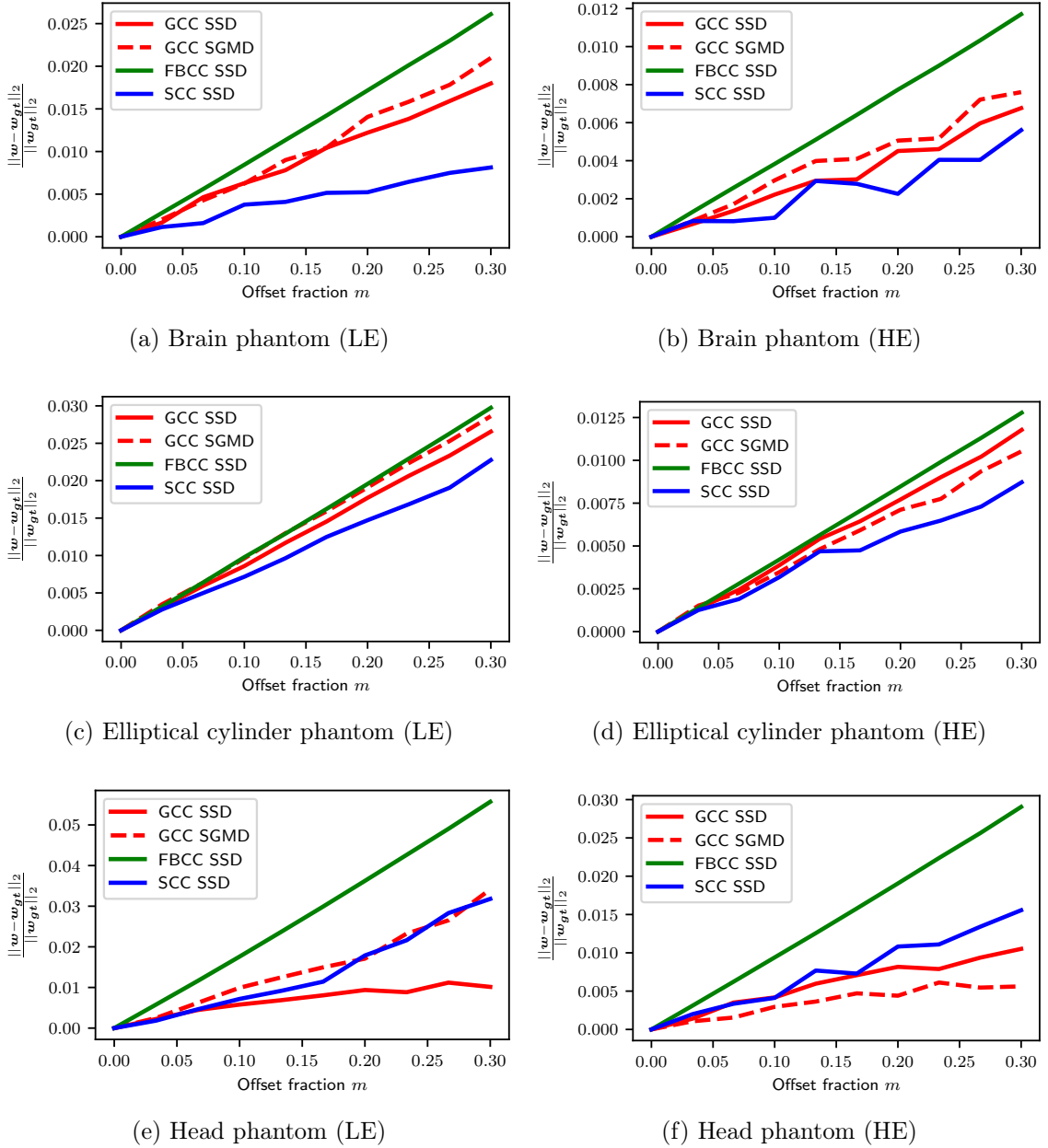


Figure 3.28: Robustness of algorithms when the projections are corrupted with a constant offset.

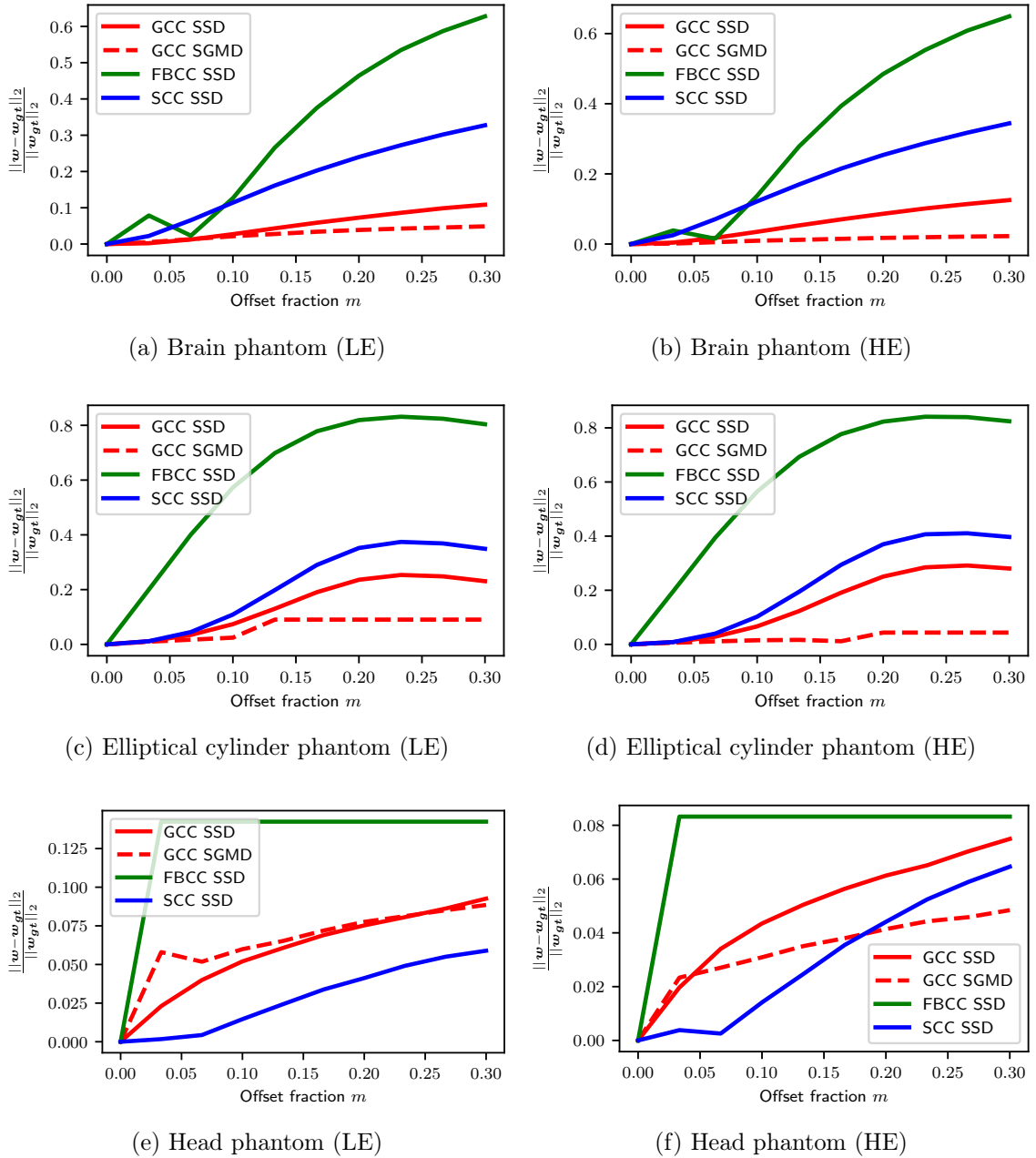


Figure 3.29: Robustness of algorithm when the projections are corrupted with projection-specific offset.

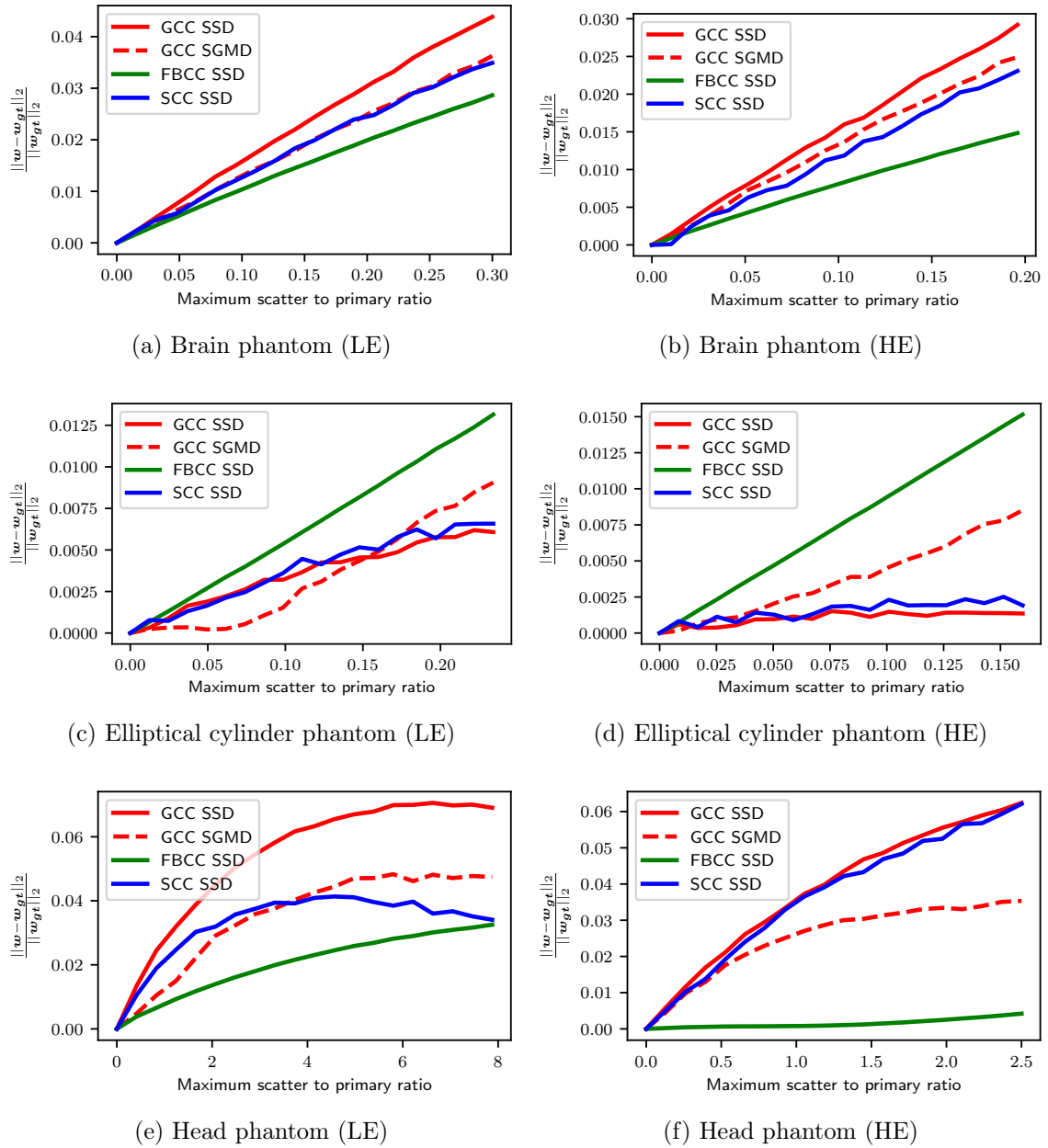


Figure 3.30: Robustness of algorithm when the projections are corrupted by scatter radiation.

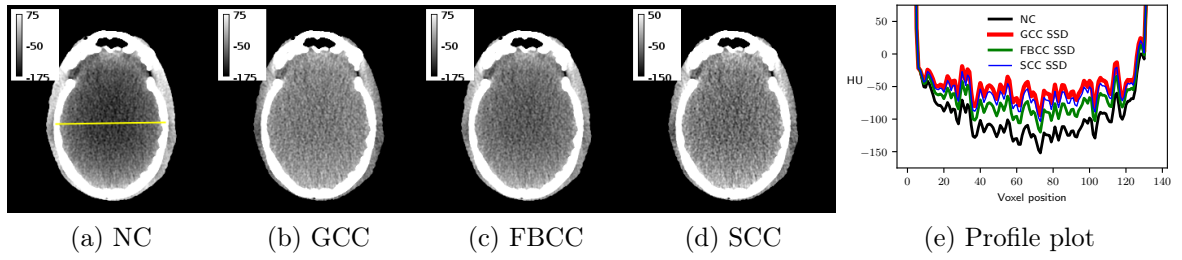


Figure 3.31: Beam hardening correction for the head phantom. The polychromatic (HE) projections were corrupted with scatter radiation where maximum $\text{SPR} = 2.5$: NC, reconstructed image without beam hardening correction; GCC, GCC-based water correction; FBCC, FBCC-based water correction; SCC, SCC-based water correction.

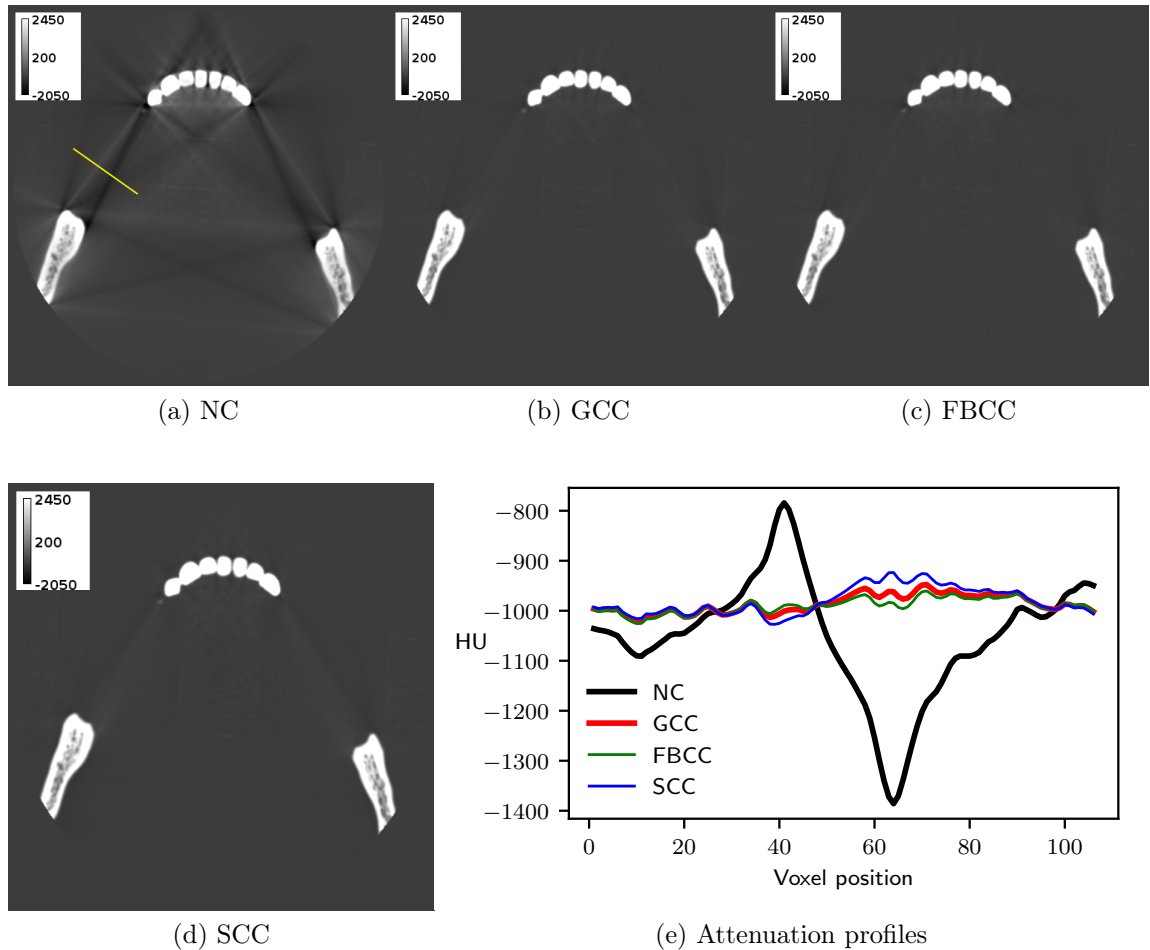
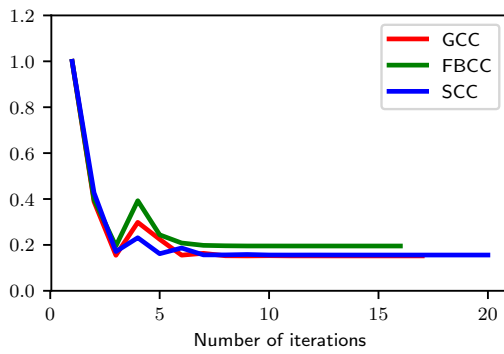
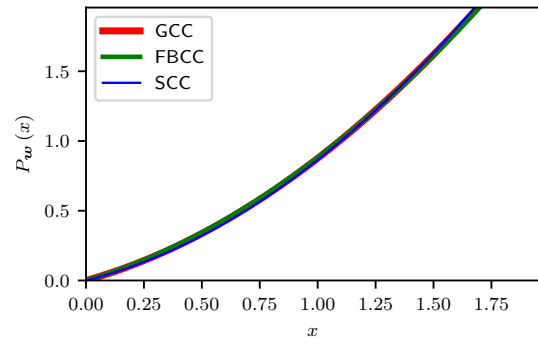


Figure 3.32: Beam hardening correction for micro-CT data. Images courtesy of Fraunhofer IPK, Berlin, Germany.

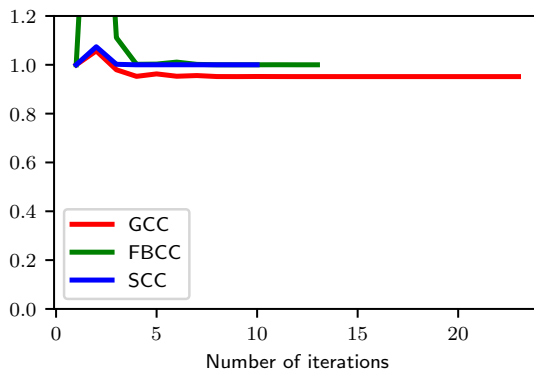


(a) The convergence of normalized inconsistency measure

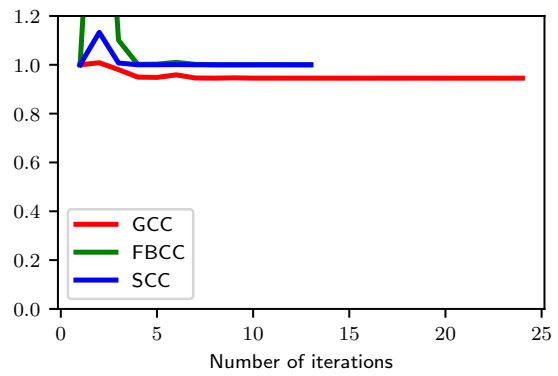


(b) The optimized polynomials

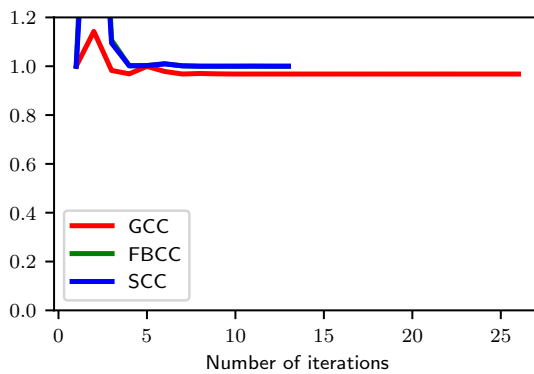
Figure 3.33: The optimization of correction polynomials (micro-CT).



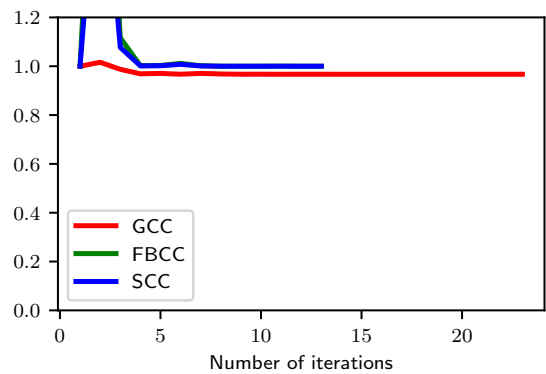
(a) Patient 1



(b) Patient 2



(c) Patient 3



(d) Patient 4

Figure 3.34: The minimization of normalized inconsistency measure (clinical data).

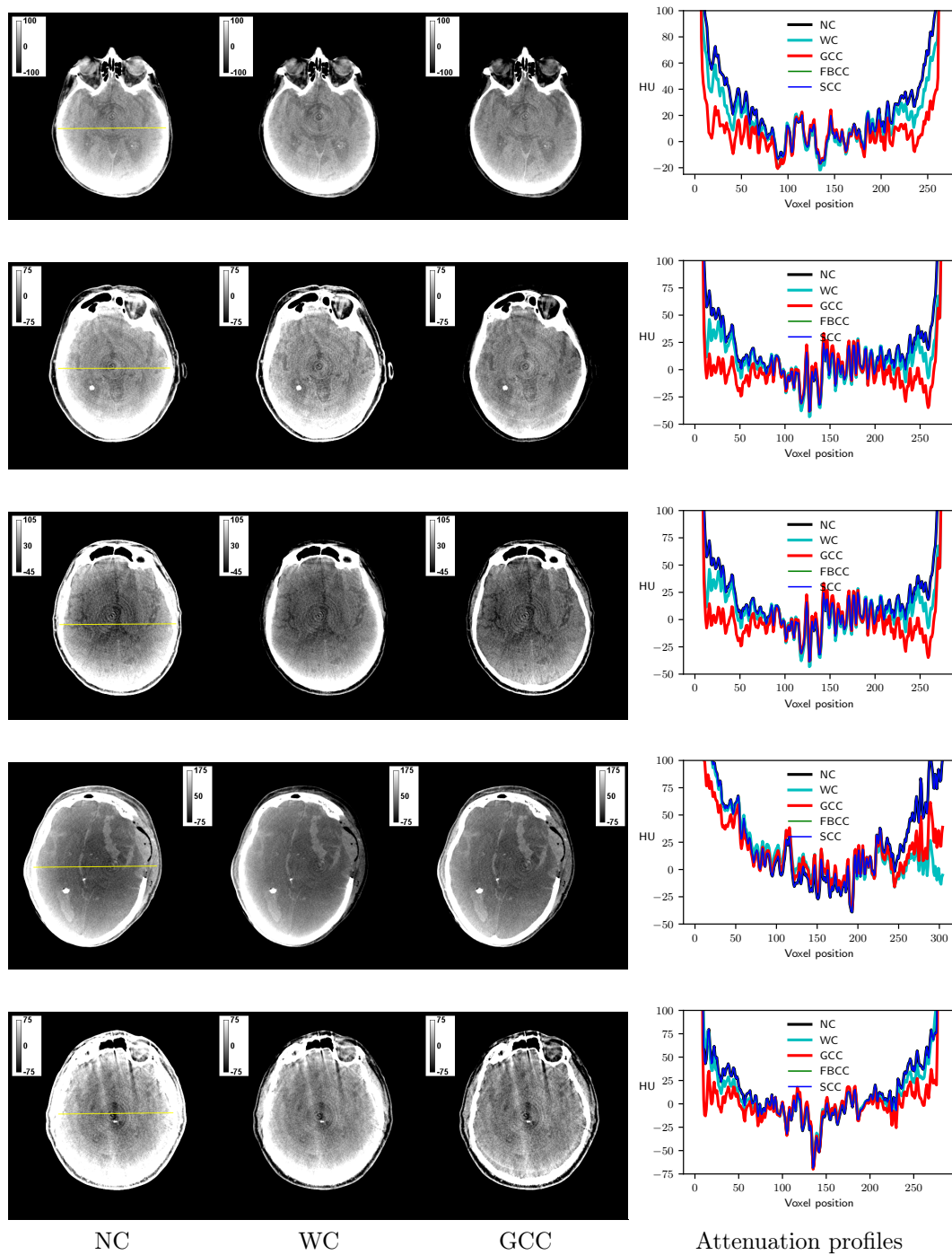


Figure 3.35: Beam hardening correction for C-arm CBCT head scans: NC, reconstructed image without beam hardening correction; WC, after scanner built-in water correction; GCC, after GCC-based water correction. Images courtesy of University Hospital, Magdeburg, Germany.

4 Beam Hardening Correction for Multi-material Objects

4.1 Introduction

The higher-order beam hardening artifacts due to polychromatic attenuation by strongly attenuating structures like bones or metals can be corrected using IBHC, EBHC, and BHFC algorithms (Sec. 2.7.1). The methods rely on the forward projections of segmented bone volume to estimate the residual error caused by polychromatic X-ray attenuation by bones which cannot be corrected by sole water correction. The algorithms differ on the parameterized models employed to compute artifact-free projections. Hsieh et al. proposed to estimate the bone correction polynomial \mathbf{b}' for IBHC using the prior knowledge about X-ray and material attenuation spectra or by the calibration experiments [49]. Calibration-free IBHC, EBHC, and BHFC involve the determination of model parameters in volume/object space by minimizing the high-frequency streak artifacts of the corrected volume iteratively [61] [58] [73]. BHFC is computationally very expensive due to the requirement of back projection operation during each iteration. By contrast, EBHC volume can be expressed as the linear combination of three monomial volumes, and they can be pre-computed before the optimization of polynomial coefficients. Hence, back projection operations are not necessary during EBHC iterations.

As in CC-based water correction, the coefficients for higher-order corrections can be estimated by enforcing consistency conditions on cone beam projection pairs. Consistency conditions enable us to determine the IBHC correction polynomial without calibration or prior knowledge. By estimating the BHFC coefficient directly from the projections using CC, the requirement of back projection operations during each iteration is eliminated. Instead of TV, CC-based EBHC reduces the number of required reconstructions from 3 to 2. Moreover, all TV-based higher-order beam hardening corrections are sensitive to image noise due to their reliance on gradient images to quantify high-frequency streak artifacts. By employing CC, a noise-tolerant beam hardening correction algorithm can be formulated.

4.2 Method

The workflow of a multi-pass algorithm to correct both water- and bone-induced beam hardening artifacts is depicted in Fig. 4.2. In the first pass of the algorithm, water

correction is performed after optimizing the polynomial using consistency conditions. During the second pass, the prior volume μ_w is reconstructed from the water corrected projections. 3-level Otsu's method is used to compute threshold values HU_a , HU_w and HU_b (in Hounsfield scale) to segment air, water, and bone from μ_w . Instead of a simple thresholding operation, the segmentation is performed according to the Elbakri-Fessler displacement model to eliminate the sharp transition [35] [42]. By assuming the volume consists of voxels representing water, bone, and water-bone mixture, the bone fraction volume f_b (Fig. 4.1) is computed as:

$$f_b(\mathbf{x}) = \begin{cases} 0.0, & \text{if } HU(\mathbf{x}) < HU_w \\ \frac{1 + \sin\left[\frac{W(HU(\mathbf{x}) - HU_w) - \frac{\pi}{2}}{2}\right]}{2}, & \text{if } HU_w \leq HU(\mathbf{x}) \leq HU_b \\ 1.00 & \text{if } HU(\mathbf{x}) > HU_b \end{cases} \quad (4.1)$$

$$W = \frac{\pi}{HU_b - HU_w}$$

$$HU(\mathbf{x}) = \frac{\mu_w(\mathbf{x}) - \mu_{water}}{\mu_{water}}$$

The volume containing only high attenuation bone structures is computed by:

$$\mu_b(\mathbf{x}) = f_b(\mathbf{x}) \mu_w(\mathbf{x}) \quad (4.2)$$

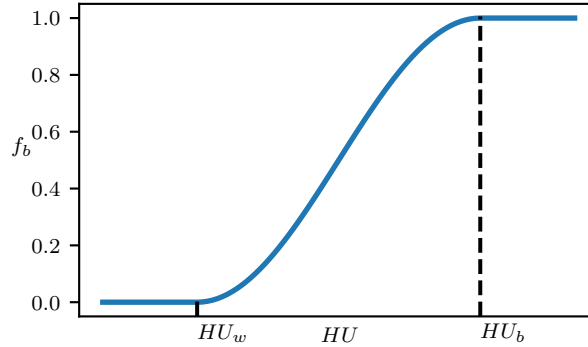


Figure 4.1: Bone fraction when $HU_w = 200$ HU and $HU_b = 800$ HU.

The rest of the steps vary according to the parametric model employed to estimate bone corrected projections.

4.2.1 CC-based IBHC

In the second-order IBHC, bone corrected projections $g_w^{b^t}$ are estimated using the water corrected projections g_w , forward projections of bone volume $\mathcal{X}_3\mu_b$ and the polynomials for water w and bone corrections $\mathbf{b}^t = [b_0^t = 0, b_1^t, b_2^t]^T$ (Eq. 2.101).

$$g_w^{b^t} = g_w + (b_1^t - w_1) \mathcal{X}_3\mu_b + (b_2^t - w_2) [\mathcal{X}_3\mu_b]^2 \quad (4.3)$$

Since the projections are already water corrected and the bone correction polynomial coefficients are unknown, we can use the identity function as water correction polynomial $\mathbf{w} = [w_0 = 0, w_1 = 1, w_2 = 0]^T$.

$$g_{\mathbf{b}^\nu} = g_{\mathbf{w}}^{\mathbf{b}^\nu} = g_{\mathbf{w}} + (b_1^\nu - 1) \mathcal{X}_{3\mu_b} + b_2^\nu [\mathcal{X}_{3\mu_b}]^2 \quad (4.4)$$

The quantified inconsistency computed from a pair of bone corrected projections is given by:

$$\mathcal{E}^{ij}(\mathbf{b}^\nu) = \sum_{k=0}^{K-1} \left[G^i, S^i \text{ or } F^i(\hat{\Theta}_k; \mathbf{b}^\nu) - G^j, S^j \text{ or } F^j(\hat{\Theta}_k; \mathbf{b}^\nu) \right]^2 \quad (4.5)$$

$$\begin{aligned} G^i(\hat{\Theta}_k; \mathbf{b}^\nu) &= G(s_k^i, \theta_k^i; \mathbf{b}^\nu) \\ &= \frac{(s_k^i)^2 + (D^i)^2}{(D^i)^2} \frac{\partial}{\partial s_k^i} \mathcal{R}_2 g_{\mathbf{b}^\nu}^c(\theta_k^i, s_k^i) \end{aligned} \quad (4.6)$$

$$\begin{aligned} S^i(\hat{\Theta}_k; \mathbf{b}^\nu) &= S(s_k^i, \theta_k^i; \mathbf{b}^\nu) \\ &= \frac{(s_k^i)^2 + (D^i)^2}{(D^i)^2} h_r(s_k^i) * \mathcal{R}_2 g_{\mathbf{b}^\nu}^c(\theta_k^i, s_k^i) \end{aligned} \quad (4.7)$$

$$\begin{aligned} F^i(\hat{\Theta}_k; \mathbf{b}^\nu) &= F(s_k^i, \theta_k^i; \mathbf{b}^\nu) \\ &= \frac{-1}{\langle \hat{\mathbf{w}}(\alpha_i), \frac{\mathbf{f}(\alpha_i) - \mathbf{f}(\alpha_j)}{\|\mathbf{f}(\alpha_i) - \mathbf{f}(\alpha_j)\|_2} \rangle} \mathcal{R}_2 g_{\mathbf{b}^\nu}^{c,d}(\theta_k^i, s_k^i) \end{aligned} \quad (4.8)$$

Similar to CC-based water correction, the bone correction polynomial is estimated by minimizing the quantified inconsistency:

$$\begin{aligned} \min_{\mathbf{b}^\nu} \frac{\sum_i \sum_j \mathcal{E}^{ij}(\mathbf{b}^\nu)}{\sum_i \sum_j \mathcal{E}^{ij}(\mathbf{b}_0^\nu)} \text{ where } \langle \mathbf{f}(\alpha_i), \mathbf{f}(\alpha_j) \rangle \rightarrow 0 \\ \text{s.t. } \int_0^{\max\{\mathcal{X}_{3\mu_b}\}} p_{\mathbf{b}^\nu}(x) dx = \frac{(\max\{\mathcal{X}_{3\mu_b}\})^2}{2} \end{aligned} \quad (4.9)$$

The rationale behind the choice of orthogonal projection pairs and the need for the normalization of inconsistency measure are explained in Sec. 3.2. Initial parameter $\mathbf{b}_0^\nu = [b_0^\nu = 0, b_1^\nu = 1, b_2^\nu = 0]^T$ is set to identity function. Hence, the normalized inconsistency measure is 1 during the first iteration.

The constraint ensures constant area under the polynomial, determined by the robust maximum value of forward projections $\max\{\mathcal{X}_3\mu_b\}$. It is to be noted that the constraint is not necessary for the optimization of bone correction polynomial. In CC-based water correction, the polynomial transforms all the pixel values of uncorrected projections. Therefore, the global minimum can be reached with the trivial solution of zero polynomial. By contrast, \mathbf{b}^e acts only on the bone forward projections, and only the bone overlapped ROIs of the water corrected projections are modified during the minimization of inconsistency measure. However, the constraint accelerates the polynomial optimization and makes the algorithm robust when the projections are corrupted with other artifacts. Since the second-order polynomial is used for corrections, the efficient implementation of the above minimization can be formulated by following the equations described in Sec. 3.2:

$$\begin{aligned} \min_{b_2'} & \frac{\sum_i \sum_j \mathcal{E}^{ij}(b_2')}{\sum_i \sum_j \mathcal{E}^{ij}(b_2' = 0)} \text{ where } \langle \mathbf{f}(\alpha_i), \mathbf{f}(\alpha_j) \rangle \rightarrow 0 \\ \text{s.t. } & 0 \leq b_2' \leq \frac{3}{2\max\{\mathcal{X}_3\mu_b\}} \\ & \text{where } b_1' = 1 - \frac{2}{3}b_2'\max\{\mathcal{X}_3\mu_b\} \end{aligned} \quad (4.10)$$

4.2.2 CC-based EBHC

As per EBHC, the bone corrected projections $g_w^{b^e}$ are formulated as the bi-variate polynomial expression of g_w , $\mathcal{X}_3\mu_b$ and the coefficients $\mathbf{b}^e = [b_1^e, b_2^e, b_3^e]^T$ (Eq. 2.102).

$$g_w^{b^e} = g_w + (b_1^e - 1) \mathcal{X}_3\mu_b + b_2^e [\mathcal{X}_3\mu_b]^2 + b_3^e \mathcal{X}_3\mu_b g_w \quad (4.11)$$

Compared to IBHC, EBHC polynomial expression has an additional coefficient b_3^e to weight the product of water corrected and bone forward projections. The quantified inconsistency parameterized by EBHC polynomial \mathbf{b}^e is given as:

$$\mathcal{E}^{ij}(\mathbf{b}^e) = \sum_{k=0}^{K-1} \left[G^i, S^i \text{ or } F^i(\hat{\Theta}_k; \mathbf{b}^e) - G^j, S^j \text{ or } F^j(\hat{\Theta}_k; \mathbf{b}^e) \right]^2 \quad (4.12)$$

The three polynomial coefficients can be estimated by solving the following optimization problem [11]:

$$\min_{\mathbf{b}^e} \frac{\sum_i \sum_j \mathcal{E}^{ij}(\mathbf{b}^e)}{\sum_i \sum_j \mathcal{E}^{ij}(\mathbf{b}_0^e)} \text{ where } \langle \mathbf{f}(\alpha_i), \mathbf{f}(\alpha_j) \rangle \rightarrow 0 \quad (4.13)$$

The initial parameter \mathbf{b}_0^e is set to $[b_1^e = 1, b_2^e = 0, b_3^e = 0]^T$.

Table 4.1: NLOPT optimization parameters (bone corrections). The default values were used for all the parameters which are not listed here.

Parameter	value
Algorithm	COBYLA
Number of optimization variables	1(BHFC), 1(IBHC), 3(EBHC)
Lower bound	0 (IBHC, BHFC)
Upper bound	$\frac{3}{2max\{\mathcal{X}_3\mu_b\}}$ (IBHC)
Absolute tolerance on the function value	1e-4
Absolute tolerances on optimization parameters	1e-4

4.2.3 CC-based BHFC

The bone corrected projections can also be computed by the addition of Beam Hardening Factor (BHF):

$$g_w^{bf} = g_w + \Delta g_w^{bf} \quad (4.14)$$

where BHF parameterized by the coefficient b^f is estimated with the path length through the bone volume $\mathcal{X}_3 f_b$.

$$\Delta g_w^{bf} = \begin{cases} 0 & b^f \mathcal{X}_3 f_b = 0 \\ \ln \left(\frac{\sinh(b^f \mathcal{X}_3 f_b)}{b^f \mathcal{X}_3 f_b} \right) & b^f \mathcal{X}_3 f_b \neq 0 \end{cases} \quad (4.15)$$

Similarly, BHFC projection's inconsistency is quantified by:

$$\mathcal{E}^{ij}(b^f) = \sum_{k=0}^{K-1} \left[G^i, S^i \text{ or } F^i \left(\hat{\Theta}_k; b^f \right) - G^j, S^j \text{ or } F^j \left(\hat{\Theta}_k; b^f \right) \right]^2 \quad (4.16)$$

The free parameter of BHF is estimated as [15]:

$$\begin{aligned} \min_{b^f} \frac{\sum_i \sum_j \mathcal{E}^{ij}(b^f)}{\sum_i \sum_j \mathcal{E}^{ij}(b^f = 0)} \text{ where } \langle \mathbf{f}(\alpha_i), \mathbf{f}(\alpha_j) \rangle \rightarrow 0 \\ \text{s.t. } 0 \leq b^f \end{aligned} \quad (4.17)$$

Since BHF is an even function (Fig. 2.11b), the non-negative constraint limits the feasible region and thereby accelerates the minimization.

The optimization parameters for bone corrections are listed in Table. 4.1.

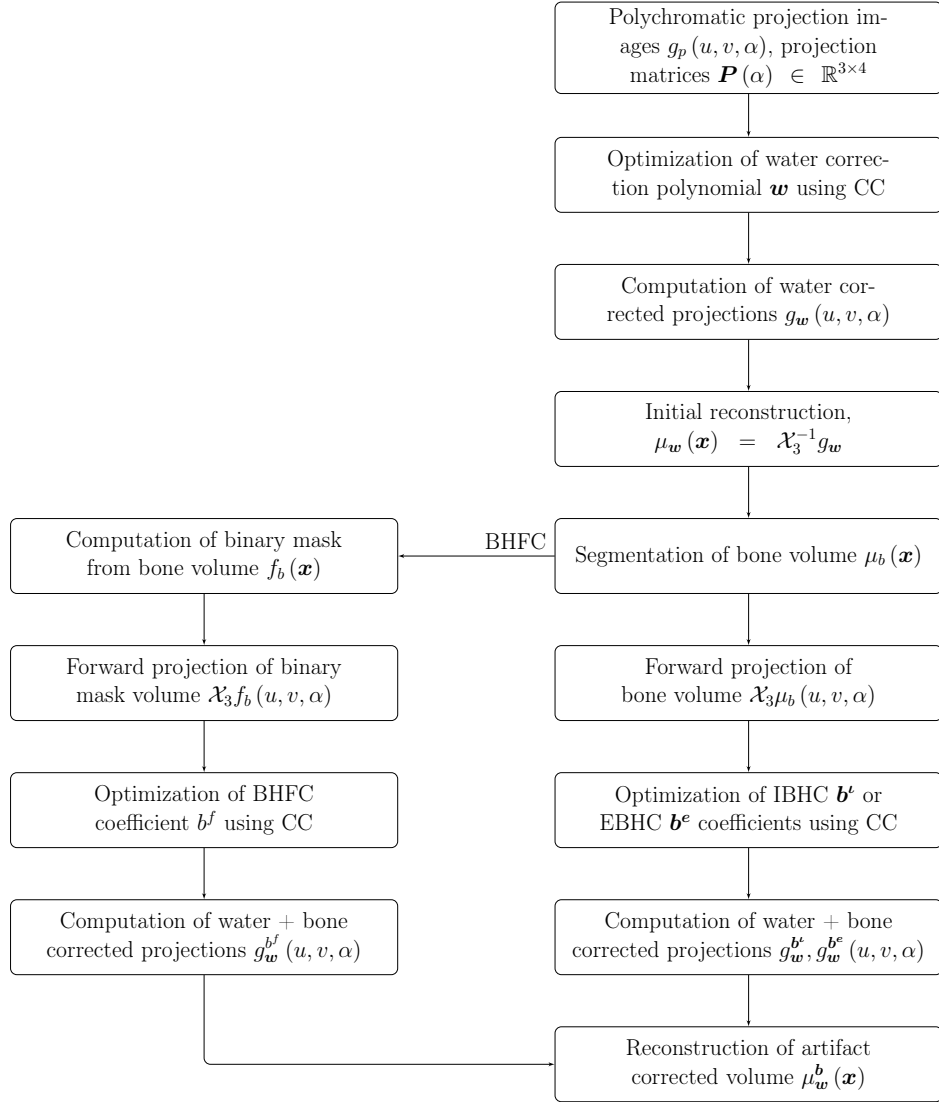


Figure 4.2: The workflow of the multi-pass algorithm for the first and higher-order corrections.

4.3 Experiments

To assess the efficacy of bone beam hardening corrections, the polychromatic projections were generated from the bi-material head and jaw phantoms [92] [65] consisting of water and bones. The same system geometry and spectrum simulation parameters described in Sec. 3.3.1 were used for projection generation. The robust coefficients of variation C_v^r (Eq. 3.19) of the voxels of selected ROIs (Fig. 4.3) were computed for quantitative evaluation. The C_v^r s corresponding to the elliptical and rectangular ROIs quantify the spill-over and streak artifacts, respectively. The algorithms were also validated with the clinical data from an interventional C-arm CBCT scan-

ner. The images were reconstructed after IBHC, EBHC, and BHFC corrections using GCC, FBCC, and SCC.

To demonstrate the effectiveness of algorithms to reduce higher-order artifacts due to beam hardening by metal implants, CC-based corrections were performed on a clinical dataset acquired by a mobile C-arm CBCT scanner. Four hundred projections at 110 keV were acquired over a short scan angular range of 199 degrees, where each projection contains 976x976 isotropic pixels of size 0.305 mm. The volumes were reconstructed on a 512x512x200 grid of isotropic voxels of 0.3 mm using FDK algorithm.

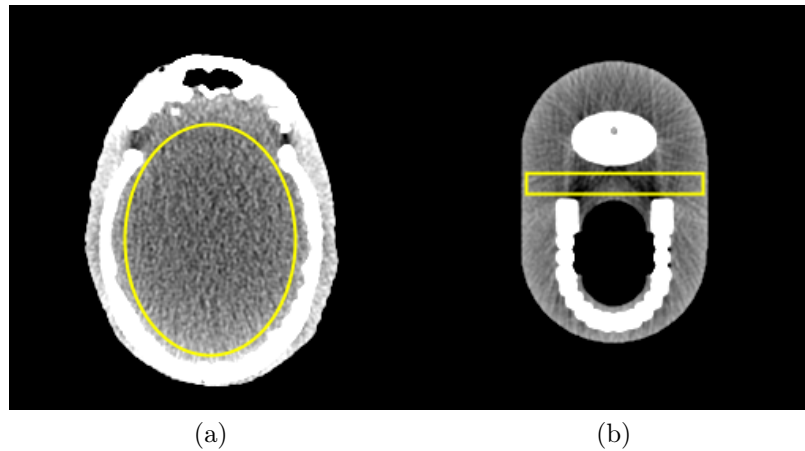


Figure 4.3: ROIs to compute the robust coefficient of variation.

4.4 Results and Discussion

4.4.1 Simulation

Fig. 4.4 and Fig. 4.5 display the results after beam hardening corrections for the head phantom. Compared to only water correction (WC), the additional bone corrections reduce the spill-over artifacts and recover the sharp bone-water boundaries. The dark streak artifacts (marked by the yellow arrow in Fig. 4.4b) between bone structures are also reduced after bone corrections. Tab. 4.2 confirms the improvement of uniformity of voxel values as evidenced by the decrease in C_v^r .

Fig. 4.4 and Fig. 4.5 show the artifacts reduction for the jaw phantom images. The streak artifacts between bone structures are greatly reduced after higher-order corrections. Due to the partial volume effect and inaccurate segmentation of bone structures, the forward projections of the bone volume can be overestimated near the edges of bone structures. As a result, the algorithms may perform over-corrections and generate bright streak artifacts. However, the reduction of dark streaks outweighs the introduction of artifacts, and the higher-order corrections improve overall image

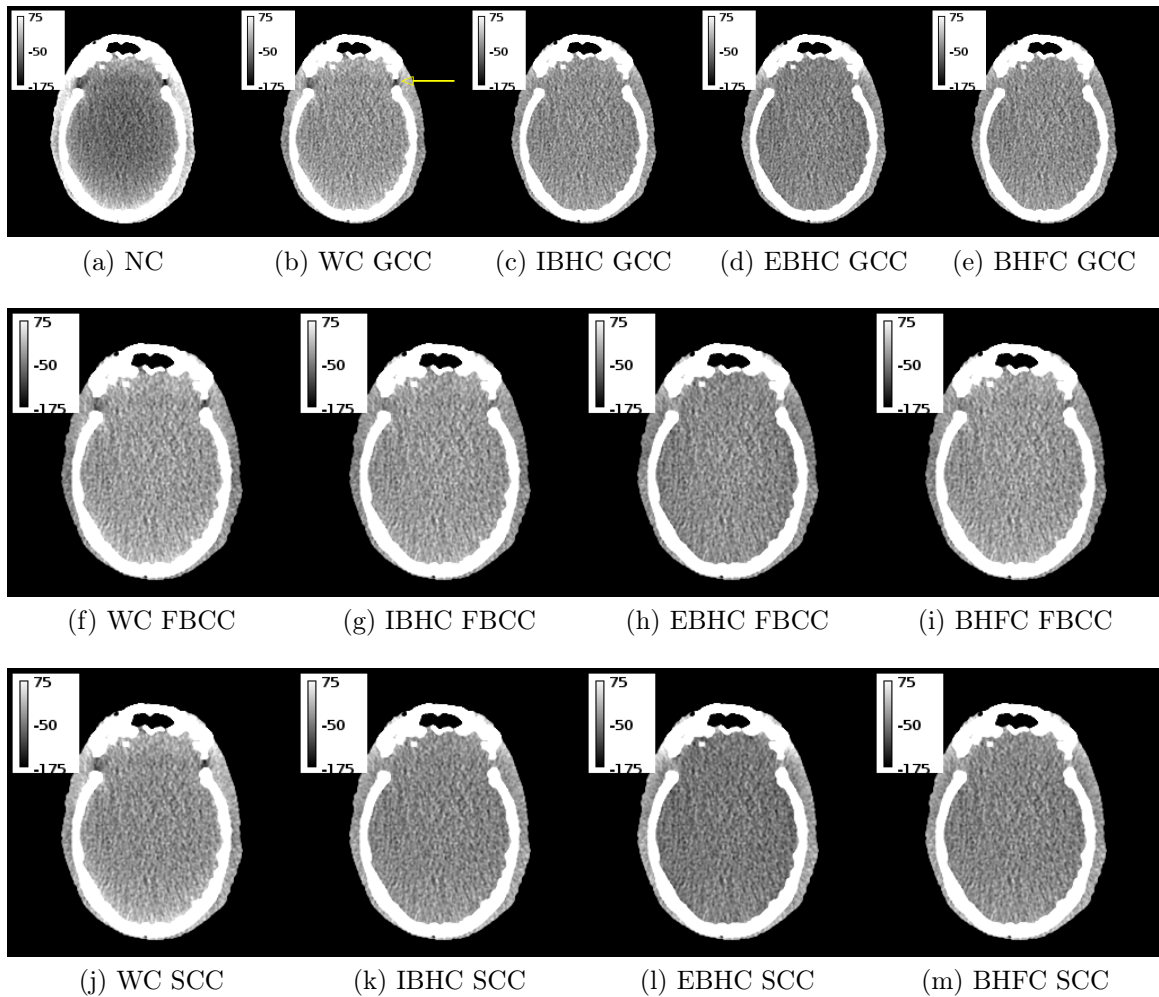


Figure 4.4: Beam hardening correction for the head phantom (LE): (a) NC, reconstructed image without beam hardening correction; (b) WC GCC, after GCC-based water correction; (c) IBHC GCC, after GCC-based water + bone (IBHC) corrections; (d) EBHC GCC, after GCC-based water + bone (EBHC) corrections; (e) BHFC GCC, after GCC-based water + bone (BHFC) corrections; (f) WC FBCC, after FBCC-based water correction; (g) IBHC FBCC, after FBCC-based water + bone (IBHC) corrections; (h) EBHC FBCC, after FBCC-based water + bone (EBHC) corrections; (i) BHFC FBCC, after FBCC-based water + bone (BHFC) corrections; (j) WC SCC, after SCC-based water correction; (k) IBHC SCC, after SCC-based water + bone (IBHC) corrections; (l) EBHC SCC, after SCC-based water + bone (EBHC) corrections; (m) BHFC SCC, after SCC-based water + bone (BHFC) corrections.

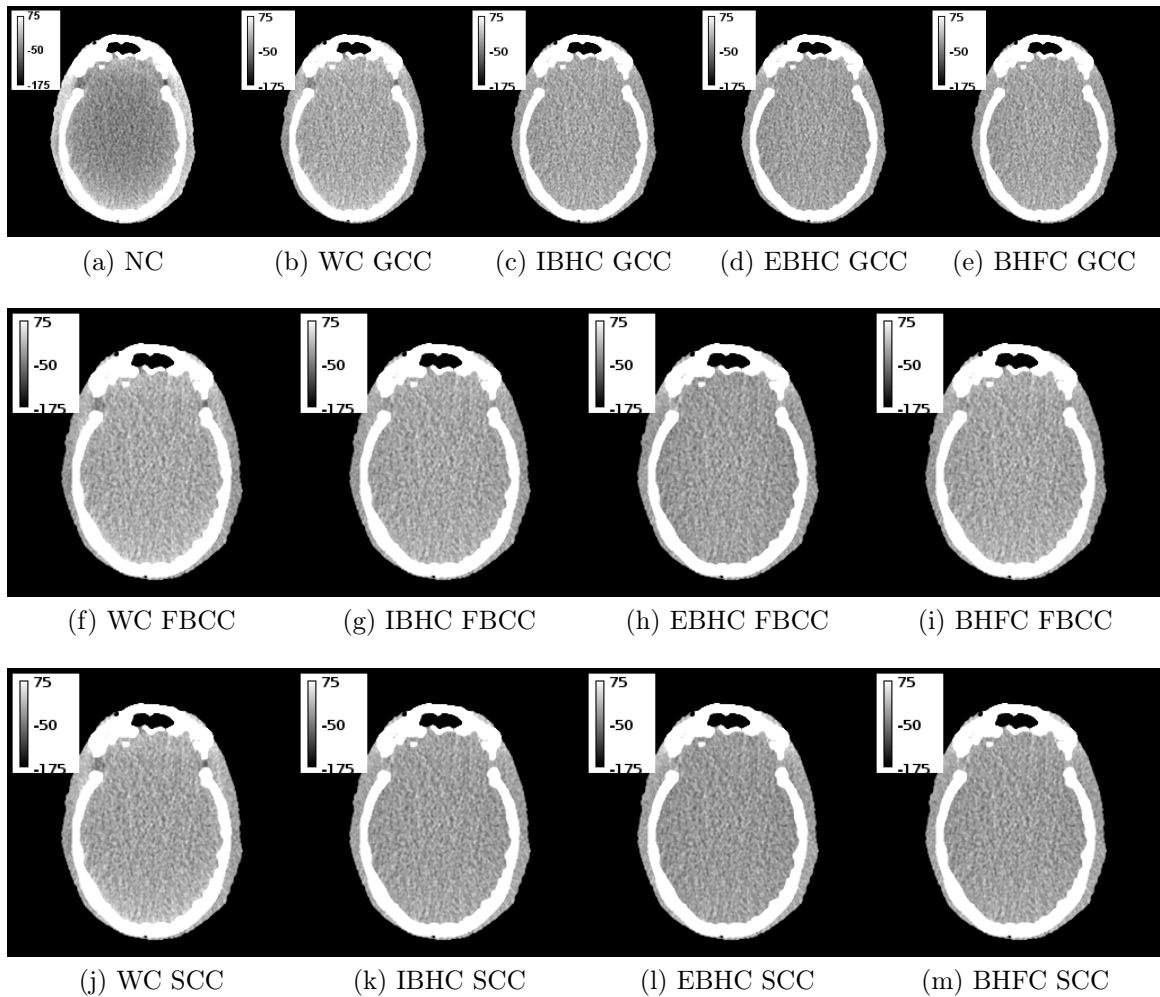


Figure 4.5: Beam hardening correction for the head phantom (HE): (a) NC, reconstructed image without beam hardening correction; (b) WC GCC, after GCC-based water correction; (c) IBHC GCC, after GCC-based water + bone (IBHC) corrections; (d) EBHC GCC, after GCC-based water + bone (EBHC) corrections; (e) BHFC GCC, after GCC-based water + bone (BHFC) corrections; (f) WC FBCC, after FBCC-based water correction; (g) IBHC FBCC, after FBCC-based water + bone (IBHC) corrections; (h) EBHC FBCC, after FBCC-based water + bone (EBHC) corrections; (i) BHFC FBCC, after FBCC-based water + bone (BHFC) corrections; (j) WC SCC, after SCC-based water correction; (k) IBHC SCC, after SCC-based water + bone (IBHC) corrections; (l) EBHC SCC, after SCC-based water + bone (EBHC) corrections; (m) BHFC SCC, after SCC-based water + bone (BHFC) corrections.

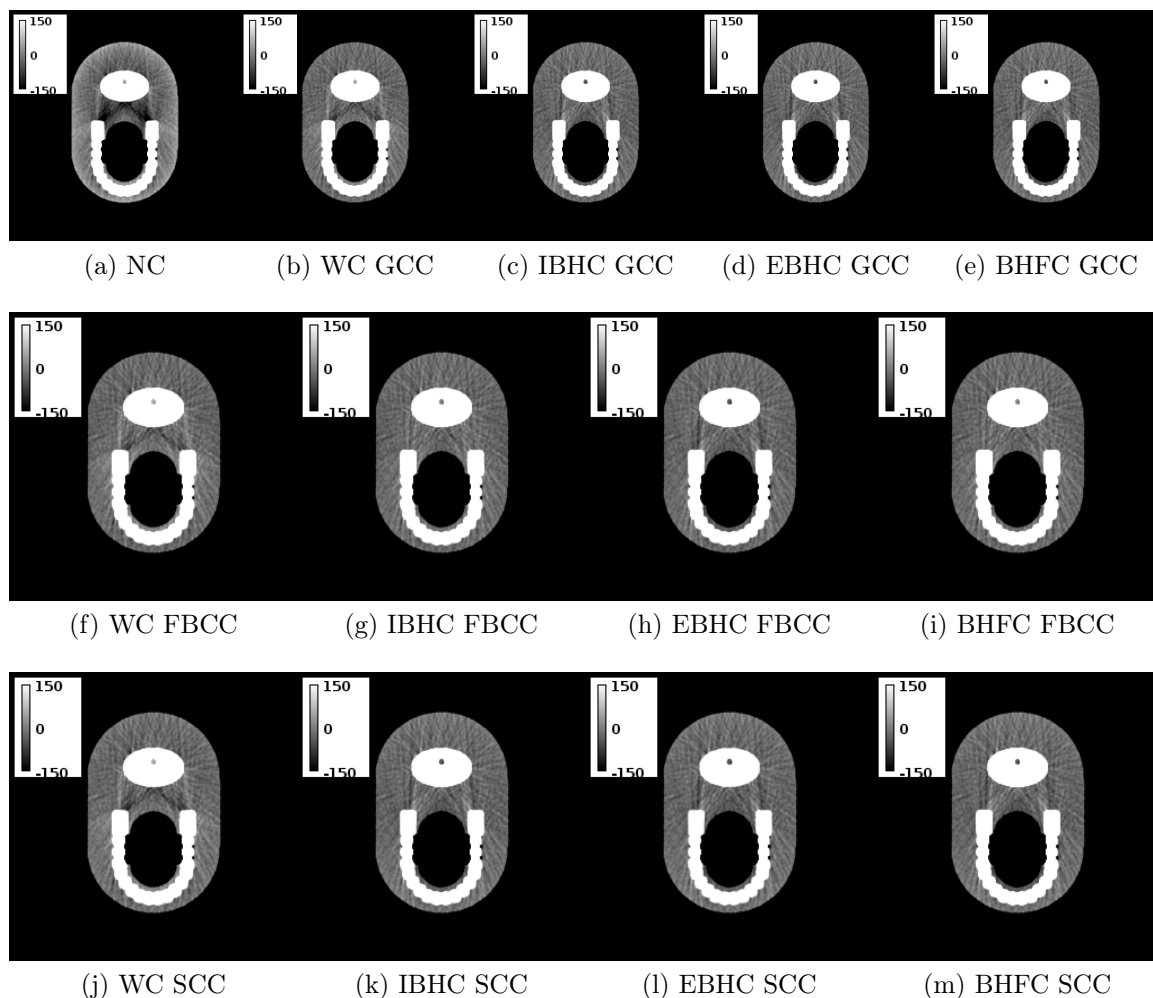


Figure 4.6: Beam hardening correction for the jaw phantom (LE): (a) NC, reconstructed image without beam hardening correction; (b) WC GCC, after GCC-based water correction; (c) IBHC GCC, after GCC-based water + bone (IBHC) corrections; (d) EBHC GCC, after GCC-based water + bone (EBHC) corrections; (e) BHFC GCC, after GCC-based water + bone (BHFC) corrections; (f) WC FBCC, after FBCC-based water correction; (g) IBHC FBCC, after FBCC-based water + bone (IBHC) corrections; (h) EBHC FBCC, after FBCC-based water + bone (EBHC) corrections; (i) BHFC FBCC, after FBCC-based water + bone (BHFC) corrections; (j) WC SCC, after SCC-based water correction; (k) IBHC SCC, after SCC-based water + bone (IBHC) corrections; (l) EBHC SCC, after SCC-based water + bone (EBHC) corrections; (m) BHFC SCC, after SCC-based water + bone (BHFC) corrections.

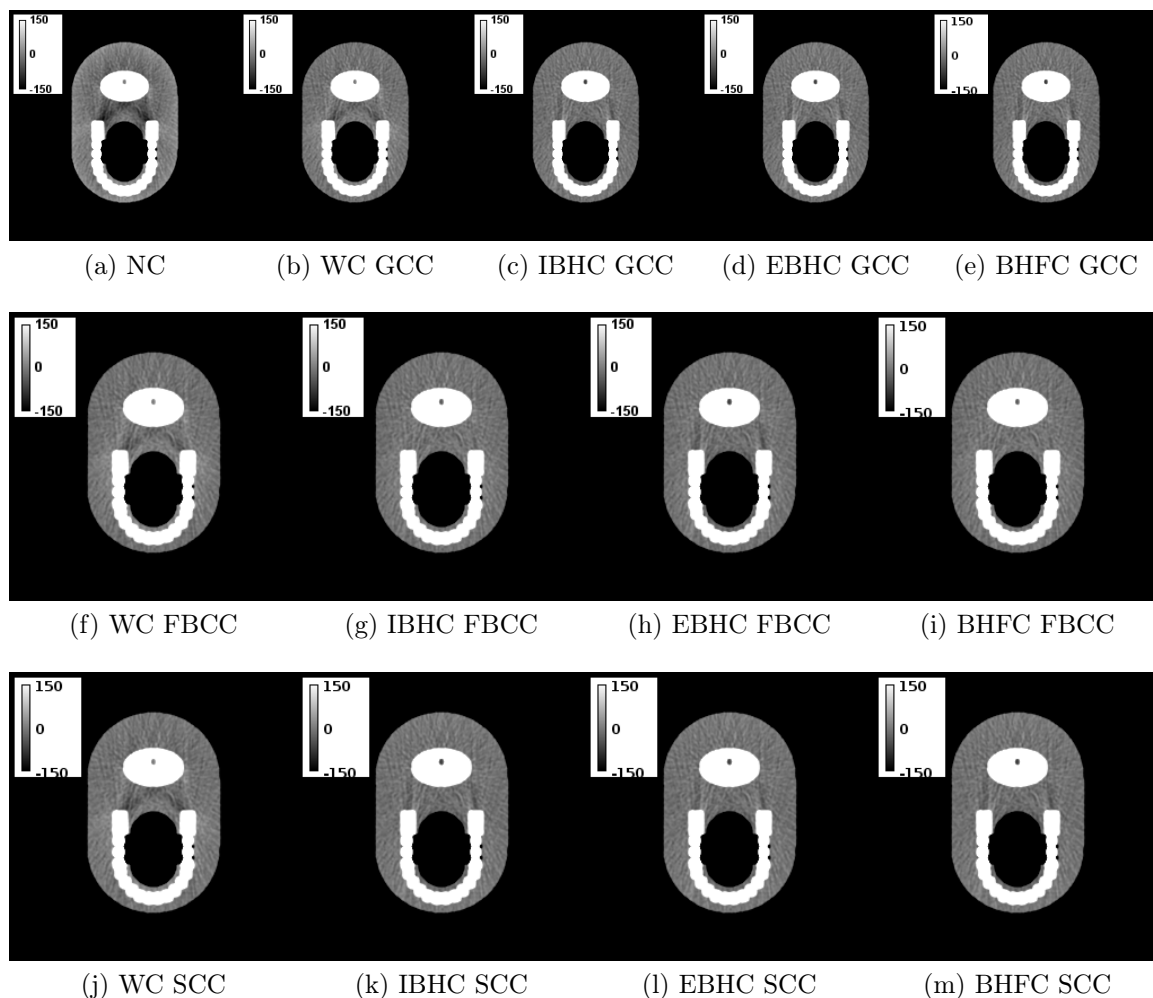
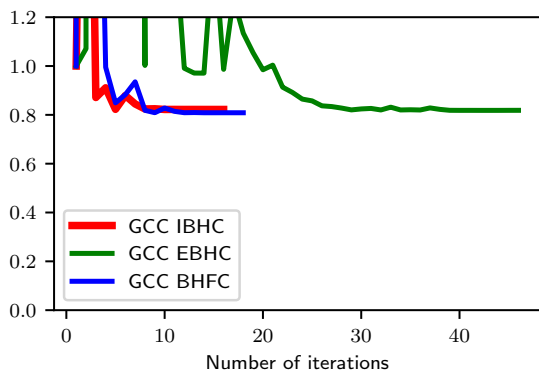
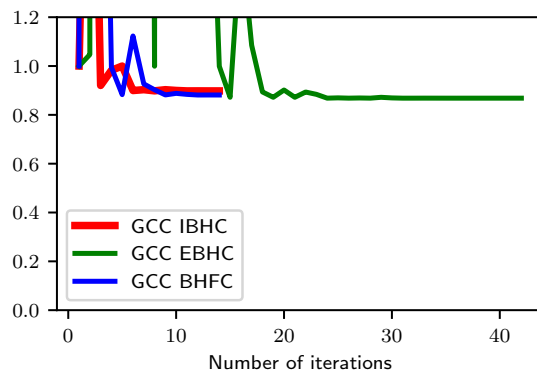


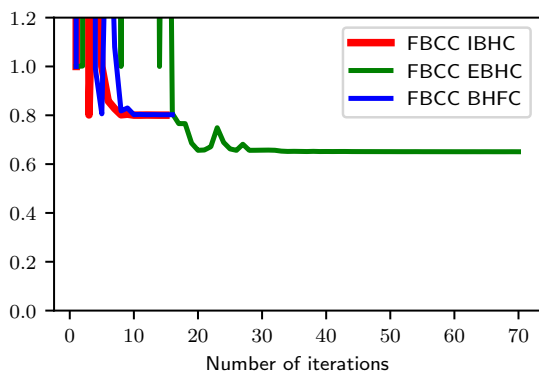
Figure 4.7: Beam hardening correction for the jaw phantom (HE): (a) NC, reconstructed image without beam hardening correction; (b) WC GCC, after GCC-based water correction; (c) IBHC GCC, after GCC-based water + bone (IBHC) corrections; (d) EBHC GCC, after GCC-based water + bone (EBHC) corrections; (e) BHFC GCC, after GCC-based water + bone (BHFC) corrections; (f) WC FBCC, after FBCC-based water correction; (g) IBHC FBCC, after FBCC-based water + bone (IBHC) corrections; (h) EBHC FBCC, after FBCC-based water + bone (EBHC) corrections; (i) BHFC FBCC, after FBCC-based water + bone (BHFC) corrections; (j) WC SCC, after SCC-based water correction; (k) IBHC SCC, after SCC-based water + bone (IBHC) corrections; (l) EBHC SCC, after SCC-based water + bone (EBHC) corrections; (m) BHFC SCC, after SCC-based water + bone (BHFC) corrections.



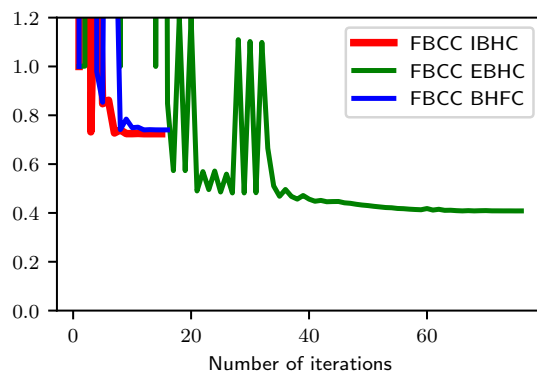
(a) GCC (Jaw, LE)



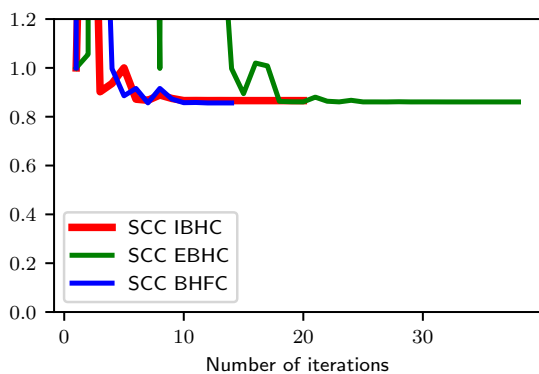
(b) GCC (Head, LE)



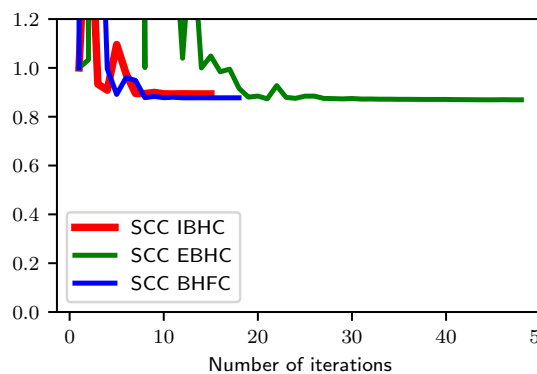
(c) FBCC (Jaw, LE)



(d) FBCC (Head, LE)



(e) SCC (Jaw, LE)



(f) SCC (Head, LE)

Figure 4.8: The minimization of normalized inconsistency measure during higher-order corrections.

Table 4.2: Robust coefficient of variation C_v^r after water and bone corrections.

Phantom	CC	NC	WC	WC + BHFC	WC + IBHC	WC + EBHC
Jaw (LE)	GCC	3.7142	1.6677	1.6143	1.5867	1.5641
Jaw (LE)	FBCC	3.7142	1.6169	1.3692	1.3819	1.5075
Jaw (LE)	SCC	3.7142	1.7245	1.5415	1.4668	1.4667
Jaw (HE)	GCC	2.3654	1.2610	1.1574	1.1297	1.1554
Jaw (HE)	FBCC	2.3654	1.2113	0.9964	0.9987	1.0937
Jaw (HE)	SCC	2.3654	1.3325	1.0922	1.0721	1.0859
Head (LE)	GCC	2.1030	1.8583	1.8095	1.8053	1.7750
Head (LE)	FBCC	2.1030	1.8555	1.8401	1.8364	1.8250
Head (LE)	SCC	2.1030	1.8703	1.7959	1.7928	1.7546
Head (HE)	GCC	1.5714	1.4061	1.3899	1.3864	1.3786
Head (HE)	FBCC	1.5714	1.4061	1.3935	1.3904	1.3839
Head (HE)	SCC	1.5714	1.4108	1.3784	1.3750	1.3663

quality. The coefficient of variation is decreased after all bone correction algorithms irrespective of cone beam consistency conditions.

The reconstructed images of the head and jaw phantoms and the coefficient of variation demonstrate the propensity of EBHC correction for over-compensation. Compared to IBHC, the additional coefficient of EBHC b_3^e is negative in most cases which leads to strong corrections for bone pixels if the prior first-order correction is weak. As the reconstructed images of jaw phantom show, FBCC-based IBHC and BHFC do not generate bright streak artifacts, and the C_v^r is significantly low compared to other correction methods. Since only the bone overlapped projection pixel values are transformed by the higher-order correction algorithms, the slow varying nature of the fan beam intermediate function plays a role in preventing over-correction. In head phantom, SCC-EBHC outperforms other methods to reduce the spill-over artifacts and homogenize the attenuation values. Due to the object's geometry and the selected ROI to compute the C_v^r , the artifacts due to over-corrections did not take account. By contrast, the introduction of bright streak artifacts after SCC and GCC-based EBHC causes the deterioration of C_v^r of the attenuation values of the jaw phantom images.

Fig. 4.8 displays the minimization of normalized inconsistency measures. Compared to the three-parameter optimization of EBHC, the sole parameter of IBHC and BHFC can be estimated with very few iterations.

4.4.2 Clinical Data

Fig. 4.9 shows GCC-based beam hardening corrections for clinical datasets from a C-arm CBCT scanner. The additional bone corrections reduced the spill-over artifacts and preserved the sharp brain-skull boundaries, as displayed in Fig. 4.10. By reducing

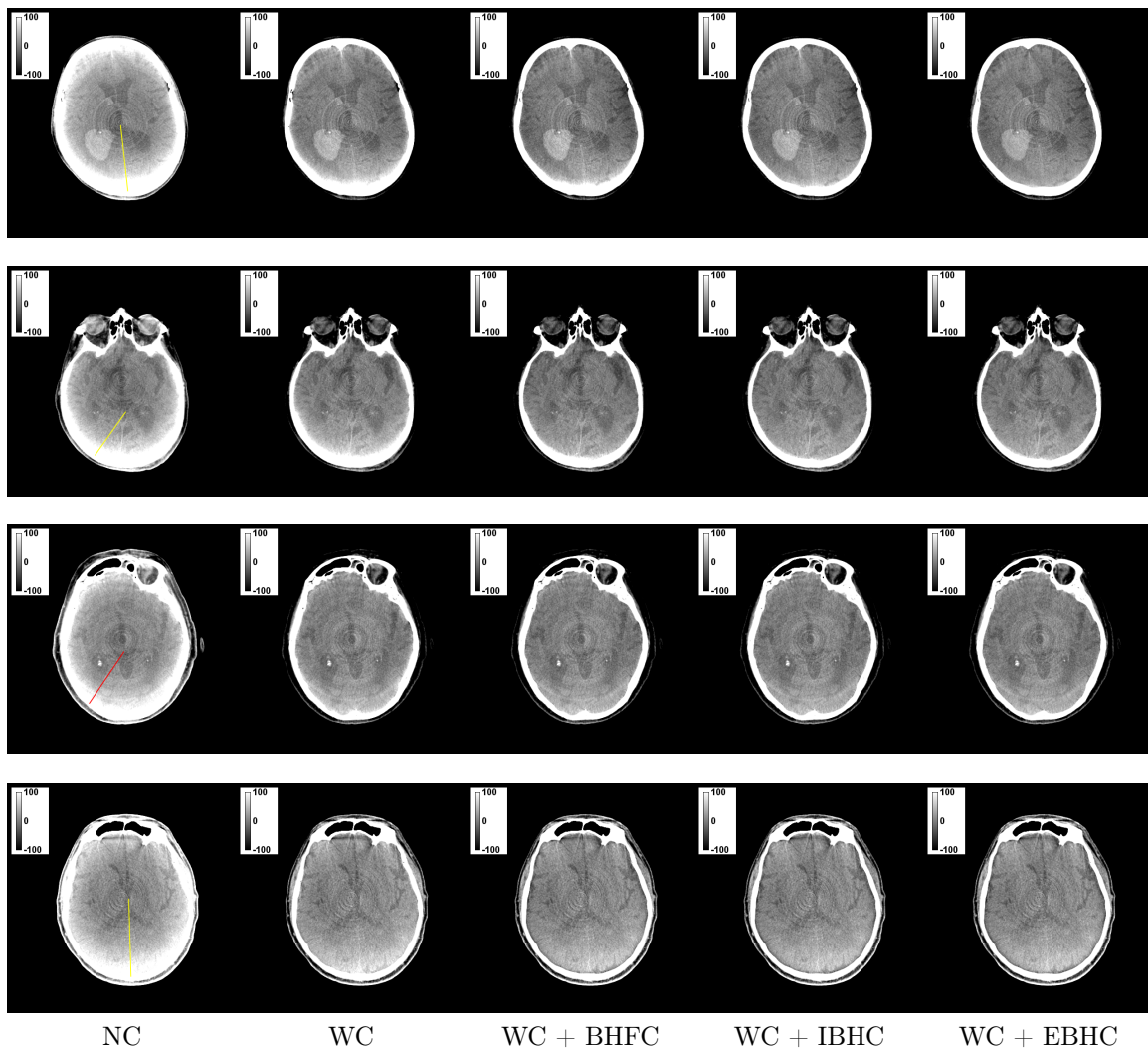


Figure 4.9: GCC-based water and bone corrections for clinical data. Images courtesy of Magdeburg University Hospital, Germany.

the artifacts, low contrast detectability is significantly improved near the boundaries, helping to assess biomarkers. Compared to IBHC and BHFC, the images after EBHC exhibit slightly improved corrections.

Fig. 4.11 and Fig. 4.12 display FBCC and SCC-based corrections. As explained in the last chapter (Sec. 3.4.3), water correction polynomial could not be optimized using both consistency conditions due to truncation and offset-induced projection errors. Since water corrections were performed with the identity function, NC and WC images are the same. By contrast, FBCC and SCC-based bone corrections can deteriorate the image quality due to the forward projection errors and the resultant over-corrections. This effect is predominant in EBHC corrections due to their sus-

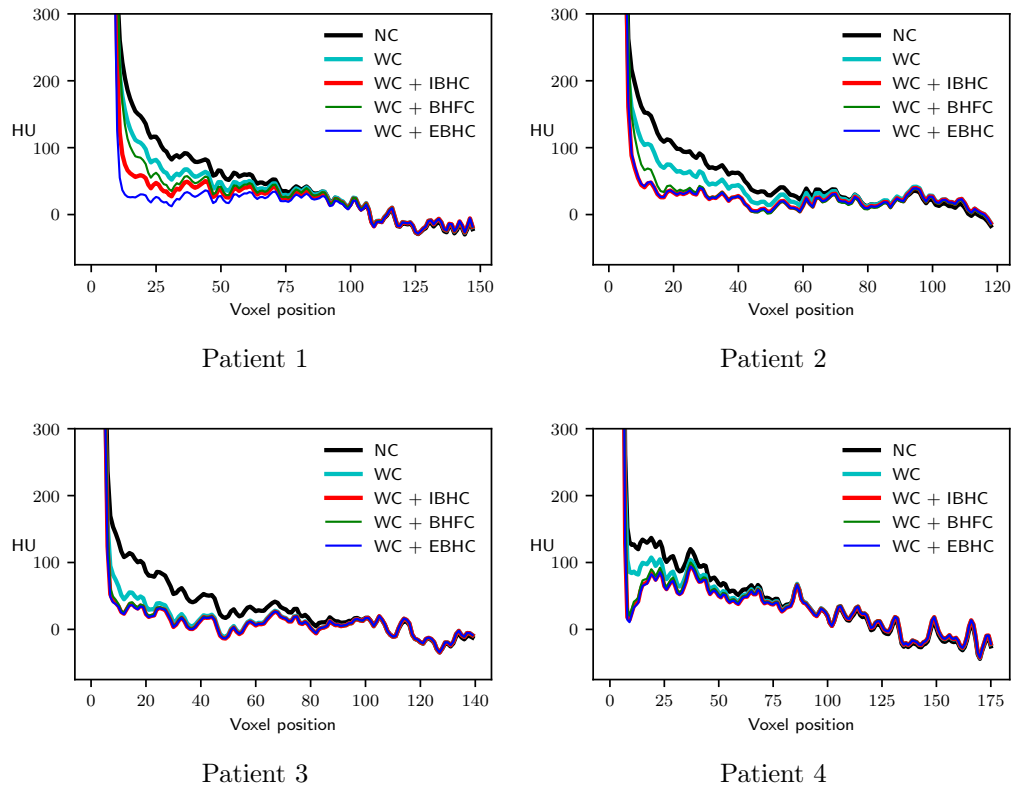


Figure 4.10: Attenuation profiles from the reconstructed images (Fig. 4.9) after GCC-based water and bone corrections.

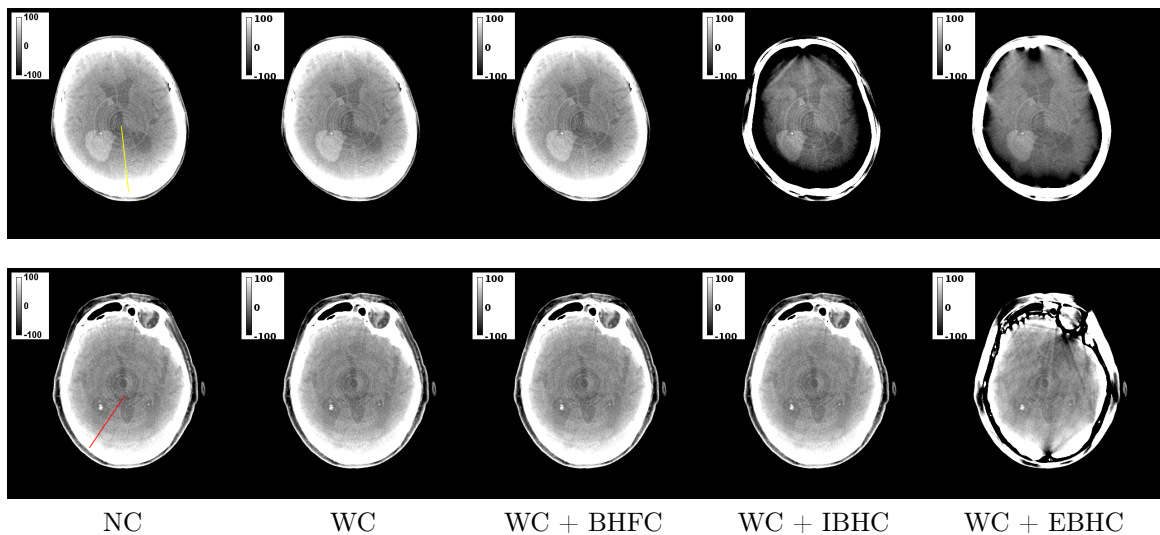


Figure 4.11: FBCC-based water and bone corrections for clinical data. Images courtesy of Magdeburg University Hospital, Germany.

ceptibility to overcompensation. Instead of bone forward projections, BHFC relies on the path length through the bone volume to compute the correction values. Hence, the over-correction due to the forward projection error and the image quality deterioration were avoided in BHFC. The algorithms of IBHC and EBHC can be modified by employing the path length projections to quantify the beam hardening-induced error and projection inconsistency. However, the two-parameter optimization of IBHC needs to be performed without the constraint to maintain the constant area under the IBHC polynomial curve.

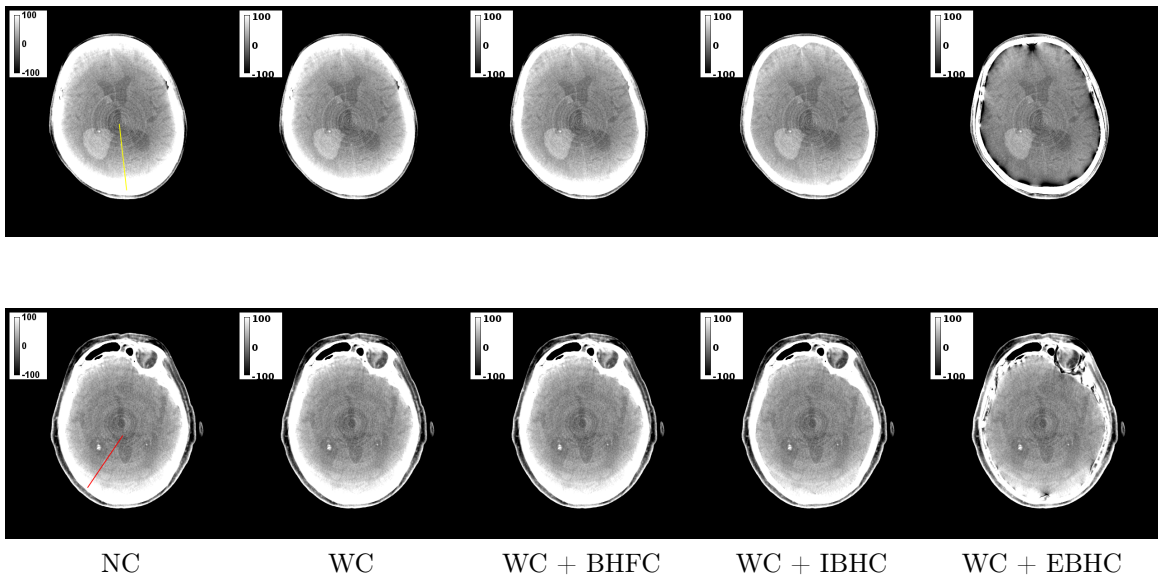


Figure 4.12: SCC-based water and bone corrections for clinical data. Images courtesy of Magdeburg University Hospital, Germany.

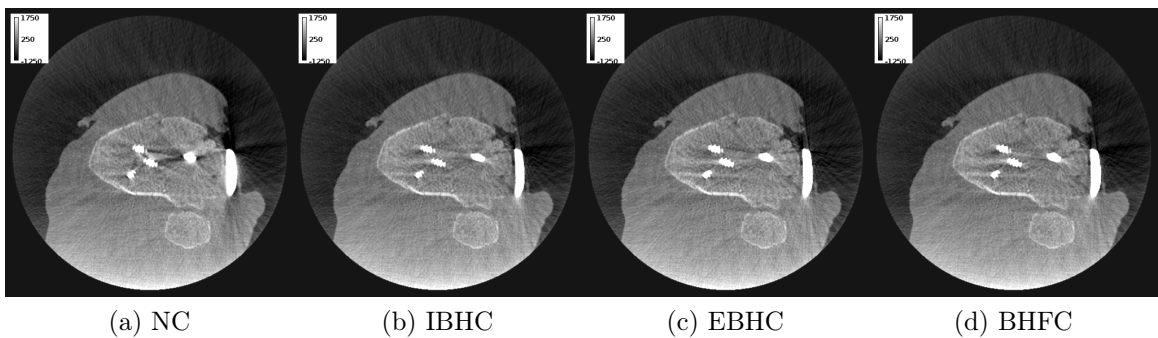


Figure 4.13: GCC-based corrections for metal artifact reduction. Images courtesy of Siemens Healthineers, Forchheim, Germany.

Fig. 4.13 demonstrates the reduction of metal artifacts due to beam hardening

by a tibia implant. The dark streak artifacts around and between the implants are reduced after GCC-based corrections. It is to be noted that the proposed algorithms only correct the metal artifacts due to beam hardening. The complete reduction of metal artifacts induced by various phenomena (e.g., scattering, photon starvation) can only be achieved using the projection completion algorithms like NMAR. However, the interpolation-based projection in-painting may cause the degradation of crucial anatomical details around the large metal implants. In this scenario, CC-based higher-order corrections can be an alternative for MAR algorithms. Artifacts could not be reduced by either FBCC or SCC-based algorithms, similar to clinical head scans.

5 Conclusions and Outlook

In this thesis, the algorithms for data-driven beam hardening correction using consistency conditions have been discussed and evaluated. The coefficients for corrections are directly estimated from CBCT projection data without calibration experiments and prior knowledge about X-ray and attenuation spectra. As the corrected images and quantitative evaluations demonstrate, all three manifestations of beam hardening artifacts are reduced, and the CT number uniformity is restored after the proposed corrections. As per comparison studies, the projection inconsistency is more reliable than the TV of uncorrected volume to quantify beam hardening-induced error. The low contrast resolution of the clinical head scans is significantly improved after water and bone corrections. The efficacy and efficiency of various correction models and cone beam consistency conditions were compared through elaborate experiments. The artifact correction results can be replicated using any cone beam consistency condition if the polychromatic projections are free from additional errors. The slow varying nature of the intermediate function and the lack of high-frequency enhancing filtering operations using adjacent plane integrals make FBCC-based algorithms robust towards Poisson noise, axial truncation, detector shifts, and scatter. However, FBCC-based algorithms are susceptible to the low-frequency distribution of projection offsets making GCC-based algorithms applicable for clinical C-arm CBCT datasets due to the offset canceling derivative filter. SCC-based corrections involve computationally expensive ramp filtering and are very sensitive to truncation. In addition, no significant advantage has been found for SCC over GCC. The comparative studies are valuable to select the appropriate condition for artifact correction based on the prior knowledge about CBCT system geometry and the presence of projection errors other than those caused by beam hardening. The robust artifact correction algorithms can be formulated by combining different consistency conditions to exploit each of their advantages and minimize their risks.

Similarly, consistency condition-based higher-order beam hardening corrections utilizing three prominent models were analyzed and compared. IBHC, EBHC and BHFC are very effective in reducing the artifacts due to polychromatic attenuation by bones and metals, which could not be mitigated by sole water correction. EBHC yields superior artifact reduction with the costs of increased computing time and susceptibility for overcompensation. Clinical head scan images demonstrate the reduction of spill-over artifacts by GCC-based algorithms to retain well-defined brain-skull boundaries. Compared to water correction, higher-order correction algorithms are more sensitive to projection errors due to their reliance on forward projections of the prior reconstructed volume. Clinical images show FBCC and SCC-based higher-order cor-

rections may cause the deterioration of image quality by introducing artifacts. This over-correction can be minimized by replacing the forward projections with the path lengths for EBHC and IBHC.

The major limitation of the proposed algorithms is their susceptibility to geometrical and physical measurement errors. It is found that the algorithms are susceptible to a high degree of lateral truncations. As a result, the polynomial for water correction could not be optimized for thorax and abdominal scans of interventional and mobile C-arm CBCT scanners. The impact of different truncation correction algorithms on polynomial optimization is a potential area of future work. The extrapolation of projections using consistency conditions to correct lateral truncation artifacts is an ongoing research area. In the future, it may be possible to optimize the correction polynomial from the truncated projections after consistency conditions-based projection extrapolation. Similarly, the susceptibility to miscalibration artifacts can be reduced by estimating the accurate projection geometry parameters using consistency conditions. Algorithms for data-driven geometric calibration have been published and successfully applied in industrial and clinical CBCT scanners.

In consistency condition-based beam hardening correction, the projection linearization is performed using a global polynomial or correction coefficients irrespective of projection view and detector pixel location. This approach may not be optimal if the projection acquisition involves a strong heel effect, tube voltage modulation, bow tie filter, and detector in-homogeneities. In such scenarios, projection or pixel-specific corrections may be advantageous for effective artifact reduction. It will be very computationally expensive to estimate numerous coefficients using consistency conditions alone. By incorporating prior knowledge (e.g., voltage distribution, detector efficiency), the parameter estimations can be simplified.

The projection error due to the underestimation of total attenuation values caused by beam hardening, scattering, and detector in-homogeneities is compensated by additive correction. The experiments have demonstrated that the cupping artifacts due to scatter were also reduced after polynomial-based projection linearization. If the scatter to primary ratio is very high, the scatter artifacts can be corrected by estimating the additive correction images using convolution-based analytical models. Like the polynomials for beam hardening corrections, the scatter kernel parameters can be optimized without calibration by enforcing consistency conditions. The preliminary results have shown promising results by reducing the scatter-induced cupping and streak artifacts. However, the estimation of projection-specific kernel parameters using pair-wise consistency conditions is a challenging task. An effective scatter correction algorithm can be developed by incorporating prior knowledge about the distribution of kernel parameter values.

The results have also shown that the artifacts due to beam hardening by metal implants could be reduced by higher-order methods using consistency conditions. However, a significant reduction of metal artifacts is only possible with sophisticated MAR algorithms like NMAR. Here, the consistency conditions can be explored to improve interpolation accuracy or estimate the optimal parameters for TV-based

inpainting.

Appendices

Proofs

.1 Beer-Lambert Law

$$I_t(E) = I_0(E) e^{-\mu(E)l} \quad (.1)$$

Proof.

$$\begin{aligned} \frac{dI(E)}{I(E)} &= -\mu(E) dl \\ \int \frac{dI(E)}{I(E)} &= -\mu(E) \int dl \\ \ln(I_t(E)) &= -\mu(E)l + C \text{ where } C = \ln(I_0(E)) \\ I_t(E) &= I_0(E) e^{-\mu(E)l} \quad \square \end{aligned} \quad (.2)$$

.2 Redundancy of 2D Radon Transform

$$\mathcal{R}_2\mu(\theta + \pi, -s) = \mathcal{R}_2\mu(\theta, s) \quad (.3)$$

Proof.

$$\begin{aligned} \mathcal{R}_2\mu(\theta + \pi, -s) &= \int_{\mathbf{x} \in \mathbb{R}^2} \mu(\mathbf{x}) \delta(\langle \mathbf{x}, -\hat{\boldsymbol{\theta}} \rangle + s) d\mathbf{x} \text{ where } \begin{bmatrix} \cos(\theta + \pi) \\ \sin(\theta + \pi) \end{bmatrix} = -\hat{\boldsymbol{\theta}} \\ &= \int_{\mathbf{x} \in \mathbb{R}^2} \mu(\mathbf{x}) \delta(-(\langle \mathbf{x}, \hat{\boldsymbol{\theta}} \rangle - s)) d\mathbf{x} \text{ since } \langle \mathbf{x}, -\hat{\boldsymbol{\theta}} \rangle = -\langle \mathbf{x}, \hat{\boldsymbol{\theta}} \rangle \\ &= \int_{\mathbf{x} \in \mathbb{R}^2} \mu(\mathbf{x}) \delta(\langle \mathbf{x}, \hat{\boldsymbol{\theta}} \rangle - s) d\mathbf{x} \text{ since } \delta(-x) = \delta(x) \\ &= \mathcal{R}_2\mu(\theta, s) \quad \square \end{aligned}$$

.3 Fourier Slice Theorem in 2D

$$\begin{aligned} \mathcal{F}_1 \mathcal{R}_2\mu(\sigma; \hat{\boldsymbol{\theta}}) &= \mathcal{F}_2\mu(\boldsymbol{\nu}) \Big|_{\boldsymbol{\nu}=\sigma\hat{\boldsymbol{\theta}}} \\ &= \mathcal{F}_2\mu(\sigma\hat{\boldsymbol{\theta}}) \end{aligned} \quad (.4)$$

Proof.

$$\begin{aligned}
 \mathcal{F}_1 \mathcal{R}_2 \mu(\sigma; \hat{\boldsymbol{\theta}}) &= \int_{s \in \mathbb{R}} \mathcal{R}_2 \mu(s; \hat{\boldsymbol{\theta}}) e^{-i2\pi s \sigma} ds \\
 &= \int_{s \in \mathbb{R}} \left[\int_{l \in \mathbb{R}} \mu(s\hat{\boldsymbol{\theta}} + l\hat{\boldsymbol{\theta}}^\perp) dl \right] e^{-i2\pi s \sigma} ds \\
 &= \int_{s \in \mathbb{R}} \int_{l \in \mathbb{R}} \mu(s\hat{\boldsymbol{\theta}} + l\hat{\boldsymbol{\theta}}^\perp) e^{-i2\pi s \sigma} dl ds
 \end{aligned} \tag{.5}$$

By using the change of variables $\mathbf{x} = s\hat{\boldsymbol{\theta}} + l\hat{\boldsymbol{\theta}}^\perp$ where $s = \langle \mathbf{x}, \hat{\boldsymbol{\theta}} \rangle$ and the Jacobian determinant $\det \mathbf{J} = 1$:

$$\begin{aligned}
 \mathcal{F}_1 \mathcal{R}_2 \mu(\sigma; \hat{\boldsymbol{\theta}}) &= \int_{\mathbf{x} \in \mathbb{R}^2} \mu(\mathbf{x}) e^{-i2\pi \sigma \langle \mathbf{x}, \hat{\boldsymbol{\theta}} \rangle} d\mathbf{x} \\
 &= \int_{\mathbf{x} \in \mathbb{R}^2} \mu(\mathbf{x}) e^{-i2\pi \langle \mathbf{x}, \sigma \hat{\boldsymbol{\theta}} \rangle} d\mathbf{x} \\
 &= \mathcal{F}_2 \mu(\boldsymbol{\nu}) \Big|_{\boldsymbol{\nu} = \sigma \hat{\boldsymbol{\theta}}} \\
 &= \mathcal{F}_2 \mu(\sigma \hat{\boldsymbol{\theta}}) \quad \square
 \end{aligned}$$

.4 Scaling Property of Ramp Filter

$$h_r(cs) = \frac{1}{c^2} h_r(s), \quad \forall c \neq 0 \tag{.6}$$

Proof.

$$\begin{aligned}
 h_r(cs) &= \int_{\sigma \in \mathbb{R}} |\sigma| e^{i2\pi \sigma cs} d\sigma \\
 &= \frac{1}{c^2} \int_{\sigma \in \mathbb{R}} |\sigma'| e^{i2\pi \sigma' s} d\sigma' \text{ after substituting } \sigma' = c\sigma \\
 &= \frac{1}{c^2} h_r(s)
 \end{aligned} \tag{.7}$$

□

.5 Zeroth-order HLCC

$$\begin{aligned} C(\theta) &= \int_{s \in \mathbb{R}} \mathcal{R}_2(s, \theta) \, ds \\ &= \mathcal{R}_3(\hat{\Theta}, t) \end{aligned} \quad (.8)$$

Proof. By substituting Eq. 2.27 in the above equation:

$$C(\theta) = \int_{s \in \mathbb{R}} ds \int_{l \in \mathbb{R}} \mu(s\hat{\theta} + l\hat{\theta}^\perp) \, dl \quad (.9)$$

And using the change of variables $\mathbf{x} = s\hat{\theta} + l\hat{\theta}^\perp$ where the Jacobian determinant $\det \mathbf{J} = 1$:

$$\begin{aligned} C(\theta) &= \int_{\mathbf{x} \in \mathbb{R}^2} \mu(\mathbf{x}) \, d\mathbf{x} \\ &= \mathcal{R}_3(\hat{\Theta}, t) \end{aligned} \quad \square$$

.6 Grangeat's Fundamental Relation

$$\begin{aligned} G^i(\hat{\Theta}_k) &= - \int_{\hat{\beta} \in \mathbb{S}^2} \delta'(\langle \hat{\Theta}_k, \hat{\beta} \rangle) g_m(\hat{\beta}, \mathbf{f}(\alpha_i)) \, d\hat{\beta} \\ &= \left. \frac{\partial}{\partial t} \mathcal{R}_3 \mu(\hat{\Theta}_k, t) \right|_{t=\langle \mathbf{f}(\alpha_i), \hat{\Theta}_k \rangle} \end{aligned} \quad (.10)$$

Proof. By substituting Eq. 2.64,

$$G^i(\hat{\Theta}_k) = - \int_{\hat{\beta} \in \mathbb{S}^2} \int_{l \in \mathbb{R}} \delta'(\langle \hat{\Theta}_k, \hat{\beta} \rangle) \mu(\mathbf{f}(\alpha_i) + l\hat{\beta}) \, dl \, d\hat{\beta} \quad (.11)$$

By using the change of variables $\mathbf{x} = \mathbf{f}(\alpha_i) + l\hat{\beta}$ where $\det \mathbf{J} = l^2$, the above equation can be expressed as:

$$\begin{aligned} G^i(\hat{\Theta}_k) &= - \int_{\mathbf{x} \in \mathbb{R}^3} \delta'(\langle \hat{\Theta}_k, \hat{\beta} \rangle) \mu(\mathbf{x}) \frac{1}{l^2} \, d\mathbf{x} \\ &= - \int_{\mathbf{x} \in \mathbb{R}^3} \delta' \left(\left\langle \hat{\Theta}_k, \frac{\mathbf{x} - \mathbf{f}(\alpha_i)}{l} \right\rangle \right) \mu(\mathbf{x}) \frac{1}{l^2} \, d\mathbf{x} \\ &= - \int_{\mathbf{x} \in \mathbb{R}^3} \delta' \left(\frac{1}{l} \langle \hat{\Theta}_k, \mathbf{x} - \mathbf{f}(\alpha_i) \rangle \right) \mu(\mathbf{x}) \frac{1}{l^2} \, d\mathbf{x} \end{aligned} \quad (.12)$$

Similar to ramp filter (Eq. 2.42), the derivative of Dirac distribution also exhibits scaling property:

$$\delta'(cx) = \frac{1}{c^2} \delta'(x) \quad (.13)$$

Therefore,

$$\begin{aligned} G^i(\hat{\Theta}_k) &= - \int_{\mathbf{x} \in \mathbb{R}^3} \delta'(\langle \hat{\Theta}_k, \mathbf{x} - \mathbf{f}(\alpha_i) \rangle) \mu(\mathbf{x}) \, d\mathbf{x} \\ &= - \int_{\mathbf{x} \in \mathbb{R}^3} \delta'(\langle \hat{\Theta}_k, \mathbf{x} \rangle - \langle \hat{\Theta}_k, \mathbf{f}(\alpha_i) \rangle) \mu(\mathbf{x}) \, d\mathbf{x} \\ &= \int_{\mathbf{x} \in \mathbb{R}^3} \delta(\langle \hat{\Theta}_k, \mathbf{x} \rangle - \langle \hat{\Theta}_k, \mathbf{f}(\alpha_i) \rangle) \mu'(\mathbf{x}) \, d\mathbf{x}, \text{ as per Eq. 2.82} \\ &= \int_{\mathbf{x} \in \mathbb{R}^3} \mu'(\mathbf{x}) \, d\mathbf{x} \int_{t \in \mathbb{R}} \delta(\langle \hat{\Theta}_k, \mathbf{x} \rangle - t) \delta(t - \langle \hat{\Theta}_k, \mathbf{f}(\alpha_i) \rangle) \, dt \\ &= - \int_{t \in \mathbb{R}} \delta'(t - \langle \hat{\Theta}_k, \mathbf{f}(\alpha_i) \rangle) \int_{\mathbf{x} \in \mathbb{R}^3} \mu(\mathbf{x}) \delta(\langle \hat{\Theta}_k, \mathbf{x} \rangle - t) \, d\mathbf{x} \\ &= - \int_{t \in \mathbb{R}} \delta'(t - \langle \hat{\Theta}_k, \mathbf{f}(\alpha_i) \rangle) \mathcal{R}_3 \mu(\hat{\Theta}_k, t) \\ &= \int_{t \in \mathbb{R}} \delta(t - \langle \hat{\Theta}_k, \mathbf{f}(\alpha_i) \rangle) \frac{\partial}{\partial t} \mathcal{R}_3 \mu(\hat{\Theta}_k, t) \\ &= \frac{\partial}{\partial t} \mathcal{R}_3 \mu(\hat{\Theta}_k, t) \Big|_{t=\langle \hat{\Theta}_k, \mathbf{f}(\alpha_i) \rangle} \quad \square \end{aligned}$$

.7 Grangeat Intermediate Function from FDCT Projections

$$G^i(\hat{\Theta}_k) = G(\theta_k^i, s_k^i) = \frac{(s_k^i)^2 + (D^i)^2}{(D^i)^2} \frac{\partial}{\partial s_k^i} \mathcal{R}_2 g_m^c(\theta_k^i, s_k^i) \quad (.14)$$

Proof. The unit direction vector $\hat{\beta} \in \mathbb{S}^2$ in Source Detector Coordinate System (SDCS) is given by:

$$\hat{\beta} = \frac{u \hat{\mathbf{u}}(\alpha_i) + v \hat{\mathbf{v}}(\alpha_i) + D^i \hat{\mathbf{w}}(\alpha_i)}{\sqrt{u^2 + v^2 + (D^i)^2}} \quad (.15)$$

$\hat{\boldsymbol{\theta}}_k^i$ and $\hat{\boldsymbol{\theta}}_k^{i\perp}$ denote the normal vector to the line $\mathcal{L}(\theta_k^i, s_k^i)$ and the line direction in DCS:

$$\hat{\boldsymbol{\theta}}_k^i = \cos \theta_k^i \hat{\boldsymbol{u}}(\alpha_i) + \sin \theta_k^i \hat{\boldsymbol{v}}(\alpha_i) \quad (.16)$$

$$\hat{\boldsymbol{\theta}}_k^{i\perp} = -\sin \theta_k^i \hat{\boldsymbol{u}}(\alpha_i) + \cos \theta_k^i \hat{\boldsymbol{v}}(\alpha_i) \quad (.17)$$

$s_k^i \hat{\boldsymbol{\theta}}_k^i + D^i \hat{\boldsymbol{w}}(\alpha_i)$ represents the line from the X-ray source to the detector which lies in the plane $\Pi(\hat{\boldsymbol{\Theta}}_k, t)$ and perpendicular to the line $\mathcal{L}(\theta_k^i, s_k^i)$. The plane normal vector can be computed by the cross product of two in-plane vectors:

$$\begin{aligned} \hat{\boldsymbol{\Theta}}_k &= \frac{s_k^i \hat{\boldsymbol{\theta}}_k^i + D^i \hat{\boldsymbol{w}}(\alpha_i)}{\left\| s_k^i \hat{\boldsymbol{\theta}}_k^i + D^i \hat{\boldsymbol{w}}(\alpha_i) \right\|} \times \hat{\boldsymbol{\theta}}_k^{i\perp} \\ &= \frac{s_k^i \cos \theta_k^i \hat{\boldsymbol{u}}(\alpha_i) + s_k^i \sin \theta_k^i \hat{\boldsymbol{v}}(\alpha_i) + D^i \hat{\boldsymbol{w}}(\alpha_i)}{\sqrt{(s_k^i)^2 + (D^i)^2}} \times -\sin \theta_k^i \hat{\boldsymbol{u}}(\alpha_i) + \cos \theta_k^i \hat{\boldsymbol{v}}(\alpha_i) \\ &= \frac{-D^i \cos \theta_k^i \hat{\boldsymbol{u}}(\alpha_i) - D^i \sin \theta_k^i \hat{\boldsymbol{v}}(\alpha_i) + s_k^i \hat{\boldsymbol{w}}(\alpha_i)}{\sqrt{(s_k^i)^2 + (D^i)^2}} \end{aligned} \quad (.18)$$

The dot product of $\hat{\boldsymbol{\Theta}}_k$ and $\hat{\boldsymbol{\beta}}$ (Eq. .15) is given by:

$$\langle \hat{\boldsymbol{\Theta}}_k, \hat{\boldsymbol{\beta}} \rangle = \frac{-D^i}{\sqrt{(s_k^i)^2 + (D^i)^2}} \frac{u \cos \theta_k^i + v \sin \theta_k^i - s_k^i}{\sqrt{u^2 + v^2 + (D^i)^2}} \quad (.19)$$

By utilizing the spherical to Cartesian coordinate transformation for surface integral ($\hat{\boldsymbol{\beta}} \rightarrow (u, v)$) and substituting Eq. .19 in Eq. 2.81 [59]:

$$G^i(\hat{\boldsymbol{\Theta}}_k) = - \iiint \delta' \left(\frac{-D^i}{\sqrt{(s_k^i)^2 + (D^i)^2}} \frac{u \cos \theta_k^i + v \sin \theta_k^i - s_k^i}{\sqrt{u^2 + v^2 + (D^i)^2}} \right) g_m(u, v, \alpha_i) \left\| \frac{\partial \hat{\boldsymbol{\beta}}}{\partial u} \times \frac{\partial \hat{\boldsymbol{\beta}}}{\partial v} \right\| dudv \quad (.20)$$

Using Eq. .13 and Eq. 2.66 [31],

$$\begin{aligned} G^i(\hat{\boldsymbol{\Theta}}_k) &= -\frac{(s_k^i)^2 + (D^i)^2}{(D^i)^2} \iiint \delta' (u \cos \theta_k^i + v \sin \theta_k^i - s_k^i) g_m^c(u, v, \alpha_i) dudv \\ &= \frac{(s_k^i)^2 + (D^i)^2}{(D^i)^2} \frac{\partial}{\partial s_k^i} \mathcal{R}_2 g_m^c(\theta_k^i, s_k^i) \quad \square \end{aligned}$$

.8 Smith Intermediate Function

$$\begin{aligned}
 S^i(\hat{\Theta}_k) &= \int_{\hat{\beta} \in \mathbb{S}^2} h_r(\langle \hat{\Theta}_k, \hat{\beta} \rangle) g_m(\hat{\beta}, \mathbf{f}(\alpha_i)) d\hat{\beta} \\
 &= h_r(t) * \mathcal{R}_3\mu(\hat{\Theta}_k, t) \Big|_{t=\langle \mathbf{f}(\alpha_i), \hat{\Theta}_k \rangle}
 \end{aligned} \tag{.21}$$

Proof. By employing the same change of variables used to prove Grangeat fundamental relation (.6) and the scaling property of ramp function (Eq. 2.42) :

$$\begin{aligned}
 S^i(\hat{\Theta}_k) &= \int_{\mathbf{x} \in \mathbb{R}^3} h_r(\langle \hat{\Theta}_k, \mathbf{x} - \mathbf{f}(\alpha_i) \rangle) \mu(\mathbf{x}) d\mathbf{x} \\
 &= \int_{\mathbf{x} \in \mathbb{R}^3} h_r(\langle \hat{\Theta}_k, \mathbf{x} \rangle - \langle \hat{\Theta}_k, \mathbf{f}(\alpha_i) \rangle) \mu(\mathbf{x}) d\mathbf{x} \\
 &= \int_{\mathbf{x} \in \mathbb{R}^3} \mu(\mathbf{x}) d\mathbf{x} \int_{t \in \mathbb{R}} h_r(t - \langle \hat{\Theta}_k, \mathbf{f}(\alpha_i) \rangle) \delta(\langle \hat{\Theta}_k, \mathbf{x} \rangle - t) dt \\
 &= \int_{t \in \mathbb{R}} h_r(t - \langle \hat{\Theta}_k, \mathbf{f}(\alpha_i) \rangle) dt \int_{\mathbf{x} \in \mathbb{R}^3} \mu(\mathbf{x}) \delta(\langle \hat{\Theta}_k, \mathbf{x} \rangle - t) \\
 &= \int_{t \in \mathbb{R}} h_r(t - \langle \hat{\Theta}_k, \mathbf{f}(\alpha_i) \rangle) \mathcal{R}_3\mu(\hat{\Theta}_k, t) dt \\
 &= \int_{t \in \mathbb{R}} h_r(\langle \hat{\Theta}_k, \mathbf{f}(\alpha_i) \rangle - t) \mathcal{R}_3\mu(\hat{\Theta}_k, t) dt, \text{ since } h_r \text{ is an even function} \\
 &= h_r(t) * \mathcal{R}_3\mu(\hat{\Theta}_k, t) \Big|_{t=\langle \hat{\Theta}_k, \mathbf{f}(\alpha_i) \rangle}
 \end{aligned}$$

□

.9 Scatter Projections

The total attenuation values of scatter-free g_m and scatter-corrupted g_m^s projection are related by the following equation:

$$g_m^s(u, v, \alpha) = g_m(u, v, \alpha) - \ln(1 + SPR(u, v, \alpha)) \tag{.22}$$

Proof.

$$g_m(u, v, \alpha) = \ln\left(\frac{I_0(u, v, \alpha)}{I_t(u, v, \alpha)}\right) \tag{.23}$$

$$g_m^s(u, v, \alpha) = \ln \left(\frac{I_0(u, v, \alpha)}{I_t(u, v, \alpha) + I_s(u, v, \alpha)} \right) \quad (.24)$$

The scatter-induced projection error due to the underestimation of total attenuation values is given by:

$$\begin{aligned} g_m(u, v, \alpha) - g_m^s(u, v, \alpha) &= \ln \left(\frac{I_t(u, v, \alpha) + I_s(u, v, \alpha)}{I_t(u, v, \alpha)} \right) \\ &= \ln(1 + SPR(u, v, \alpha)) \end{aligned} \quad (.25)$$

Hence,

$$g_m^s(u, v, \alpha) = g_m(u, v, \alpha) - \ln(1 + SPR(u, v, \alpha)) \quad (.26)$$

□

Bibliography

- [1] Exponential decay - wikipedia. https://en.wikipedia.org/wiki/Exponential_decay. (Accessed on 04/23/2020).
- [2] Nist: X-ray mass atten. coef. - tissue, soft (icru-44). <https://physics.nist.gov/PhysRefData/XrayMassCoef/ComTab/tissue.html>. (Accessed on 2020-04-24).
- [3] Nist: X-ray mass attenuation coefficients - bone, cortical. <https://physics.nist.gov/PhysRefData/XrayMassCoef/ComTab/bone.html>. (Accessed on 2020-04-24).
- [4] Nist: X-ray mass attenuation coefficients - iodine. <https://physics.nist.gov/PhysRefData/XrayMassCoef/ElemTab/z53.html>. (Accessed on 2020-04-24).
- [5] Nist: X-ray mass attenuation coefficients - titanium. <https://physics.nist.gov/PhysRefData/XrayMassCoef/ElemTab/z22.html>. (Accessed on 2020-04-24).
- [6] Nist: X-ray mass attenuation coefficients - water, liquid. <https://physics.nist.gov/PhysRefData/XrayMassCoef/ComTab/water.html>. (Accessed on 2020-04-24).
- [7] Siemens artis q. <https://www.siemens-healthineers.com/de/angio/artis-interventional-angiography-systems/artis-q>. Accessed: 2020-12-31.
- [8] Somatom definition flash. <https://www.siemens-healthineers.com/en-us/computed-tomography/ecoline-refurbished-systems/somatomdefinitionas>. Accessed: 2020-12-31.
- [9] X-ray mass attenuation coefficients. <https://www.nist.gov/pml/x-ray-mass-attenuation-coefficients>. Accessed: 2020-04-24.
- [10] Shiras Abdurahman, Frank Dennerlein, Anna Jerebko, Andreas Fieselmann, and Thomas Mertelmeier. Optimizing high resolution reconstruction in digital breast tomosynthesis using filtered back projection. In *International Workshop on Digital Mammography*, pages 520–527. Springer, 2014.

- [11] Shiras Abdurahman, Robert Frysch, Richard Bismark, Oliver Beuing, and Georg Rose. A complete scheme of empirical beam hardening correction using grangeat consistency condition. In *2018 IEEE Nuclear Science Symposium and Medical Imaging Conference Proceedings (NSS/MIC)*, pages 1–5. IEEE, 2018.
- [12] Shiras Abdurahman, Robert Frysch, Richard Bismark, Michael Friebe, and Georg Rose. Calibration free beam hardening correction using grangeat-based consistency measure. In *2016 IEEE Nuclear Science Symposium and Medical Imaging Conference Proceedings (NSS/MIC)*, pages 1–3. IEEE, 2016.
- [13] Shiras Abdurahman, Robert Frysch, Richard Bismark, Steffen Melnik, Oliver Beuing, and Georg Rose. Beam hardening correction using cone beam consistency conditions. *IEEE Transactions on Medical Imaging*, 37(10):2266–2277, 2018.
- [14] Shiras Abdurahman, Robert Frysch, Steffen Melnik, and Georg Rose. Beam hardening correction using pair-wise fan beam consistency conditions. In *15th International Meeting on Fully Three-Dimensional Image Reconstruction in Radiology and Nuclear Medicine*, volume 11072, page 110721T. International Society for Optics and Photonics, 2019.
- [15] Shiras Abdurahman, Robert Frysch, and Georg Rose. Reduction of beam hardening induced metal artifacts using consistency conditions. In *15th International Meeting on Fully Three-Dimensional Image Reconstruction in Radiology and Nuclear Medicine*, volume 11072, page 110721S. International Society for Optics and Photonics, 2019.
- [16] Shiras Abdurahman, Robert Frysch, and Georg Rose. Scatter correction using pair-wise fan beam consistency conditions. In *15th International Meeting on Fully Three-Dimensional Image Reconstruction in Radiology and Nuclear Medicine*, volume 11072, page 110722I. International Society for Optics and Photonics, 2019.
- [17] Shiras Abdurahman, Anna Jerebko, and Michael Kelm. Method and apparatus for projection image generation from tomographic images, February 14 2017. US Patent 9,569,864.
- [18] Shiras Abdurahman, Anna Jerebko, and Michael Kelm. Method for generating a combined projection image and imaging device, December 5 2017. US Patent 9,836,858.
- [19] Shiras Abdurahman, Anna Jerebko, Thomas Mertelmeier, Tobias Lasser, and Nassir Navab. Out-of-plane artifact reduction in tomosynthesis based on regression modeling and outlier detection. In *International Workshop on Digital Mammography*, pages 729–736. Springer, 2012.

- [20] André Aichert, Jerome Lesaint, Tobias Würfl, Rolf Clackdoyle, Laurent Desbat, and Andreas Maier. Stereo rectification for x-ray data consistency conditions. 2018.
- [21] André Aichert, Michael T Manhart, Bharath K Navalpakkam, Robert Grimm, Jana Hutter, Andreas Maier, Joachim Hornegger, and Arnd Doerfler. A realistic digital phantom for perfusion c-arm ct based on mri data. In *2013 IEEE Nuclear Science Symposium and Medical Imaging Conference (2013 NSS/MIC)*, pages 1–2. IEEE, 2013.
- [22] Chandima NPG Arachchige, Luke A Prendergast, and Robert G Staudte. Robust analogues to the coefficient of variation. *arXiv preprint arXiv:1907.01110*, 2019.
- [23] Matthias Baer and Marc Kachelrieß. Hybrid scatter correction for ct imaging. *Physics in Medicine & Biology*, 57(21):6849, 2012.
- [24] Matthias Bertram, Jens Wiegert, and Georg Rose. Potential of software-based scatter corrections in cone-beam volume ct. In *Medical Imaging 2005: Physics of Medical Imaging*, volume 5745, pages 259–270. International Society for Optics and Photonics, 2005.
- [25] Richard NK Bismark, Robert Frysch, Shiras Abdurahman, Oliver Beuing, Manuel Blessing, and Georg Rose. Reduction of beam hardening artifacts on real c-arm ct data using polychromatic statistical image reconstruction. *Zeitschrift für Medizinische Physik*, 30(1):40–50, 2020.
- [26] Rodney A Brooks and Giovanni Di Chiro. Beam hardening in x-ray reconstructive tomography. *Physics in medicine & biology*, 21(3):390, 1976.
- [27] Simone Carmignato, Wim Dewulf, and Richard Leach. *Industrial X-ray computed tomography*. Springer, 2018.
- [28] Rolf Clackdoyle. Necessary and sufficient consistency conditions for fanbeam projections along a line. *IEEE Transactions on Nuclear Science*, 60(3):1560–1569, 2013.
- [29] Bruno De Man, Johan Nuyts, Patrick Dupont, Guy Marchal, and Paul Suetens. Metal streak artifacts in x-ray computed tomography: a simulation study. In *Nuclear Science Symposium, 1998. Conference Record. 1998 IEEE*, volume 3, pages 1860–1865. IEEE, 1998.
- [30] C. Debbeler, N. Maass, M. Elter, F. Dennerlein, and T. M. Buzug. A new ct rawdata redundancy measure applied to automated misalignment correction. In *Fully Three-Dimensional Image Reconstruction in Radiology and Nuclear Medicine*, pages 264–267, 2013.

- [31] Michel Defrise and Rolf Clack. A cone-beam reconstruction algorithm using shift-variant filtering and cone-beam backprojection. *IEEE transactions on medical imaging*, 13(1):186–195, 1994.
- [32] Frank Dennerlein. *Image Reconstruction from Fan-Beam and Cone-Beam Projections*. Friedrich-Alexander-Universitaet Erlangen-Nuernberg (Germany), 2009.
- [33] Matthias Ebert. *Non-ideal projection data in X-ray computed tomography*. PhD thesis, Universität Mannheim, 2001.
- [34] Idris A Elbakri and Jeffrey A Fessler. Statistical image reconstruction for polyenergetic x-ray computed tomography. *IEEE transactions on medical imaging*, 21(2):89–99, 2002.
- [35] Idris A Elbakri and Jeffrey A Fessler. Segmentation-free statistical image reconstruction for polyenergetic x-ray computed tomography with experimental validation. *Physics in Medicine & Biology*, 48(15):2453, 2003.
- [36] Lee A Feldkamp, Lloyd C Davis, and James W Kress. Practical cone-beam algorithm. *Josa a*, 1(6):612–619, 1984.
- [37] Robert Frysch and Georg Rose. Rigid motion compensation in interventional c-arm ct using consistency measure on projection data. In *International Conference on Medical Image Computing and Computer-Assisted Intervention*, pages 298–306. Springer, 2015.
- [38] Lars Gjestebj, Bruno De Man, Yannan Jin, Harald Paganetti, Joost Verburg, Drosoula Giantsoudi, and Ge Wang. Metal artifact reduction in ct: where are we after four decades? *IEEE Access*, 4:5826–5849, 2016.
- [39] Pierre Grangeat. Mathematical framework of cone beam 3d reconstruction via the first derivative of the radon transform. In *Mathematical methods in tomography*, pages 66–97. Springer, 1991.
- [40] Peter Hammersberg and Måns Mångård. Correction for beam hardening artefacts in computerised tomography. *Journal of X-ray Science and Technology*, 8(1):75–93, 1998.
- [41] Richard Hartley and Andrew Zisserman. *Multiple view geometry in computer vision*. Cambridge university press, 2003.
- [42] Hein Hein, Zhou Yu, and Satoru Nakanishi. Three-dimensional two material based beam hardening correction for iterative reconstruction. In *The 4th International Conference on Image Formation in X-Ray Computed Tomography*, pages 455–458, 2016.

- [43] B Heismann and M Balda. Quantitative image-based spectral reconstruction for computed tomography. *Medical physics*, 36(10):4471–4485, 2009.
- [44] Gabor T Herman. Correction for beam hardening in computed tomography. *Physics in Medicine & Biology*, 24(1):81, 1979.
- [45] Stefan Hoppe. Accurate cone-beam image reconstruction in c-arm computed tomography. 2008.
- [46] Berthold K.P. Horn. Grangeat’s “trick”. https://people.csail.mit.edu/bkph/courses/papers/Exact_Conebeam/Grangeat_Trick.pdf. Accessed: 2021-03-28.
- [47] Godfrey N Hounsfield. Computerized transverse axial scanning (tomography): Part 1. description of system. *The British journal of radiology*, 46(552):1016–1022, 1973.
- [48] Jiang Hsieh. *Computed tomography: principles, design, artifacts, and recent advances*, volume 114. SPIE press, 2003.
- [49] Jiang Hsieh, Robert C Molthen, Christopher A Dawson, and Roger H Johnson. An iterative approach to the beam hardening correction in cone beam ct. *Medical physics*, 27(1):23–29, 2000.
- [50] Sébastien Jan, D Benoit, E Becheva, T Carlier, F Cassol, P Descourt, T Frisson, L Grevillot, L Guigues, L Maigne, et al. Gate v6: a major enhancement of the gate simulation platform enabling modelling of ct and radiotherapy. *Physics in Medicine & Biology*, 56(4):881, 2011.
- [51] Steven G. Johnson. The nlopt nonlinear-optimization package. <http://ab-initio.mit.edu/nlopt>, 2016.
- [52] Peter M Joseph and Robin D Spital. A method for correcting bone induced artifacts in computed tomography scanners. *Journal of computer assisted tomography*, 2(1):100–108, 1978.
- [53] M Kachelrieß and Willi A Kalender. Improving pet/ct attenuation correction with iterative ct beam hardening correction. In *IEEE Nuclear Science Symposium Conference Record, 2005*, volume 4, pages 5–pp. IEEE, 2005.
- [54] Marc Kachelrieß. *Reduktion von Metallartefakten in der Roentgen-computer-tomographie*. 1998.
- [55] Marc Kachelrieß, Katia Sourbelle, and Willi A Kalender. Empirical cupping correction: A first-order raw data precorrection for cone-beam computed tomography. *Medical physics*, 33(5):1269–1274, 2006.

- [56] Avinash C Kak and Malcolm Slaney. *Principles of computerized tomographic imaging*. SIAM, 2001.
- [57] Changhwan Kim, Miran Park, Younghun Sung, Jaehak Lee, Jiyoung Choi, and Seungryong Cho. Data consistency-driven scatter kernel optimization for x-ray cone-beam ct. *Physics in Medicine & Biology*, 60(15):5971, 2015.
- [58] Yiannis Kyriakou, Esther Meyer, Daniel Prell, and Marc Kachelrieß. Empirical beam hardening correction (ebhc) for ct. *Medical physics*, 37(10):5179–5187, 2010.
- [59] Jerome Lesaint. *Data consistency conditions in X-ray transmission imaging and their application to the self-calibration problem*. PhD thesis, 2018.
- [60] Jérôme Lesaint, Simon Rit, Rolf Clackdoyle, and Laurent Desbat. Calibration for circular cone-beam ct based on consistency conditions. *IEEE Transactions on Radiation and Plasma Medical Sciences*, 1(6):517–526, 2017.
- [61] Jacob Levi, Brendan L Eck, Rachid Fahmi, Hao Wu, Mani Vembar, Amar Dhanantwari, Anas Fares, Hiram G Bezerra, and David L Wilson. Calibration-free beam hardening correction for myocardial perfusion imaging using ct. *Medical physics*, 46(4):1648–1662, 2019.
- [62] Baolei Li, Quanhong Zhang, and Junjiang Li. A novel beam hardening correction method for computed tomography. In *2007 IEEE/ICME International Conference on Complex Medical Engineering*, pages 891–895. IEEE, 2007.
- [63] Xinhua Li, Da Zhang, and Bob Liu. A generic geometric calibration method for tomographic imaging systems with flat-panel detectors—a detailed implementation guide. *Medical physics*, 37(7Part1):3844–3854, 2010.
- [64] Donald Ludwig. The radon transform on euclidean space. *Communications on pure and applied mathematics*, 19(1):49–81, 1966.
- [65] Andreas Maier, Hannes G Hofmann, Martin Berger, Peter Fischer, Chris Schwemmer, Haibo Wu, Kerstin Müller, Joachim Hornegger, Jang-Hwan Choi, Christian Riess, et al. Conrad—a software framework for cone-beam imaging in radiology. *Medical physics*, 40(11):111914, 2013.
- [66] Andreas Maier, Stefan Steidl, Vincent Christlein, and Joachim Hornegger. *Medical Imaging Systems: An Introductory Guide*, volume 11111. Springer, 2018.
- [67] Esther Meyer, Rainer Raupach, Michael Lell, Bernhard Schmidt, and Marc Kachelrieß. Normalized metal artifact reduction (nmar) in computed tomography. *Medical physics*, 37(10):5482–5493, 2010.

- [68] Sucheta Mohapatra. Development and quantitative assessment of a beam hardening correction model for preclinical micro-ct. 2012.
- [69] Xuanqin Mou, Shaojie Tang, and Hengyong Yu. Comparison on beam hardening correction of ct based on hl consistency and normal water phantom experiment. In *SPIE Optics+ Photonics*, pages 63181V–63181V. International Society for Optics and Photonics, 2006.
- [70] B Ohnesorge, T Flohr, and K Klingensbeck-Regn. Efficient object scatter correction algorithm for third and fourth generation ct scanners. *European radiology*, 9(3):563–569, 1999.
- [71] Robert C Orth, Michael J Wallace, Michael D Kuo, Technology Assessment Committee of the Society of Interventional Radiology, et al. C-arm cone-beam ct: general principles and technical considerations for use in interventional radiology. *Journal of Vascular and Interventional Radiology*, 19(6):814–820, 2008.
- [72] Hyoung Suk Park, Yong Eun Chung, and Jin Keun Seo. Computed tomographic beam-hardening artefacts: mathematical characterization and analysis. *Philosophical Transactions of the Royal Society A: Mathematical, Physical and Engineering Sciences*, 373(2043):20140388, 2015.
- [73] Hyoung Suk Park, Dosik Hwang, and Jin Keun Seo. Metal artifact reduction for polychromatic x-ray ct based on a beam-hardening corrector. *IEEE transactions on medical imaging*, 35(2):480–487, 2015.
- [74] Dennis L Parker. Optimal short scan convolution reconstruction for fan beam ct. *Medical physics*, 9(2):254–257, 1982.
- [75] G Poludniowski, G Landry, F DeBlois, PM Evans, and F Verhaegen. Spekcalc: a program to calculate photon spectra from tungsten anode x-ray tubes. *Physics in Medicine & Biology*, 54(19):N433, 2009.
- [76] Michael JD Powell. A direct search optimization method that models the objective and constraint functions by linear interpolation. In *Advances in optimization and numerical analysis*, pages 51–67. Springer, 1994.
- [77] Alexander Preuhs, Andreas Maier, Michael Manhart, Markus Kowarschik, Elisabeth Hoppe, Javad Fotouhi, Nassir Navab, and Mathias Unberath. Symmetry prior for epipolar consistency. *International journal of computer assisted radiology and surgery*, 14(9):1541–1551, 2019.
- [78] Zhi Qiao, Alfredo Illanes, Shiras Abdurahman, and Michael Friebe. A novel automatic gauge detection algorithm for the performance test of a ct scanner with catphan 600 phantom.

- [79] Johann Radon. 1.1 über die bestimmung von funktionen durch ihre integralwerte längs gewisser mannigfaltigkeiten. *Classic papers in modern diagnostic radiology*, 5:21, 2005.
- [80] Karsten Schörner. *Development of methods for scatter artifact correction in industrial x-ray cone-beam computed tomography*. PhD thesis, Technische Universität München, 2012.
- [81] Chris C Shaw. *Cone beam computed tomography*. Taylor & Francis, 2014.
- [82] Alejandro Sisniega, Wojciech Zbijewski, Jennifer Xu, Hao Dang, Joseph Webster Stayman, J Yorkston, Nafi Aygün, V Koliatsos, and Jeffrey H Siewerdsen. High-fidelity artifact correction for cone-beam ct imaging of the brain. *Physics in Medicine & Biology*, 60(4):1415, 2015.
- [83] Bruce D Smith. Image reconstruction from cone-beam projections: necessary and sufficient conditions and reconstruction methods. *IEEE transactions on medical imaging*, 4(1):14–25, 1985.
- [84] Josh Star-Lack, Mingshan Sun, Anders Kaestner, Rene Hassanein, Gary Virshup, Timo Berkus, and Markus Oelhafen. Efficient scatter correction using asymmetric kernels. In *Medical Imaging 2009: Physics of Medical Imaging*, volume 7258, page 72581Z. International Society for Optics and Photonics, 2009.
- [85] Norbert Strobel, Oliver Meissner, Jan Boese, Thomas Brunner, Benno Heigl, Martin Hoheisel, Günter Lauritsch, Markus NaGel, Marcus Pfister, Ernst-Peter Rührschopf, et al. 3d imaging with flat-detector c-arm systems. In *Multislice CT*, pages 33–51. Springer, 2009.
- [86] Paul Suetens. *Fundamentals of medical imaging*. Cambridge university press, 2017.
- [87] M Sun and JM Star-Lack. Improved scatter correction using adaptive scatter kernel superposition. *Physics in Medicine & Biology*, 55(22):6695, 2010.
- [88] Shaojie Tang, Xuanqin Mou, Qiong Xu, Yanbo Zhang, James Bennett, and Hengyong Yu. Data consistency condition-based beam-hardening correction. *Optical Engineering*, 50(7):076501, 2011.
- [89] Maurice Tubiana. Wilhelm conrad röntgen and the discovery of x-rays. *Bulletin de l'Académie nationale de médecine*, 180(1):97–108, 1996.
- [90] Elke Van de Castele, Dirk Van Dyck, Jan Sijbers, and Erik Raman. A model-based correction method for beam hardening artefacts in x-ray microtomography. *Journal of X-ray Science and Technology*, 12(1):43–57, 2004.

- [91] Ge Wang, Yi Zhang, Xiaojing Ye, and Xuanqin Mou. *Machine learning for tomographic imaging*. IOP Publishing, 2019.
- [92] Oliver Watzke. Jaw phantom. <http://www.imp.uni-erlangen.de/phantoms/jaw/jaw.htm>. Accessed: 2021-10-25.
- [93] Martin J Willemink and Peter B Noël. The evolution of image reconstruction for ct—from filtered back projection to artificial intelligence. *European radiology*, 29(5):2185–2195, 2019.
- [94] Tobias Würfl, Mathis Hoffmann, André Aichert, Andreas K Maier, Nicole Maaß, and Frank Dennerlein. Calibration-free beam hardening reduction in x-ray cbct using the epipolar consistency condition and physical constraints. *Medical Physics*, 46(12):e810–e822, 2019.
- [95] Xiaochun Yang. *Geometry of cone-beam reconstruction*. PhD thesis, Massachusetts Institute of Technology, 2002.
- [96] Hengyong Yu, Yuchuan Wei, Jiang Hsieh, and Ge Wang. Data consistency based translational motion artifact reduction in fan-beam ct. *IEEE Transactions on Medical Imaging*, 25(6):792–803, 2006.
- [97] M Zellerhoff, B Scholz, E-P Ruehrnschopf, and T Brunner. Low contrast 3d reconstruction from c-arm data. In *Medical Imaging 2005: Physics of Medical Imaging*, volume 5745, pages 646–655. International Society for Optics and Photonics, 2005.
- [98] Gengsheng Lawrence Zeng. *Medical image reconstruction: a conceptual tutorial*. Springer, 2010.
- [99] Wei Zhao, Stephen Brunner, Kai Niu, Sebastian Schafer, Kevin Royalty, and Guang-Hong Chen. Patient-specific scatter correction for flat-panel detector-based cone-beam ct imaging. *Physics in Medicine & Biology*, 60(3):1339, 2015.